Experimental Investigations and Numerical Modelling of a Mixed Flow Marine Waterjet

by

Richard Warren Kimball

Submitted to the Department of Ocean Engineering
in partial fulfillment of the requirements for the degree of

Doctor of Philosophy
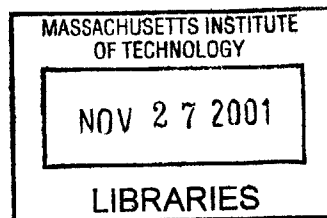
at the

MASSACHUSETTS INSTITUTE OF TECHNOLOGY

June 2001

Author . . . .
Department of Ocean Engineering
June 1, 2001

Certified by. . . .
Justin E. Kerwin
Professor of Naval Architecture
Thesis Supervisor

Accepted by . . . .
Henrik Schmidt
Professer of Ocean Engineering
Chairman, Department Committee on Graduate Studies

Experimental Investigations and Numerical Modelling of a Mixed Flow Marine Waterjet

by

Richard Warren Kimball

Abstract

Recently, waterjet propulsion has gained great commercial interest as the shipping industry trends toward faster passenger ferries and other fast transport vessels. The work presented in this thesis was part of a larger effort to improve the capabilities and performance of a mixed flow marine waterjet used in such high speed marine applications.

An experimental test faciity was constructed and employed in the testing of a mixed flow marine waterjet rotor, stator and housing set. Full description of the facility and waterjet test procedures are discussed. The pumpset was designed using a coupled Lifting Surface/RANS procedure by Taylor et.al.[35] and was built and tested as part of the work presented in this research. Detailed measurements of the pump performance is described including pump curves, tipgap studies, inlet, midstage and outlet velocity and pressure profiles in an axisymmetric inflow. Full accounting for losses including rotor and stator loss profiles as well as a full pumpset energy balance is presented. From the results of the experiment, dominant losses were found near the tip/duct junction casing along with a large and unexpected increase in swirl in this region.

Detailed numerical modelling of this pumpset was performed using both a Lifting Surface/RANS procedure and a Lifting Surface/Euler solver. Effects of losses were modelled as well as tipgap effects. Prior work had developed these coupling procedures but the computationally efficient Euler coupling lacked the introduction of loss and drag induced swirl. This loss coupling was added to the model and the analysys results are discussed. Also, a model to align the wakesheet with the local flowfield in the Lifting Surface solver was developed and these results are discussed.

Thesis Supervisor: Justin E. Kerwin
Title: Professor of Naval Architecture

Acknowledgments

Contents

List of Figures

List of Tables

NOMENCLATURE

A_{inlet} = Duct area at inlet measurement plane

$A_{midstage}$ = Duct area at midstage measurement plane

A_{exit} = Duct area at exit measurement plane

A_{tun} = Inlet area of tunnel forward of the flow nozzle

A_{noz} = Area of the nozzle throat (less the shaft casing area)

A_{panel} = Vortex lattice panel area

$Cd(r)$ =Sectional Drag Coefficient

$C(r)$ =Effective Blade chord along streamtube

C_q =Gap flow coefficient

D_i =Inlet Duct Diameter

E =Bulk Fluid energy flux (power)

E_{loss} = Bulk Fluid energy loss (power loss)

$F_{drag}(r)$ = Sectional Drag Force

$F_{sdrag}(r)$ = volumeric viscous body force

F_Θ, F_{Θ_v} = Volumetric body force, total and viscous in tangential direction

$F_{gaploss}$ = Effective gap loss force

g = acceleration due to gravity

H =height of water column in calibrator

h_t, h_{inl} = stagnation enthalpy, enthalpy at inlet

J = Non-dimensional rotor speed $J = Vref/NDref$ N is rev/sec

K = Viscous correction for nozzle flow calculation

Kt = Blade row thrust coefficient = $\frac{Thrust}{\rho N^3 D_r^3}$

Kq = Blade row torque coefficient = $\frac{Torque}{\rho N^2 D_r^5}$

$P_{in.static}, P_{out.static}$ = Wall static pressure at pump inlet and outlet

P_{tot} = Bulk Pumpset total pressure rise

P_t = Stagnation Pressure

$P_{t\Omega}$ = Stagnation Pressure in Rotating Frame

P_{tinl} = Inlet Stagnation Pressure

P_g = Pressure across gap

11

ΔP_{noz} = Nozzle pressure drop from inlet to nozzle throat

$\dot{Q}$ = Volumetric Flowrate

R_{core} = Vortex Core Radius

RC_0 = Initial Vortex core radius

RC_{grow} = Vortex core growth factor

$Re = \frac{U_i D_i}{\nu}$ Reynolds number based on inlet plane diameter and mean axial velocity

r = radius

r_i = inner streamline radius

r_o = outer streamline radius

s = streamline coordinate

S = entropy

T = Rotor shaft torque

t = mean rotor tip clearance

t_n = vortex growth timestep

U_i = Mean Inlet Axial Velocity

$\vec{V_{eff}}$ = Effective velocity

$\vec{V_{tot}}$ = total velocity (actual flowfield velocity)

$\vec{V_{ind}}$ = Velocity induced by singularities

V_g = Tip gap velocity

V_s = Velocity along streamline

Vx, Vr, Vt = Axial, Radial and Tangential velocity

Ux, Ur, Ut = normalized Axial, Radial and Tangential velocity/Vi

x = axial coordinate

γ = compressibility

Γ = Vortex strength

ν = kinematic viscosity

ρ = Fluid Density

τ = Vortex growth time

$\varpi(r)$ = pressure loss coefficient

ω = Rotation rate radians/second

Ξ = Bulk Fluid energy flux (non-dimensional)

Ξ_{loss} = Bulk Fluid energy flux loss (non-dimensional)

Ξ_{shaft} = Non-Dimensional Shaft power = $\frac{T\Omega}{\rho U_i^3 D_i}$

$\xi(r)$ = Fluid Energy flux coefficient

$\xi loss(r)$ = Energy loss flux coefficient

Ψ = Stream function

Chapter 1

Introduction

1.1 Motivation

1.1.1 Waterjets for Ship Propulsion

Marine waterjet propulsion for large ships has existed for quite some time. Allison [1] cites some of the historical development of marine waterjets, with modern waterjets being implemented starting in the 1950's . Recently, however, interest in marine waterjets for large ships has risen sharply due mainly to interest in fast ferries. The motivation for fast ferries is economically driven as speed means more effective transport for passengers and their cargo. As fast ferries become viable alternatives to land transportation in many areas, the faster time of the transport transates directly into improved tranportation effectiveness.

Conventional propulsion in the form of external propellers have proved very efficient at propelling large ships at moderate speed, and have done so for more than a hundred years. The top speed of a ship is limited by the engine shaft power and propeller blade cavitation. Modern high speed ships, in the form of catomarans, have narrow hulls which would warrent a smaller propeller for maximum efficiency. To absorb the shaft power would require a very high speed propeller prone to cavitation since the propeller power density would be high. In this case the internal flow the waterjet has advantages. Because the blade rows are housed internally, the pressure rise in the housing can help reduce cavitation effects, and highly loaded blades can be designed to operate very efficiently. Such waterjets are routinely installed today

on large fast ferries that reach top speeds in excess of forty knots.

In some sense, the migration of the ship propulsion industry from propellers to waterjets is analogous to the migration of the aeronautical industry from airplane propellers (for low speed aircraft) to gas turbine engines as the desire for higher speed became necessary. In the aeronautical world, Mach number effects become a critical design constraint analogous to cavitation in the marine world (though they are physically very different phenomenon).

Pump efficiency and cavitation performance are two criteria that drive much of the hydrodynamic design of the waterjet. It is desirable to have the waterjet power density be high, to either fit the most pump in the space available or reduce the cost of the pump by reducing its size. The prior constraint is very important in the installation of waterjets in catomaran hulls where the desire to improve ship speed drives hull design to be narrower, thus limiting the space available for the waterjet. The effect of high loading means that cavitation effects are more likely.

The current research is part of a larger program to improve the performance of a typical commercial marine waterjet. The main goal of this research was to carefully measure the flow details and performance characteristics of mixed flow marine waterjet designed as part of this program to better understand the details of the pump performance, losses etc. Since this waterjet was designed using recently developed numerical modelling methods, another major goal of the current research was to validate the accuracy of these computational design and analysis tools. As part of this validation of the computational tools, efforts were made to enhance the models to improve modelling of flow features important to waterjets. For example, it was found that tip clearance flows were responsible for a major part of the losses for the rotor and improvements to modelling this effect were implemented and tested.

1.1.2 Propellers vs. Turbomachines

In the development of propulsors in general two major design paradigms exist, the propeller paradigm and the turbomachinery paradigm. The methodology of propeller design has its roots in the area of wing theory since a typical propeller has a small

15

number of blades, and the modelling details of the flow require the computation of the flow around these "wings". The typical computational models used to design and analyze propellers are potential flow based and represent blades using singularity elements on the propeller surfaces and in the blade wakes. These techniques are very similar to those techniques used to analyze fixed wings. In fact, a modern course in propeller design taught by Prof. Jake Kerwin [22] of MIT is titled "Hydrofoils and Propellers" and spends half the course covering wing theory as background to propeller design. These methods capture fully three dimensional effects of the propulsor on the flow field. However, since the propulsor operates in an external flow field, the background flowfield is input to the potential flow calculation. Fortunately, for typical propellers, this backgound flow can be estimated to sufficient accuracy for the computation.

Though the paradigm of turbomachinery design also has roots in 2-D wing theory, there are major differences in the design techniques used in comparison with propeller design. For one, turbomachines are typically internal flow machines and hence pressure rise is a major factor and design criterion. Generally the solidity of the blade rows (defined as the projected area of the blades divided by the area of the blade annulus) is greater than one. This is generally achieved through high blade number. The effect of high solidity is that the flow follows the blade geometry closely and designers can calculate performance based on this assumption, greatly simplifying modelling, since blade to blade variations in the flowfield are typically small. Blade design is typically done using using strip theory for 2-D blade sections operating in a cascade. Empirical relationships for estimating second order effects are then typically applied as corrections to the model. In analyzing the flow through the turbomachine, axisymmetric flow is typically assumed and the Euler turbine equation is utilized to track stagnation pressures, temperatures etc. throughout the flow passage.

In the current work the merging of these two paradigms has been an unforseen outcome of the design, analysis and experimental studies on a mixed flow marine waterjet. Even though waterjets are marine propulsors, they fit better into the realm of turbomachinery than in the realm of propellers. In fact, many researchers and

designers use techniques with roots in turbomachinery design to successfully design waterjets. Some more modern example of these techniques can be found in Zangeneh [44], [43] and Huntsman et al.[12], though these more modern methods deal with some of the 3-D blading effects in a more sophisticated fashion than earlier 2-D strip cascade methods.

A major motivating factor in the goals of this waterjet development effort was the desire to implement complicated blade shapes to improve cavitation performance. To properly design such blade shapes requires fully three dimensional blade solvers and 2-D strip theory is inadequate for such analysis. For this the propeller design methodology comes to the rescue. For its part, turbomachinery throughflow modelling is very good at tracking the flow through a passage of bladerows. The propeller codes need this background flow to do their job and thus the merging of these two realms is a marriage made in heaven, well almost. One still needs to communicate back and forth between the two techniques in some sort of coupling procedure.

1.1.3 Lifting Surface/Throughflow coupled solvers

The success of vortex-lattice based potential solvers in accurately computing the hydrodynamic performance of marine propulsors has been both remarkable and well proven in the area of open and ducted propellers. Computational codes such as those developed by Kerwin and others have been utilized in the design and analysis of external flow marine propellers for over thirty years with great success. Examples of these methods can be found in references [15],[19],[9],

The vortex lattice method is a class of potential flow solvers which represent the propeller blades using a lattice of vortex singularity elements applied to the propellers mean camber surface(i.e. lifting surface). Blade thickness is generally represented using source line elements coincident with the vortex elements. Control points are carefully placed between the lattice loops and the velocity at the points is specified such that no flow passes through the blade (or vortex loop). Then a linear system of equations is solved to find the strengths of the singularity elements such that this boundary condition is satisfied. Another class of solver, similar to the vortex lattice

method, is a panel method where singularity panels (dipole and source) are applied to the surface of the blade, explicitly representing the blade thickness. All these types of solvers have the capability to analyse and design complicated three dimensional blade shapes and can include the effects of all other surfaces of the propeller such as other blades, hub and duct etc.

Potential solvers are accurate in giving the flow characteristics around propellers given the following conditions are valid:

- The boundary layers on all surfaces are thin

- regions of viscous flow are small (such as secondary junction flows, tip flows etc.

- The background or "effective" flowfield is known

The requirement of the knowing the background flowfield is one of the caveats of the potential based methods, but for external flow marine propellers there exist good methods to estimate this flowfield, even in cases of non-uniform inflow (such as a ship wake). The effective velocity field is the background flow field in which the propeller operates. This effective flowfield is affected by the presence of the propeller. However, we are solving for the propellers influence on the flowfield so its effects on the background or "effective" flowfield is unkown. Thus we have a paradox where we need the background or "effective" flowfield to solve the lifting surface problem and we need the propeller's influence on the nominal inflow to get the proper "effective" inflow. For most propellers, the influence of the propeller on this background flowfield is relatively small and thus methods to estimate this effective flowfield have been very effective. Examples of methods to estimate the "effective" flow field can be found in Wilson et al. [40] and Taylor [33]. Mathematically the "effective" flow is defined as the total velocity field minus the velocity induced by the lifting surface singularities as depicted in equation 3.10, where $\bar{V}_{tot}$ is the total velocity, $\bar{V}_{ind}$ is the induced velocity due to singularity elements and $\bar{V}_{eff}$ is the effective velocity.

$$\vec{V}_{eff} = \vec{V}_{tot} - \vec{V}_{ind}$$

(1.1)

18

For the case of highly loaded propulsors and internal flow propulsors, estimation of this effective flowfield is more difficult, and without a robust and accurate method to determine the effective flowfield accurate calculations are difficult. One solution to this problem is to solve the background flowfield using a discrete fluid solver such as a Reynolds Averaged Navier Stokes (RANS) solver or an Euler solver. These methods discretize the entire flow domain and solve the flow field explicitly. One could discretize the three dimensional fluid domain including rotating blades, boundaries etc. and solve for the entire propulsor's performance using one solver. However, the discretization of the entire flow field including blade rows would require very fine meshing in general and the presence of rotating blades means that the grid would need to be regenerated for each time step (or some other clever gridding scheme would be required). In short, the computation and grid administration burden makes such calculations very tedious and time consuming for the engineer. If one were to throw in multiple blade rows the task becomes even more untenable.

In the Lifting Surface/ Throughflow solver coupling technique the lifting surface calculation on the blade rows are calculated in some starting flowfield (not the correct flowfield). The lifting surface code computes the blade forces, losses etc. and then passes the time averaged component of these forces (or equivalently, entropy and rV_θ) to the throughflow solver grid. The throughflow solvers used in this research were axisymmetric steady solvers so the time-averaged "forces" etc. are equivalent to circumferential mean "forces". The throughflow solver then solves for the fluid field given these forces to give a total flowfield. The blade row's influence velocity is subtracted from this total velocity field what is left is an "effective" velocity which is used for the next lifting surface calculation. This procedure is repeated iteratively until (hopefully) the solution converges. The final solution represents the bladerow performance in the proper background or effective flowfield which includes the effects of the blade row on the effective flow. Figure 1-1 depicts this iterative process showing the passing of forces to the throughflow solver and the passing of the velocity field back to the lifting surface. The "coupling" part of the process happens outside of both
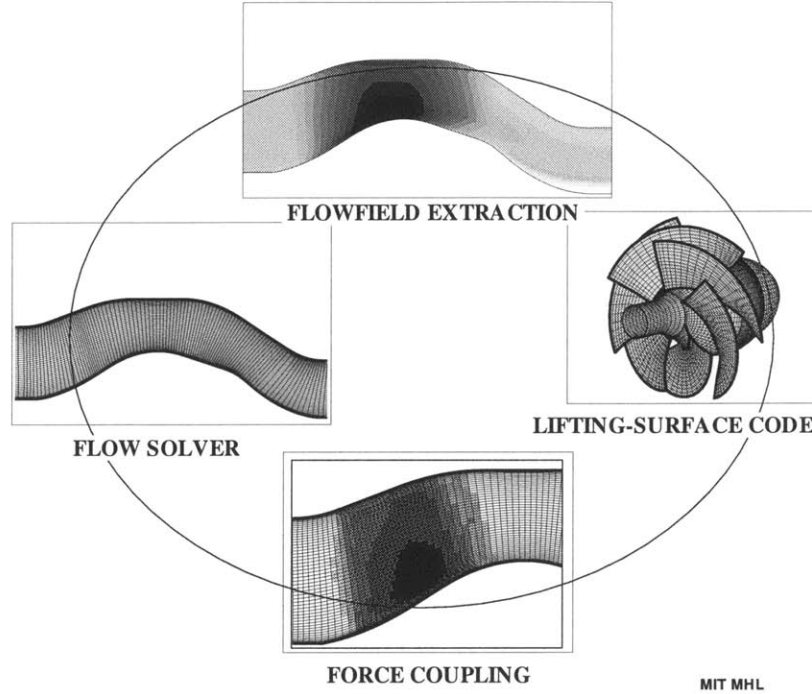
Figure 1-1: Lifting Surface/Throughflow Solver Coupling Procedure

the flow codes by routines that convert output quantities from one code into input quantities that the other code understands. Details of the coupled Lifting Surface/ Throughflow solver methods can be found in Kerwin et al. [18], [21], [20], Black [4], and McHugh [27].

The advantage of coupling a 3-D potential solver with a throughflow solver is the ability to design and analyze complex blade shapes with significant skew and rake. Conventional 2-D strip theory design as well as quasi 3D methods have trouble capturing the three dimensional blade effects which can be significant. The advantage of more complicated blade shapes are the possibility of significant improvement in cavitation performance and reduction of structural vibration. Both of these factors are important considerations for waterjets but cavitation improvement can significantly improve the maximum power at which the pump can operate.

1.1.4 Background of the Waterjet Program

In 1997 an effort was initiated by what was then the Bird Johnson Co. (now Rolls Royce Marine) as part of a MARITECH program to improve the performance of a conventional marine waterjet typical of those is use in large fast ferries. The details of this design effort are documented in Taylor et.al [35]. Classical turbomachinery techniques were employed to come up with a starting geometry which could be input into a computational design procedure where the final blade shapes were then generated. General pump parameters such as casing geometry, rotation rate, blade chordlengths as well as the loading distributions for both stator and rotor were set prior to initiating the computational design. In this way the modelling techniques discussed in this paper do not replace conventional design techniques but enhance the overall design procedure. Good references covering classical turbomachinery design principles can be found in Vavra [37], Wilicenus [41], [42] and Lewis [24]

Once the "starting" design was determined, a coupled Vortex-Lattice/RANS solver was used for the blade row design. The resulting pump had design specific speed of 0.43 (7400 in English units) with a six bladed rotor with solidity of 1.82 and an eleven bladed stator with blade solidity of 1.73. Figure 1-2 depicts the computational representation of the pump as designed. In parallel with the design effort was an effort to design and implement a test facility to test the designed pump at the Marine Hydrodynamics Laboratory at MIT. This effort is actually part of the efforts outlined in this thesis and will be discussed in detail later. The designed pumpset was then built and the constructed models are depicted in Figure 1-3, showing the rotor, rotor casing and the stator housing unit.

1.1.5 Summary of Experimental Efforts

As mentioned, a special facility was built specifically for the testing of marine waterjets at the Marine Hydrodynamics Laboratory(MHL) at MIT. Only a handful of waterjet test facilities exist in the world today. This thesis documents the details of the design and testing capabilities of the waterjet test facility. The test facility was designed to insert into the test section of the current water tunnel housed at the MHL,
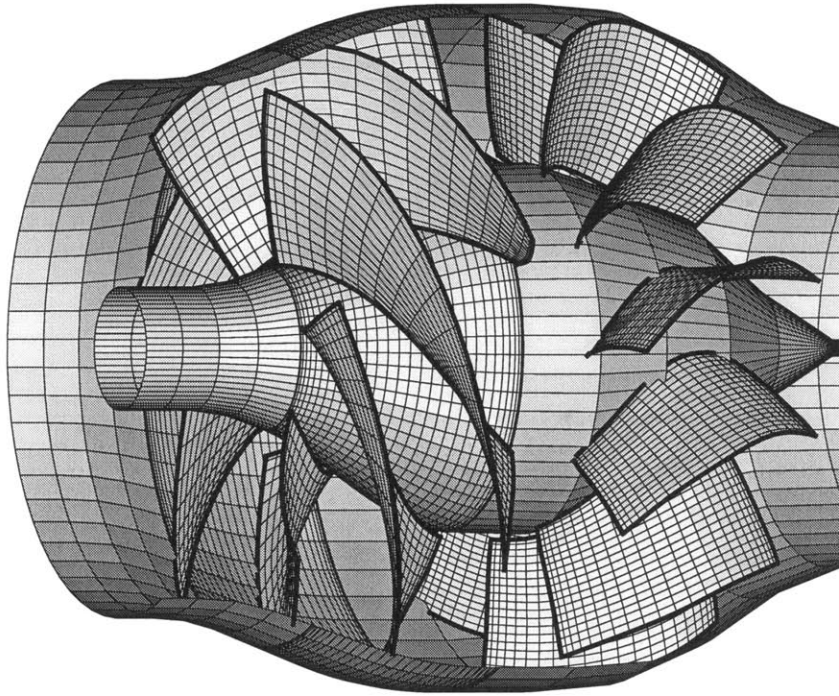
Figure 1-2: Computer Representation of the Designed Waterjet Pumpset

and consisted of a long axisymmetric duct with a nozzle at the inlet and a shaft running down the inlet to drive the rotor. Downstream of the waterjet model was a valve to control the pump operating point. Measurement planes located at the pump inlet, between the rotor and stator and at the pump exit allowed radial surveys of the three velocity components and stagnation pressure profiles. The rotor was encoded so that the Laser Doppler Velocimetry system (LDV) could resolve phase-averaged velocities at the rotor exit. Stagnation pressure profiles were measureed using Kiel probes which accurately resolved magnitude and was insensitive to inflow angle. This combination of total pressure measurements and velocity profile measurements provided a very direct calculation of losses. As a check on the loss measurement full integration of the energy profiles was conducted and was found to match the measured shaft input power within measurement error and served to validate the loss measurements. Details of the calculation methods used to determine losses are presented later in this document. Also summaries of the experimental testing, and the resultant validation, are also described in Taylor et al.[34] and Kimball et al.[23].

22
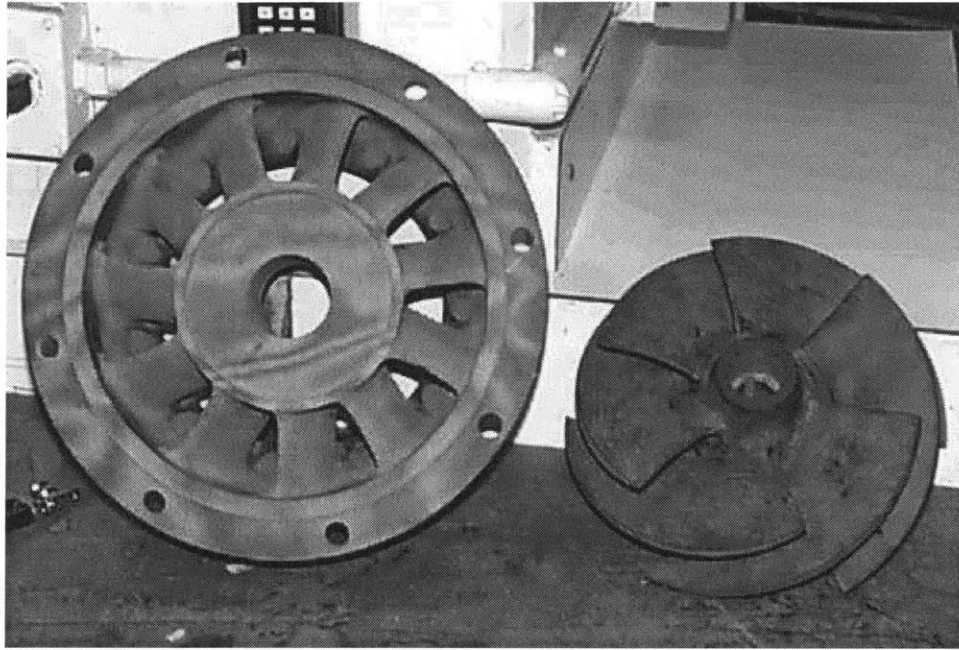
Figure 1-3: Photograph of the Designed Rotor casing and Stator Housing

The tip clearance between the rotor and casing could be controlled by moving the rotor fore and aft along the shaft and the tipgap parameter was found to have an extremely important effect on both the pressure rise and efficiency of the pump. The detailed studies of rotor and stator losses was conducted at a moderately high tip clearance, which is largeer than is typical for these types of marine waterjets. Therefore the losses measured in this condition were much higher than normally encountered. However, the nature of the details of the flow in the tipgap region were found to be similar even for small tip gaps such gap that the large gap data was representative of the general flow behavior for smaller gaps.

Given that the relative velocity through the stator set is low, the measured stator losses were unexpectedly high. However it was believed that the mechanisim for these stator losses was different from the rotor tipflow junction losses. It is believed that because the rotor exit flow was highly disturbed by the rotor losses that the incidence of the flow coming into the stator was far from its intended design. This was somewhat good news because this means that much of the stator losses can be recovered by realigning the stator blades to match the incoming flow.

It should be noted that the aspect ratio of the rotor blades was 0.35 and little empirical data is available for this low an aspect ratio. Gas turbine compressor stages are the closest match in aspect ratio but data for aspect ratios of less than 0.5 is rare. Since large blade chord has advantages in cavitation performance recent design methodology drives toward lower aspect ratios. Unfortunately this seems to result in larger pump losses, which may be why few have ventured into such low aspect ratio design. In a different realm, centrifugal machines generally have even lower aspect ratio (though the concept of aspect ratio becomes a little fuzzy in this geometry) and it is notable that these machines typically have lower efficiencies than their axial flow counterparts. The experimental work presented documents the flow performance of a mixed flow turbomachine with aspect ratio in a region where little data exists.

1.1.6 Summary of Numerical Modelling Improvements

In an effort to improve the numerical models, information gleaned from the waterjet experiments as compared to the predicted results led to efforts to improve those numerical models. The numerical modeling improvement efforts covered in this research included:

- Modelling of tip clearance leakage loss in terms of entropy

- Modelling of blade drag losses in terms of entropy

- Coupling the above loss mechanism with an Euler solver

- Addition of local flow wake alignment in the potential solver

The importance of the tip leakage/junction flow was apparent from the experimental data. The Lifting surface/RANS solver communicates information from the Lifting surface solver to the RANS solver in the form of circumferential mean body forces including blade drag) for which most of the losses are implicitly solved. Since the throughflow solver is axisymmetric it does not account for the fluid energy due to circumferential variations in the velocity and pressure fields. The Lifting Surface solver does account for blade to blade effects so the computed rotor forces include this effect. Prior research by Kerwin et al. [18], [21] determined how to properly couple the circumerential mean forces with the RANS solver but the contribution to

24

the unsteady kinetic energy due to the non-axisymmetric component of force was not coupled into the RANS solver. In this research, as well, no attempt was made to add theses additional effects into the RANS coupling procedure.

The tip leakage model implemented into the lifting surface model is described by McHugh [27] and is based on models derived by Kerwin [16] and Van Houten [11]. On the lifting surface, the last blade panel actually represents the physical tipgap in position and size. During the solution fluid is allowed to "leak" through the gap panel. An orifice flow model is implemented to limit the flow through the gap by the jump in pressure across the panel and this is iteratively solved until both the orifice equation is satisfied and the lifting surface boundary condition is satisfied. The force on the gap panel then simply becomes the force on the bound gap vortices. The component of this force in the direction of the local gap flow streamline is then directly related to the entropy rise, which is passed to the Euler throughflow solver to model leakage losses.

Drag losses were relatively easy to couple since the force was known directly and hence easily converted to entropy rise. In the lifting surface model the sectional blade drag losses were either input by the user as sectional drag coefficents or could be explicilty estimated using an integral boundary layer model built into the method. The integral boundary layer techniques used for the blade boundary layer calculation in the model are similar to those implemented by Drela [7]. For this research the integral boundary layer calculation was not used and sectional drag coefficients were entered directly from either estimations or those derived directly from the experimental results. In addition the component of the force in the tangential direction contributes to the swirl induced by the rotor. If care is taken to ensure that the total mean force (rotor induced plus drag forces) is accounted for in the coupling procedure then than the drag induced swirl would be properly accounted for in the Euler solver coupling. In coulping the Lifting Surface solver to the Euler solver the conversion from a velocity based coupling method to a combined force/velocity based coupling method was implemented as part of this research.

A significant part of the numerical modelling improvement effort was devoted to

the implementation of a scheme to align the wake with the local flowfield accounting for the influence of the wake trajectory on itself. The current coupled lifting surface model aligns the wake along the circumferential mean flowfield calculated by the throughflow solver. This alignment is efficient computationally and generally gives good results. However, in the case of open propulsors, the trajectory of the wake is complicated since the free end of the wake in a free tip propeller has tendancy to roll up on itself. Many other researchers have added wake alignment schemes to lifting surface codes (for example Greeley et al. [9]). The current method builds upon the work on wake rollup done by Ramsey [30], which was based on a desingularized vortex model capable of dealing with the wake rollup without "blowing up" due to singularity issues of the vortex trailer crossing a control point. The vortex model implemented has some resemblence to a rankine vortex with a viscous core and the method tended to help stabilize the wake alignment procedure. The method implemented in this research applies this type of logic to all wake trailers (not just the tip vortex) and adds a viscous core growth algorithm based on the decay of a steady 2-D (Oseen) vortex in a viscous fluid.

The wake alignment procedure was found not to have an important effect in the case of an internal flow waterjet. In hindsight this makes sense since the wake is more constrained to follow the circumferential mean flow due to the fact that it is in a duct. In fact for most of the waterjet validation cases the wake alignment procedure was not used since it is relatively computationally intensive. It is included in this research not because it is an important effect to model in the waterjet, but because the effort was significant and useful for external flow propeller calculations. In addition, the wake alignment procedure developed in this research could be used to implement a model of the tip leakage vortex which is a important phenomenon present in waterjets. The tip leakage flow looks much like a wake flow with a bizarre kutta condition applied (the orifice leakage flow) coming off the tip of the propeller. Unfortunately, there was not sufficient time to implement such a model as part of the current research, though the major building blocks for this model are in place.

1.1.7 Summary of Validation Efforts

From the experimental portion of this research the effects of the losses driven by the blade/duct tipgap region of the rotor were found to be responsible for the majority of the rotor losses. Loss mechanisms of this sort were not originally modelled in the lifting surface modelling techniques used to design the waterjet described in this research, but clearly this was a significant oversight in the case of the waterjet.

Thus the conventional calculations of blade drag losses that were implemented in the model were insufficient to capture the complete effect of the junction flows on the overall pump performance. Updated loss estimates were then extracted from the experminentally measured loss profiles, converted to estimated sectional drag coefficients and the analysis was recomputed using the coupled Lifting Surface/RANS technique. These results showed much better agreement with the experimentally measured pressure and velocity profiles as well as prediction of the pump pressure rise. However, the computed rotor torque was 10% higher than measured. It was apparent from the analysis that modelling the secondary flow losses purely in terms of section drag coefficients was insufficient to fully model the secondary flows, though the inclusion of these losses gave better prediction of the performance. One problem with the use of secondary flow drag losses in the analysis is that the prediction of these losses is difficult to conceive without experimental data or empirical models. In this analysis explicit modelling of the leakage flow was not implemented, and the details of the tip leakage effects on local blade forces may easily resolve the 10% torque discrepency.

The Euler solver differs greatly from the RANS coupling method as it deals with losses directly through entropy rise that is entered explicitly in the coupling process. Also, rotor forces are introduced as swirl, not as direct forces as in the RANS solvers. This required that drag induced swirl be included in the coupling process as well as the swirl due to typical blade forces. A method was introduced as part of this research to convert forces (blade and drag etc.) into the proper swirl and entropy rise into the Euler solver.

The Euler solver coupling method with swirl and entropy coupling implemented

gave good prediction of the waterjet pump performance and compared well to the experimental results. The overall pressure rise as well as pressure profiles and velocity profiles showed good agreement with the experiments when the losses representing those measured in the experiment were imput to the model. Validation of the tipgap modelling implemented was carried out using the the Lifting Surface/Euler solver coupling method, which showed mixed results in predicting the performance drop due to tip clearance.

In summary, the efforts implemented to capture the losses due to the tip junction flows in the waterjet gave better prediction of the performance. Though this leaves us encouraged that the numerical models are capable of producing accurate results when the input of the correct losses are input, this still leaves the effort of determining the losses up to the designer. Clearly, accurate methods to predict losses a priori would be of great use to the designer when using the design and analysis tools developed during the course of this research.

Chapter 2

The Waterjet Test Facility

2.1 Overview of the Facility

2.1.1 The Water Tunnel

The waterjet tests were conducted in the variable pressure water tunnel at the Marine Hydrodynamics Laboratory at MIT (MHL). This water tunnel facility is generally used for the testing of external flows such as flows around propellers and bodies. Figure 2-1 shows a schematic of the water tunnel. The tunnel's entire planform is approximately 6 meters square and the test section is about 0.50 meters square by 1.5 meters in length. Fluid velocity is controlled by a variable speed impeller located in the lower horizontal section of the tunnel which driven by a large DC motor. Speed control is adjusted by manually adjusting the field current via a variable resistor on the tunnel control panel. In general the impeller was not required for most of the waterjet tests as the flow was controlled to the design point via a valve in the waterjet test setup (described later). However the impeller was required when data were collected at the high flow/low pressure end of the pump curves. The tunnel could be sealed and a vacuum system could vary the test section absolute static pressure between atmospheric pressure down to as low as 5 kPa, which was used to perform cavitation tests on the waterjet pumpset as part of the waterjet experimental efforts. More details about the MHL water tunnel can be found in Kerwin [14] ,[17].
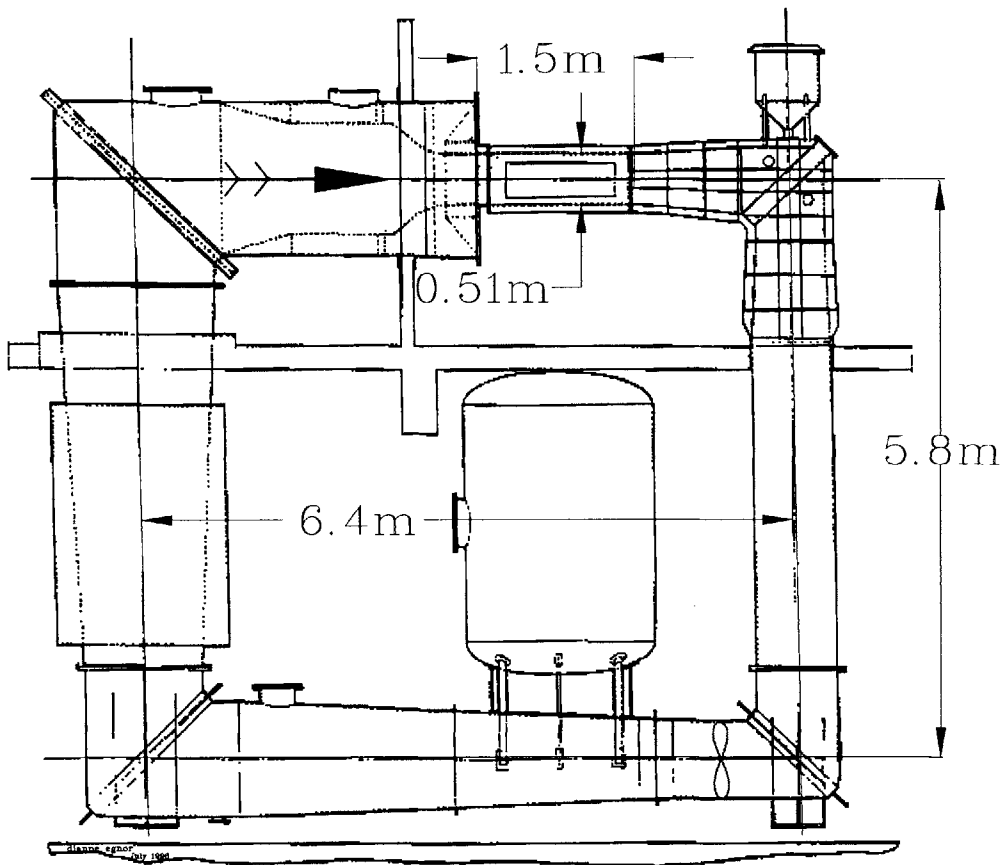
Figure 2-1: MIT Water Tunnel

2.1.2 Design of the Waterjet Test Facility

During the conceptualization of the waterjet test facility, one requirement was that the facility be fitted into the water tunnel with minimal retrofitting to the tunnel. This was achieved by installing the waterjet ductwork inside the tunnel test section to create a tunnel within a tunnel. Because access to the pump area and instrumentation was desirable, the design needed to allow the duct work to pass through the test section with the windows of the test section removed to allow access to the duct.

Figure 2-2 is a schematic of the waterjet test facility as mounted in the test section of the tunnel. Figure 2-3 is a photographof the waterjet test facility as it was installed in the water tunnel. Figure 2-4 shows a picture of the entire waterjet test facility assembled outside of the water tunnel showing the inflow nozzle, test sections, pumpset and tunnel sealing bulkheads. The ductwork included an inlet bellmouth

30

for measuring flowrate as well as inlet, midstage and exit measurement planes for measuring velocity and total pressure profiles using laser doppler velocimetry and Kiel probes respectively. Downstream of the forward bulkhead was a transition duct which reduced the duct diameter to 7.5 inches. This 7.5 inch inlet diameter was used as the length scale reference for all non-dimensionalization of the data. The reason this was chosen as the length scale is because this inlet size was constant regardless of the pump being tested, making comparison of performance from pump to pump easier.

The rotor was turned by a shaft coming in from the inlet, which was instrumented with a dynamometer for measuring torque and an inductive pickup for measuring shaft rotation rate. Unless noted otherwise, the test RPM for the rotor was 1200 rpm which corresponded to a Reynolds number based on inlet diameter and inlet velocity of 0.88×10^6. Reynolds number in this form was input to the throughflow solvers during numerical computations. The rotor had an inductive pickup encoder attached for resolving blade angular position used in phase averaged rotor exit velocity measurements . A valve at the exit of the setup was used to adjust the operating point.
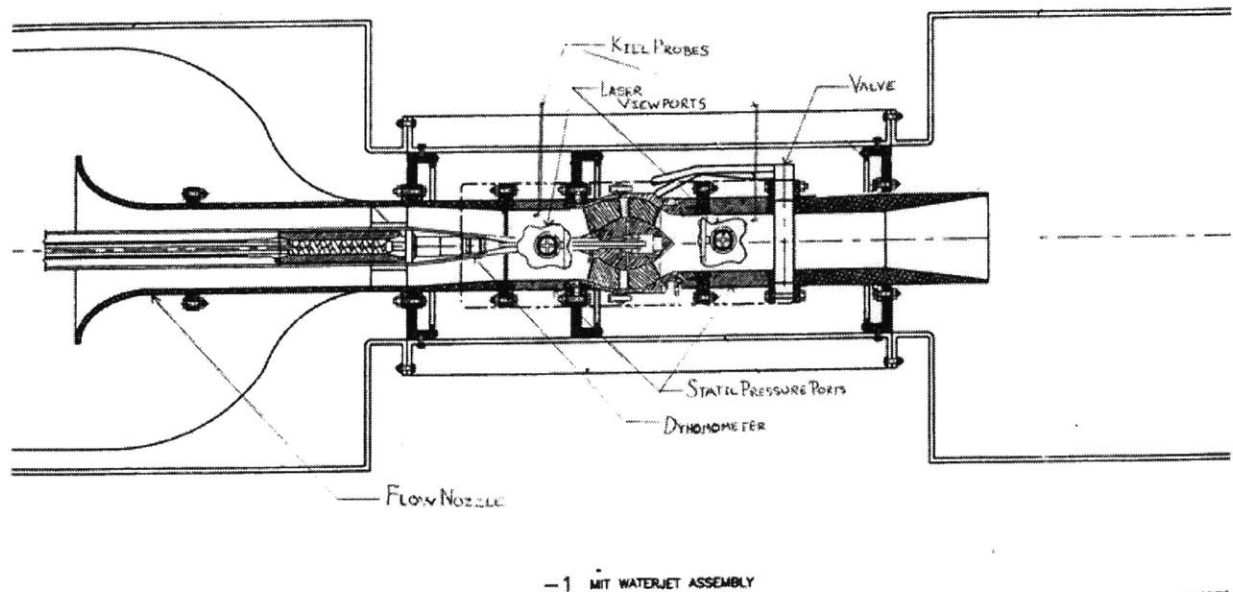
Figure 2-2: Schematic of Waterjet Test Setup

31
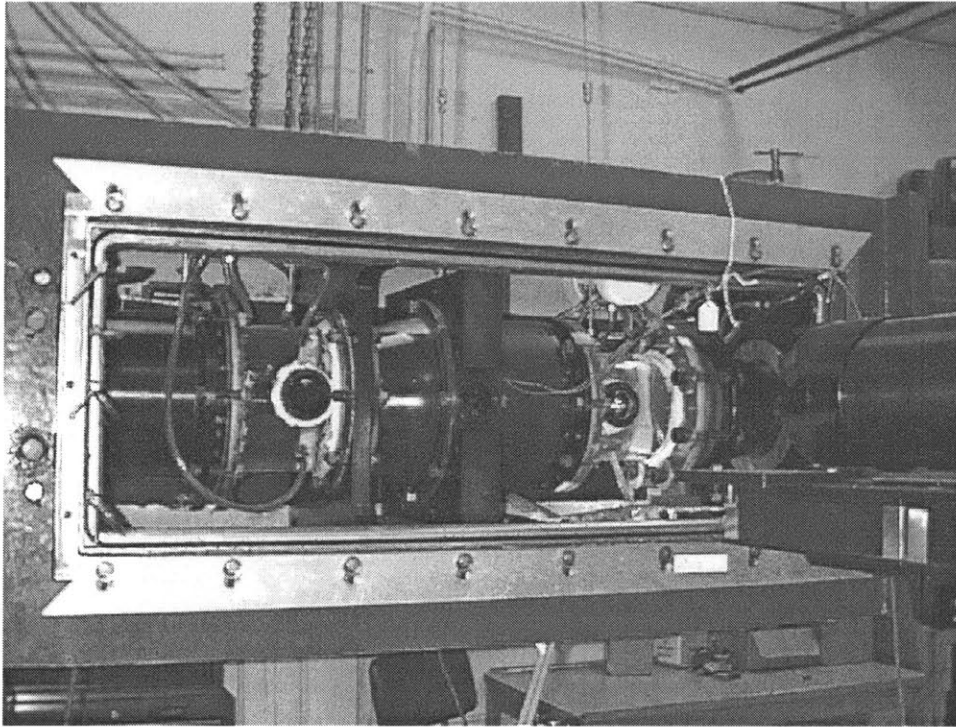
Figure 2-3: Photograph of the Waterjet Test Setup Installed in the Water Tunnel

2.2 Details of the Waterjet Test Facility Design and Instrumentation

2.2.1 Test Section Bulkheads

Since the test section of the water tunnel was normally flooded, the installation of the waterjet test ductwork required sealing the test section ductwork both upstream and downstream of the test section. This was accomplished using bulkhead plates upstream and downstream of the test section consisting of thick aluminum plates machined to fit precisely into the tunnel test section and bolted to the tunnel wall from bolt holes around the tunnel walls (these bolt holes were the only tunnel modification necessary to install the waterjet test facility). These bulkheads can be seen in Figures 2-2 and 2-4. An o-ring was installed on a chamfer around the periphery of these bulkheads and a clamping plate compressed the o-ring against the tunnel providing the seal between the bulkhead and the interior tunnel wall. The duct work on the upstream section was equiped with a flange which bolted to this bulkhead face. This
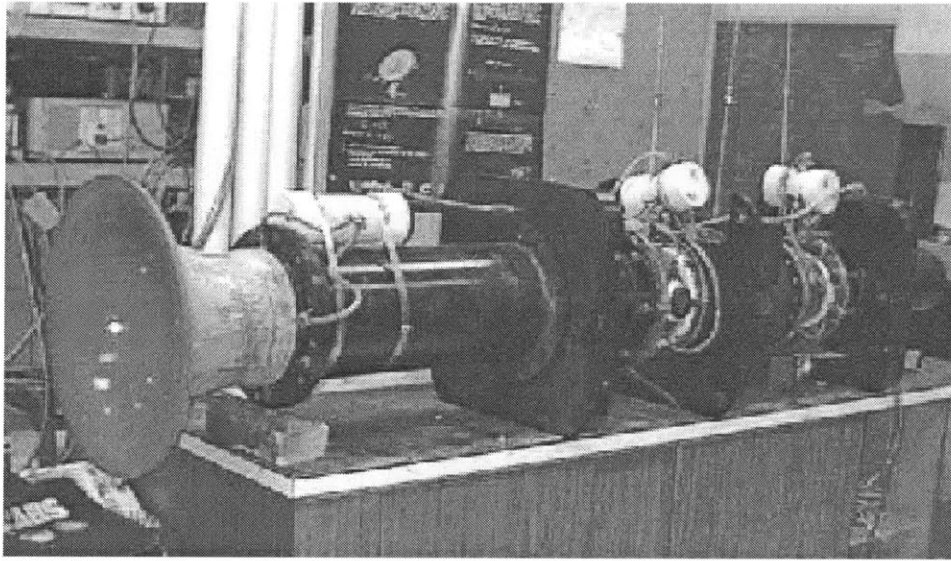
Figure 2-4: Photograph of the Entire Waterjet Test Facility Assembled Outside of the Water Tunnel

flanges contained an o-ring in a groove to seal against the bulkhead face.

The downstream outlet pipe was of constant diameter and was designed so it could slide in and out of the downstream bulkhead. An o-ring was slid onto the outlet pipe and pushed into a chamfer on the through hole of the rear bulkhead. Then an o-ring clamping ring was bolted onto the bulkhead face which compressed the o-ring against the pipe and the bulkhead chamfer creating the seal. The ability to slide the outlet pipe allowed the length of the ductwork to be changed in the tunnel installation so that different pumpsets could be tested. In fact, as of this writing, three different pumps with various case lengths have been successfully tested.

2.2.2 Inflow Nozzle

The inflow nozzle was chosen to perform two important functions. First to provide clean inflow to the ductwork with as little disturbance to the flow as possible. The second, and more important function, was to provide a simple and accurate method to measure the total fluid flowrate through the duct. Some original design concepts sought to measure flowrate by measuring the pressure drop through an orifice at the outlet of the pump. Since the pumpset disturbs the flow prior to this orifice and also

imparts an unknown amount of swirl exiting the pumpset, this would have been an inaccurate method of measuring flowrate. In fact, for flow nozzles in general, one wants clean, uniform and swirl free flow coming into the nozzle.

The inflow nozzle section was designed according to the standard set forth by the Air Moving and Control Association (AMCA). These standards were established for the construction of flow nozzles for fan testing facilities, but the standards apply well in the case of a water tunnel. These standards are published in the AMCA 210-85 standard [28].

Figure 2-5 is a photograph of the nozzle section of the waterjet test facility, showing the nozzle face, pressure taps at the throat of the nozzle and the equalizing manifold to which the four throat taps were connected. There was a straight duct section of about 2 feet long connecting the nozzle to the forward bulkhead. This length ensured that no disturbances downstream would affect the throat pressure reading. An outlet tube from the equalizing manifold fed through the forward bulkhead into the test section and on to an electronic pressure gauge. The reference pressure to this gauge was a tap connected to the water tunnel inlet section upstream of the nozzle. The flowrate then could be determined using Bernoulli's equation to convert the pressure difference between the tunnel wall and the nozzle throat, according to equation 2.1.

$$\dot{Q} = K \frac{A_{noz}^2}{\sqrt{1 - \frac{A_{noz}^2}{A_{tun}^2}}} \sqrt{\frac{2\Delta P_{noz}}{\rho}}$$

Where K is a viscous correction coefficient close to unity.   (2.1)

The flow nozzle was calibrated using the laser velocimetry system to measure the axial velocity profile at the inflow to the waterjet pump and integrating this velocity to establish the total flowrate. Using equation 2.1 the value of $K = 1.0$ was found to be within accuracy of the calibration of $\pm 1\%$. From that point on in the experiment the value of K was set to unity.
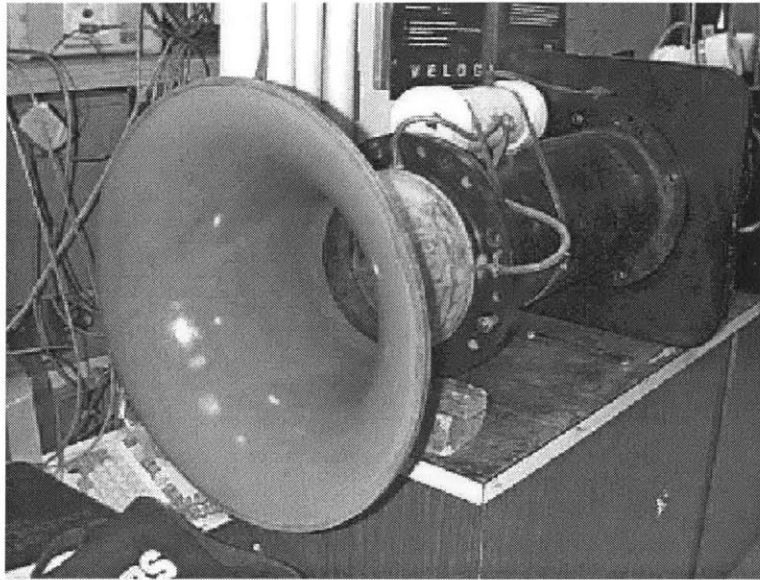
Figure 2-5: Photograph of the flow nozzle showing through taps and equalizing manifold

2.2.3 Wake Screen

Downstream of the forward bulkhead just downstream of the duct transition section, a special rotating disk was squeezed between two duct section flanges (w/ face o-rings). This disk was the wake screen mounting disk. Since it was not through bolted to the flanges it could be rotated without disassembling the ductwork and could even be rotated while tests were underway.

A wake screen could be mounted to this disk to simulate non-uniform inflow like that encountered in a real waterjet installation. Figure 2-6 shows the disk mounted against one flange with a wake screen attached. Spanner holes on the outside of the disk were used to facilitate the rotating of the disk and the disk had tickmarks every 6 degrees around the outside of the disk so that the angular position of the disk was known.

By rotating the wakescreen (and thus rotating the non-uniform inflow) full circumferential maps of velocity and pressure profiles could be mapped at each of the measurement planes using the LDV system and the Kiel probes. In a sense, it was easier to rotate the "world" around the measurement devices than rotate the devices around the duct. For the measurements used in most of this work there was no wake

35

screen in place so that the inflow was axisymmetric.
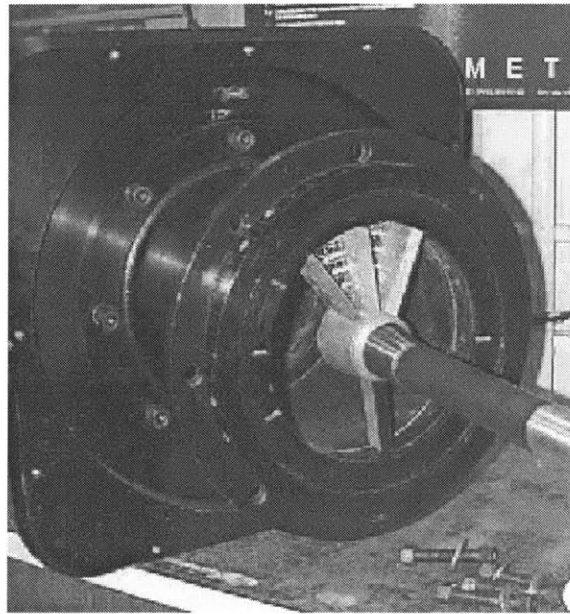
Figure 2-6: Photograph of the wake screen section with a typical screen for inducing non-axisymmetric inflow

2.2.4 Rotor Driveshaft and Dynamometer

As part of this experimental effort a new shaft system and torque dynamometer was designed and built. The original system had the dynamometer outside of the tunnel and the long driveshaft was mounted on water bearings. This shaft system had trouble reaching speeds over 1000 rpm due to excessive vibration. A new shaft system using ball bearings to support the drive shaft and an end mounted strain gauged dynamometer was used, which would not be affected by the shaft bearing friction since it was downstream of these bearings. This dynamometer was salvaged from previous experiments conducted by Burke [5] who actually built the dynamometer gauge. The dynamometer strain gauges were stripped and new semiconductor gauges were fitted to measure both torque and thrust. Though the semiconductor gauges had high response, there zero tended to drift slowly over time. Also the thrust gauge became inoperable part way through the testing and was not used. In hind sight, fitting the gauge with good old platinum strain guages would have probably been

a better choice, even given the output response that was an order of magnitude lower than that of the semiconductor gauges. With a 5 volt supply feeding these semiconductor gauges the typical torque output for the rotor running at the test speed an output of about 50 millivolts was measured, Platinum gauges would have put out about 5 millivolts, but this signal is still easy to accurately measure using high resolution voltage measurement devices.

Figure 2-7 shows a drawing of the dynamometer fitted into the end of the shaft housing. A sealed connector attached to the gauge where it passed down the center of the shaft and connected to a set of slip rings. Then the cables from the slip rings connected to a strain gauge conditioner which output the measured voltage signal. To calibrate the dynamometer for torque, a calibration device was attached to the end of the dynamometer and the shaft was held rigid. Figure 2-9 shows a photograph of this calibration device showing two arms on either side of the device from which known weights were hung. On one side the weights hung straight down and on the other the hanger cable passed through a pulley above the calibrator so the applied wieghts would pull up on the arm . In this fashion a pure torque could be applied to the dynamometer assuming equal wieghts were applied to each side.

The distance between the hangers was measured as well as the weights so the calibration torque could be calculated as the total arm distance times the total weight. Figure 2-9 shows the resulting calibration curve for the dynamometer using the procedure described above. As expected the dynamometer voltage is linear with torque. One major problem encountered with the dynamometer torque gauge was the slow drift of the zero with time. It was found, however, through subsequent calibration that the calibration sensitivity (the slope of the calibration curve) was not affected measurably by the zero drift. During tests the zero value was recorded often between tests. The uncertainty of the zero accounted for most of the torque measurement uncertainty which was calcultated to be $\pm 2.0\%$ at the torque values measured during the waterjet testing.
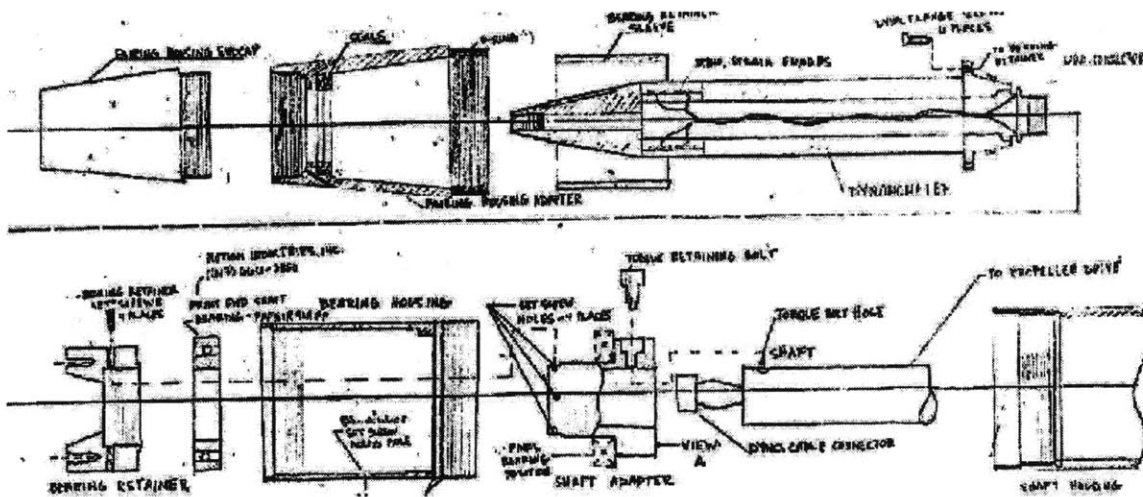
Figure 2-7: Drawing of the Driveshaft/Dynamometer System

2.2.5 Profile Measurement Planes

Profile measurements were conducted at special measurement planes located at the inlet of the waterjet, between the rotor and stator and at the exit of the waterjet. Figure 2-10 shows the measurement plane flange located between the rotor and stator. On the side of this flange was a laser window with "crosshair" slots cut in the flange to allow the four laser beams to pass through (two beams for the axial velocity measurement and two beams for the tangential velocity measurement. Located at the top of the flange was a Kiel probe mounted in a compression fitting so it's measurement head could be moved radially across the duct. A bracket mounted to the laser traverse could be connected to the Kiel probes so that this traverse could be used to precisely position the probe during the profile measurements of total pressure. The inlet and outlet measurement planes were each fitted with four wall taps connected to an equalizing manifold similar to that used for the nozzle throat pressure taps (shown in Figure 2-5). The inlet wall static tap readings were used as the reference pressure for all the total pressure measurements, as well as the reference for the outlet wall static pressure taps, which were used to measure global pump pressure rise.

38
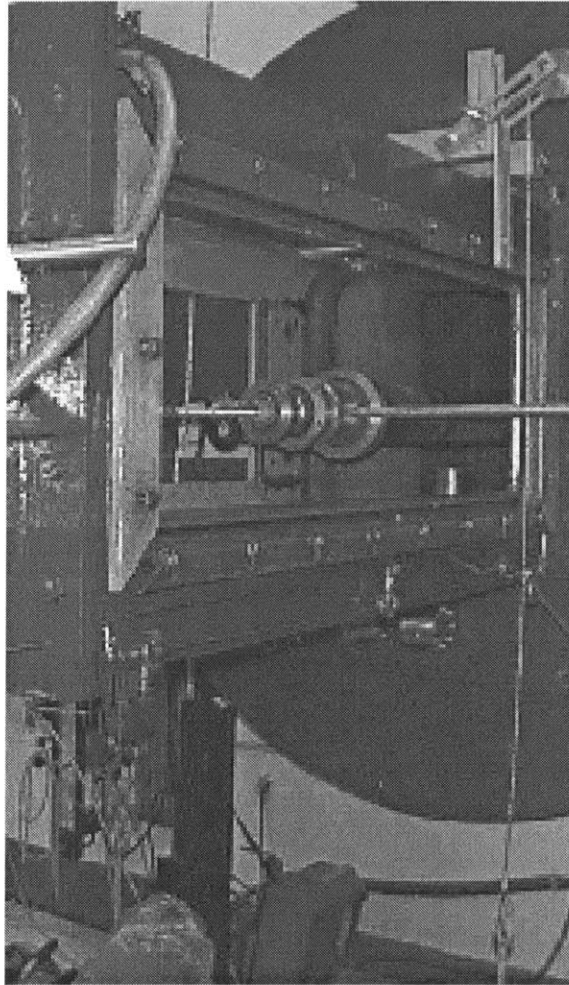
Figure 2-8: Photograph of the Torque Calibration Rig Mounted to the Dynamometer

2.2.6 Rotor Encoder and Phase-Averaged Velocity Measurements

The blade position encoder consisted of a six toothed metal disk attached to the rotor rear face with inductive pickups located in the hub of the stator as shown in Figure 2-11. The signal from the inductive pickups was fed directly into the laser signal analyzer which measured both the velocity and arrival time of a particle in th fluid. By comparing the arrival time of a particle measurement to an encoder signal from the rotor the postion (or phase) of the rotor blade at the time of the measurement could be determined. A measurement bin of one degree was set over the 360 degree blade rotation cycle and any measurement determined to fall in a particular bin was averaged with the other particle measurements in this bin to determine the phase-
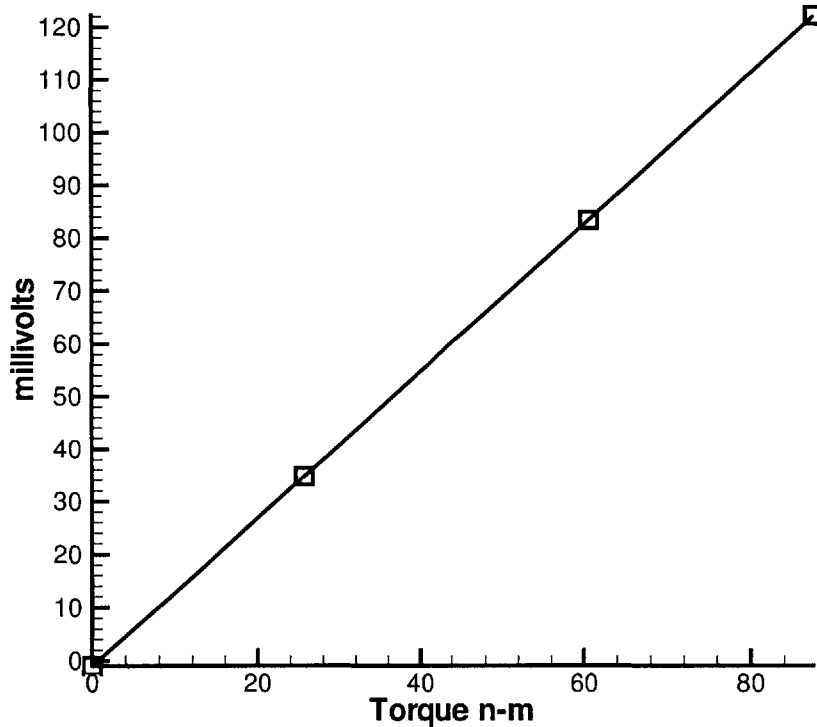
Figure 2-9: Typical Torque Calibration Curve

averaged velocity. This data was used to capture the periodically unsteady flow
caused by the blades and their wakes.

2.2.7 Laser Doppler Velocimetry System

The LDV system used to measure fluid velocities was a two component system that
could resolve the streamwise and tangential component of velocity. It uses an Argon
laser with maximum power of about six watts. The laser optics in the system were
manufactured by TSI. The Signal conditioner was a 2-component FVA system from
the DANTEC Measurement Corporation. The laser optics were mounted to a traverse
so the position of the measurement point could be precisely positioned. Figure 2-12
shows a picture of the LDV system and traverse taking a measurement in the duct
of the waterjet test facility. Figure 2-13 shows a schematic of the components of the
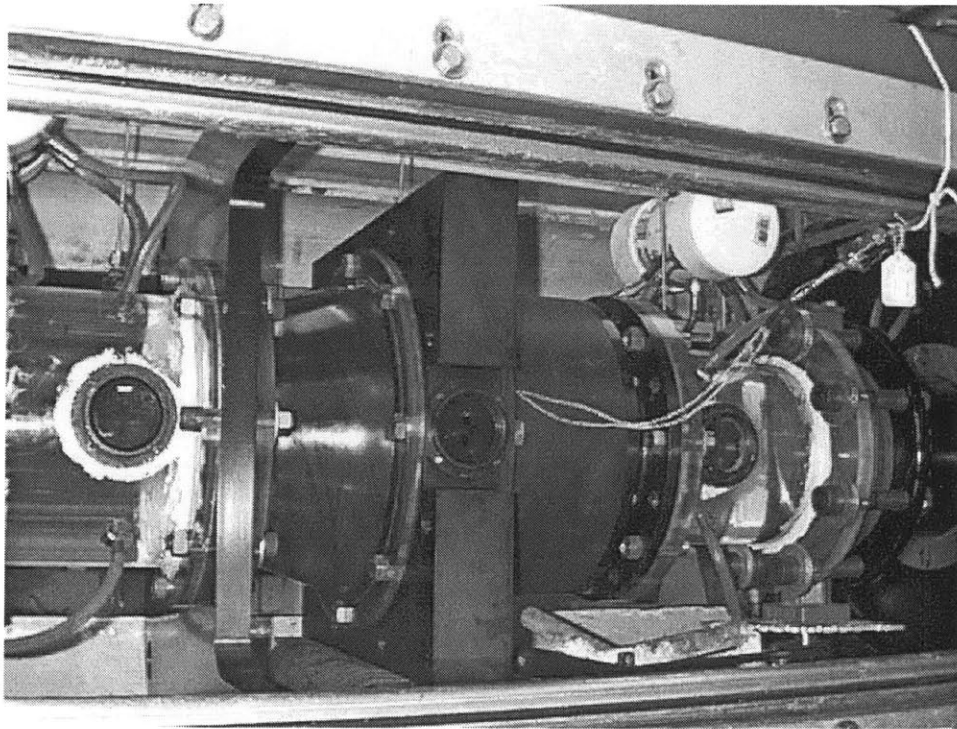
Figure 2-10: Picture of the Inflow Midstage and Exit Measurement Planes showing the Laser Windows and Kiel Probes

LDV system.

A good overview of the principles of LDV measurements can be found in Durst et al. [8]. Laser doppler velocimetry works by first separating the different laser frequencies in a prism so each color can be used for a different component of velocity. Each beam then gets split into two beams and aligned and focussed through a lens so that they cross at a point, which is actually an ellipsoid of about 1 mm by 0.2 mm in size. Since the beams are plane wave at the same frequency, when the beams cross they form an interference (or fringe) pattern The fringe spacing is known from the frequency of the beam and the optics. When a shiny particle in the fluid passes through the crossing volume it encounters these fringes of light and dark regions sending out a pulse of light each time it hits a bright spot. Each set of periodic flashes for a particle, or bursts as they are called are recorded by a photoresistive pickup, amplified and sent back to the LDV signal conditioner. From each burst the time between pulses is determined and since the fringe spacing is known the velocity
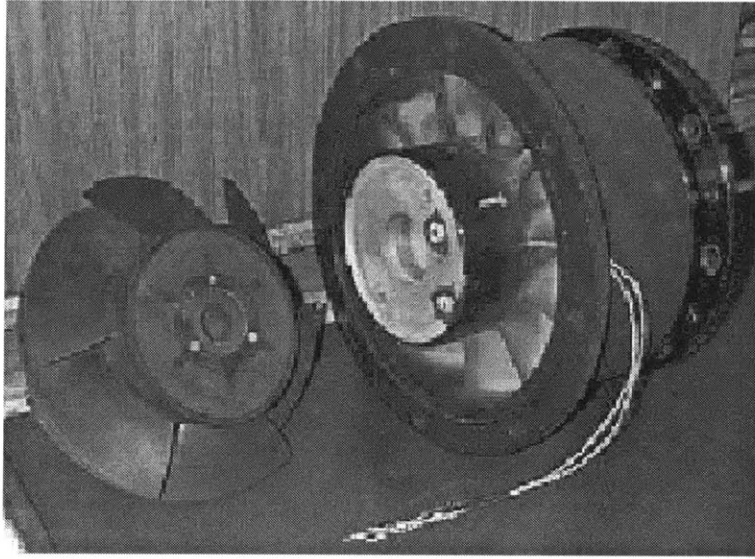
Figure 2-11: Picure of the Rotor w/ Encoder and Pickups in Stator Housing

of the particle can be calculated. One problem encountered is that there is no way to tell if the measured velocity is positive or negative. This is remedied by shifting the frequency of one of the beams so that the fringe pattern moves across the crossing volume at a known rate. This provides an offset in the measured velocity such that all measured velocities are positive (relative) due to the moving frnge pattern. By the subtracting off this fringe velocity both positive and negative velocities can be resolved. This feature is useful for measurements where the direction of the velocity is not known, such as the direction of the swirl velocity leaving the waterjet stator.

Though it was stated that the fringe spacing in the laser crossing was set by the optics, it is difficult to precisely measure these optical parameters. In order to calibrate the laser velocity measurement, a "spinning disk" calibration procedure was used, in which a disk spinning at a constant rate rotates in a plane perpendicular to the beam path. The velocity at which a point on the surface is moving can be calculated from the following equation:

$$v_t = \omega \times r \tag{2.2}$$

where v is the velocity of the measurement point, ω is the rotation rate, and r is the
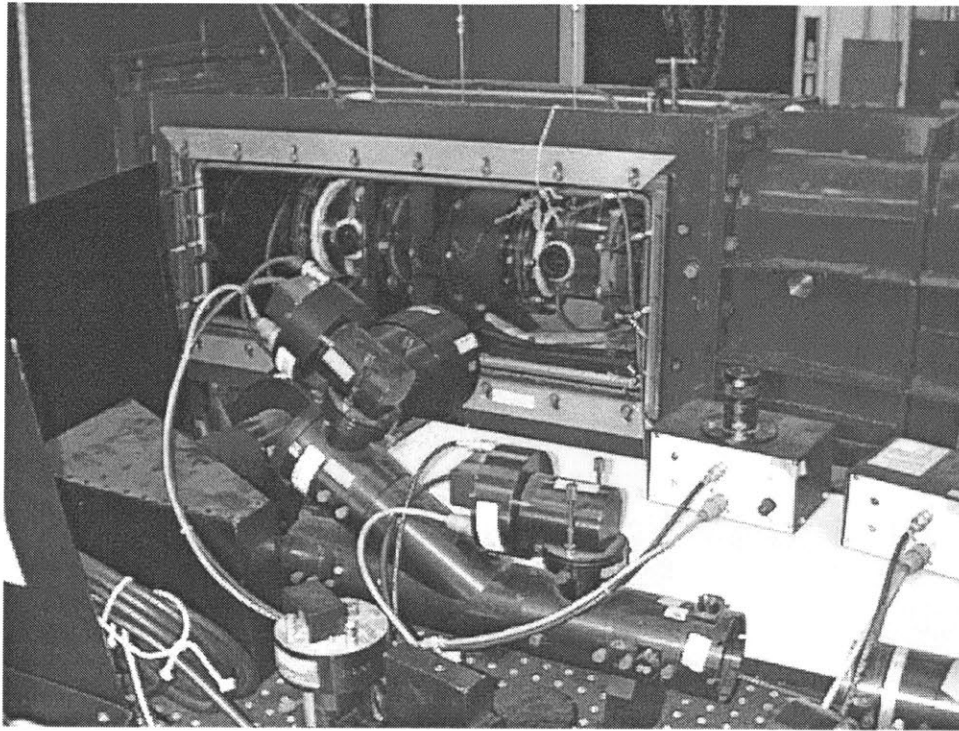
Figure 2-12: Photograph of the Laser Doppler Velocimetry System

distance between the measurement point and the center of rotation. A schematic of this spinning disk calibration setup is shown in Figure 2-14 and a photograph of the actual laser calibration setup is shown in Figure 2-15.

This spinning disk method allows the calibration of both components simultaneously with the accuracy of the calibration being determined by the laser traverse system positioning (r) and a photo-optic rpm sensor circuit and frequency counter (ω). The uncertainty analysis for the LDV velocity shows the uncertainty in velocity is within $\pm 0.4\%$ This method also allows the measurements and correction of beam parallelness to the traverse axes. Cross talk between velocity components was measured to be less than 0.1% of cross component reading. Using this spinning disk method, the laser was calibrated to $\pm 0.5\%$ of velocity reading.

In a two component system the beams of each component are made to cross at the same point. This allows correlated velocity measurements where both components of an individual particle are measured at once. If a signal is measured in one component and not in the other component then the measurement is rejected. This type of
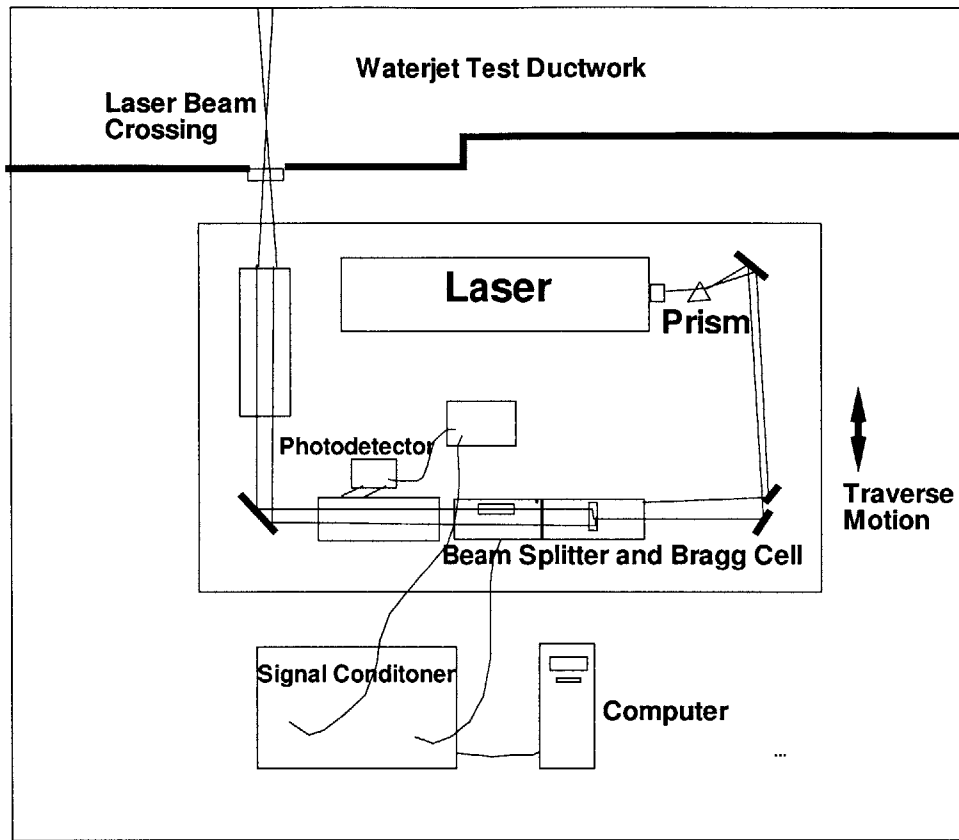
Figure 2-13: Schematic of the Laser Doppler Velocimetry System

filtering improves the fidelity of the data. Since velocities of individual particles are measured, many particles collected at a point are required to resolve the mean velocity values accurately. In general, for the mean velocity measurements collected in these experiments a sample size of 400 particle per measurement point was used, which gave decent results. For the phase-averaged velocity measurements, however, each "point" consisted of 360 bins so in the interest of collection time the average bin count was set to 100 particles. The bin data was found to be relatively uniform even across the wakes indicating uniform particel seeding. The problem with teh relatively low bin count this is that the occasional outlier can give an unrealistic spike in the profile. To alleviate this problem the phase-averaged data was processed through a numerical filter which computed the standard deviation, removed outliers that fell outside of 3 standard deviations and then recomputed the statistics for the remaining

44

samples. This method worked reasonably well at smoothing out the spikes in the phase-averaged data profiles.More details on the accuracy and error analysis of laser measurements of the MHL system can be found in Lurie [25].
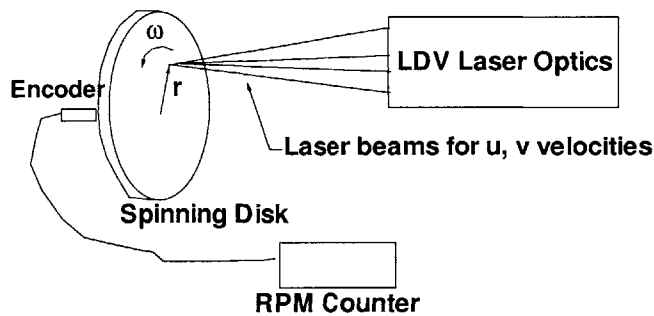
Figure 2-14: Schematic of the LDV Calibrator

2.2.8 Kiel Probes for Total Pressure Profiles

The total pressure profiles were collected using Kiel probes traversed across the duct at the measurement planes. Figure 2-17 shows a schematic of the Kiel probe head showing its measurement tube shrouded by a duct. This duct redirects the local flow into the measurement tube so it gets an accurate measurement of the fluid stagnation pressure without having to precisely align the probe with the local flow. In the case of a rotor exit flow, significant deviation in the inflow angle exists as the blades rotate. The Kiel probe appears to have no problem resolving the mean stagnation pressure of this unsteady periodic flow. Figure 2-16, produced from data published by the manufacturer [36] shows the sensitivity of the Kiel probe reading to yaw and pitch angle. As can be seen from this plot, a unique advantage of the Kiel probe is that its

45
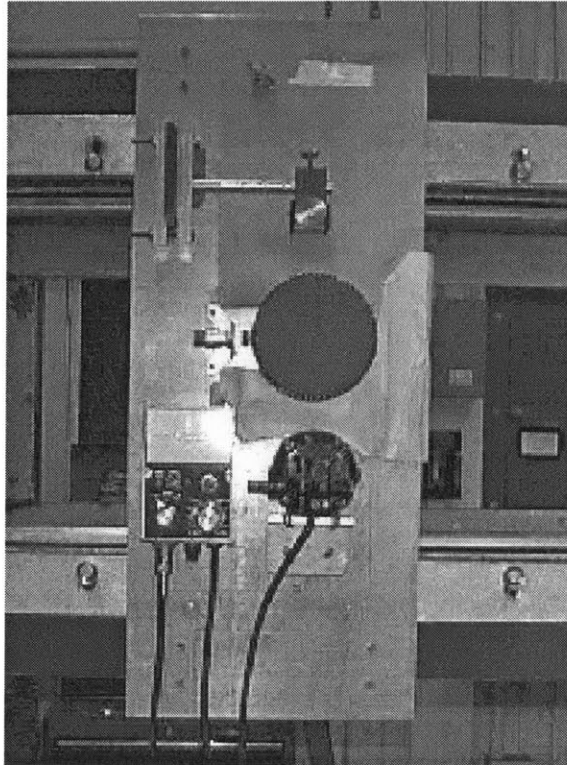
Figure 2-15: Picture of the LDV Calibrator

measurement of total pressure is insensitive to inflow direction for up to 50 degrees of yaw and 40 degrees of pitch before significant drop in accuracy ($> 1\%$) is seen. Since the stagnation pressure profiles across a blade row are a direct measurement of the fluid losses (at least in incompressible flow) the direct measurement of this stagnation pressure gives directly the bladerow loss profiles. This amazing ability of the Kiel probe to measure these quantities with ease by the experimenter makes the Kiel probe, in the author's opinion, the most valuable measurement instrument for detailed waterjet bladerow testing.

2.2.9 Pressure Measurement

All pressure measurements made during the testing of the waterjet were measured using electronic strain-gauge type pressure transducers connected to strain gauge conditioners. The gauges were calibrated against a known head of pure water using a water manometer system that was refitted for the purpose of calibratating pressure

46
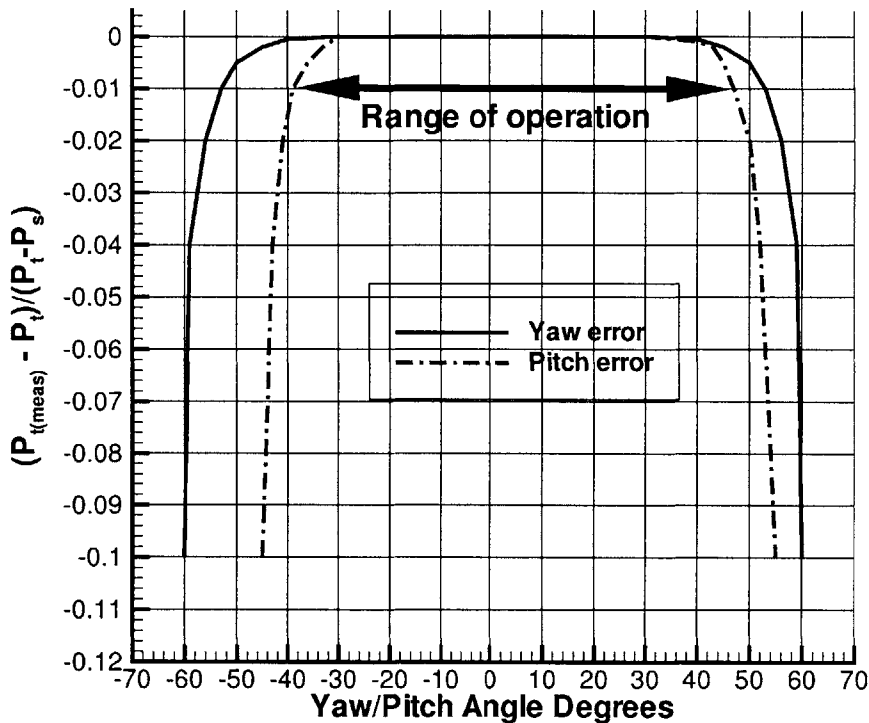
Figure 2-16: Plot of Kiel Probe Measurement Sensitivity to Yaw and Pitch (Data from reference [36])

gauges. A photograph of the calibration apparatus is shown in Figure 2-19 and the details of the calibration method is outlined in [3]. Essentially tubes from each side of the differential pressure guage were connected to a water manometer and the water in one side was pumped to some height relative to the other side. By measuring the height difference in the two columns the pressure applied could be calculated by: $\Delta P = \rho g \Delta H$ where g is the acceleration due to gravity. A typical calibration curve obtained from this method is shown in figure 2-18.

The uncertainty of the calibration method depends chiefly on the accuracy of water column height measurement ($\pm 2mm$). The uncertainty in static pressure was computed to be ± 20 Pascals.
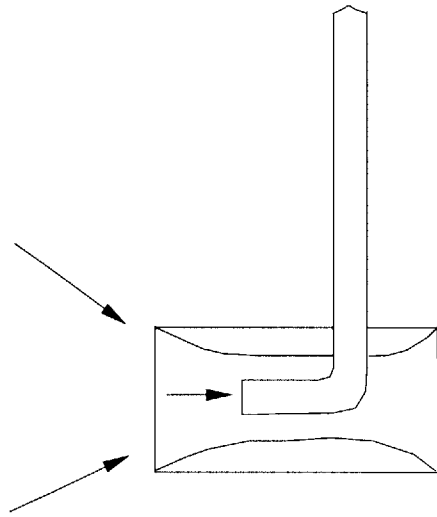
Figure 2-17: Schematic of a Kiel Probe Head

2.2.10 Traverse Positioning for pressure and velocity profiles

Laser position was measured by digital traverse/encoder system. The laser positioning system has a resolution of .001 mm and relative accuracy of better than 0.01mm . For the purposes of error analysis, this position error was negligible. The dominant error in the positioning data was establishing the reference position. This error was typically +/- 0.5 mm therefore the offset error was roughly fifty times the relative positioning accuracy. The laser positioning system was also used to position the Kiel probe for stagnation pressure profile experiments. The traverse system is shown in Figure 2-12.

2.2.11 Electronic Data Acquisition System

The conditioned signals from the electronic pressure gauges, the dynamometer torque gauge and the rotor RPM gauge were fed into a 12 bit computer data acquisition card used to simultaneously collect these data at each measurement condition. For all of the gauges the voltage range was set so that the mean value of the measurement was at least half the voltage range. For a 12 bit system this corresponded to a data aquisition resolution of 0.1% which was generally far better than the accuracy of the gauges themselves.The system was set to take 10000 samples over 10 second period
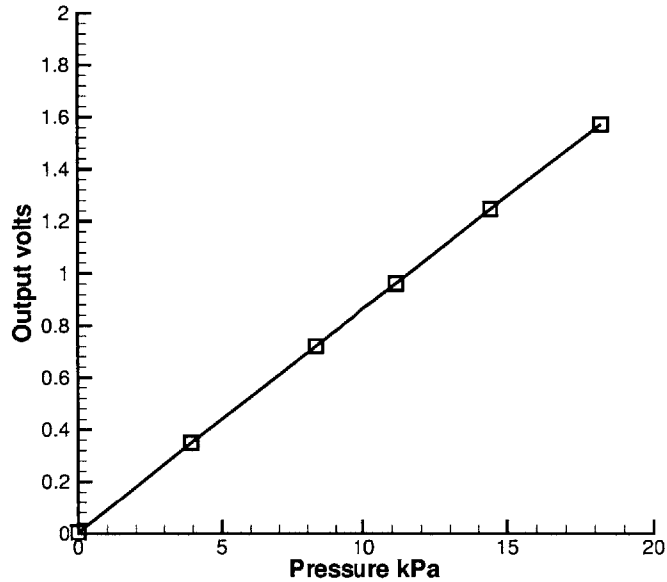
Figure 2-18: Typical Pressure Guage Calibration Curve

and output the average of these samples for each of the gauges. Signals from the gauges were checked using a spectrum analyzer to ensure that the signal to noise was high so that measurement aliasing would not be a problem. In this fashion accurate mean values could be determinend without the error typically introduced when by manual data collecting. Since this type of data acquisition hardware is of low cost and easily setup, it was well worth the effort to install such a system as part of the waterjet test facility. Typically as part of a test sequence, data was collected with the waterjet rotor turned off before and after the measurement sequence and this data was used to establish zero references, which was needed especially for the torque guage whose zero tended to drift in time.

2.3 Measurement Procedures

2.3.1 Pump Performance Curves

Overall pump performance characteristics for waterjets was generally measured in the form of head-capacity curves. To conduct these tests in the waterjet test facility, the
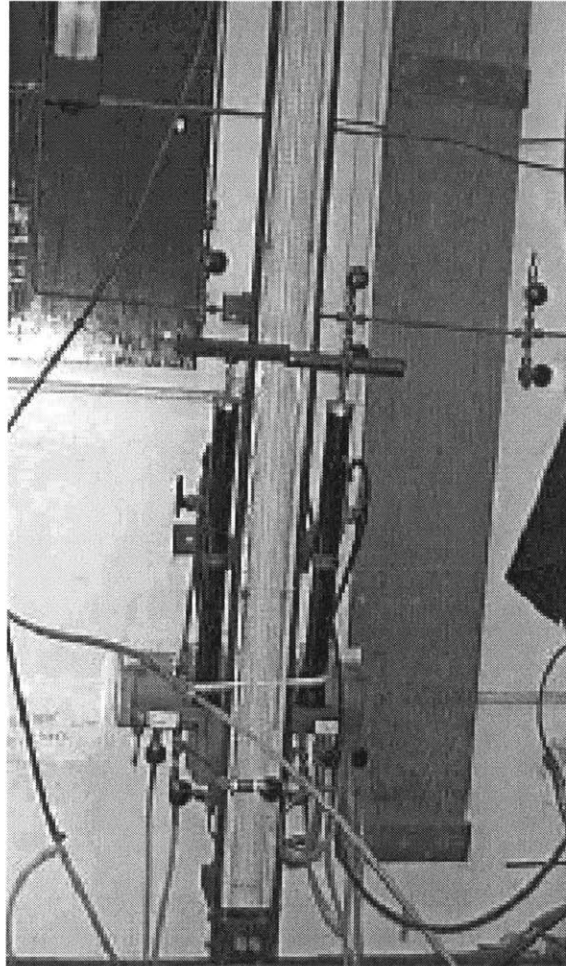
Figure 2-19: Photograph of the Pressure Gauge Calibration System

pump rotor was started and set to a steady test speed and the downstream control valve was varied to vary the flow through the pump. Measurements of nozzle pressure (flowrate) wall static pressure rise between the pump inlet and outlet and rotor rpm and torque were collected at each flow point. Figure 2-20 is a typical pump curve generated for the waterjet pump showing total head rise as a function of flowrate, normalized by the design flow and head. The torque curve is shown in this figure as well. For the purposes of generating pump performance curves, the pressures measured were average wall static pressure values. To estimate the the total pressure rise(or head rise) through the pumpset this wall static pressure rise was assumed constant across the duct. To compute the dynamic head (which is added to the static

head to give the total head rise) uniform axial velocity at the pump exit and inlet was assumed and the dynamic head rise due to any swirl in the exit flow was neglected. Thus the total pump head rise was estimated by using equation 2.3.

$$\Delta P_{tot} = P_{out.static} - P_{in.static} + \frac{\rho \dot{Q}^2}{2}[\frac{1}{A_{exit}^2} - \frac{1}{A_{inlet}^2}]$$ (2.3)

Pressure rise in all pump curves presented in this work were computed in this fashion. When comparing the value of the mean total pressure rise as computed by flow weighting the total pressure profiles (a more accurate measure of the total pressure rise) the difference was less than $\pm 2\%$. So the more crude estimate of total head rise was felt to be adequate to report the global pump performance characteristics of the pumpset . In fact, much of the data published in commercial pump curves were taken in a similar fashion and though only approximate, this methods is a least common practice in the field. The alternative would be to take detailed profile measurements at each operating point and this would be simply too time consuming.

2.3.2   Tipgap Studies

Since the rotor is a mixed flow device the mean tip clearance could be easily adjusted for tipgap studies by moving the driveshaft fore or aft(and hence the position of the rotor in the duct). Figure 2-21 shows a picture of the shaft positioning mechanism, which could repeatably moved by a fraction of a millimeter which meant that the mean gap could be set to $\pm t/D_i = 0.0002$. It should be noted that this method of adjusting gap did not produce a constant tipgap along the blade chord. Thus the mean gap was calculated as the average radial gap along the blade tip chord. Both pump curves and mean velocity profile data were collected at various tip gap settings as set by this method. The range of mean tip gaps measured during this experiment was $t/D_i = 0.0013$ to $t/D_i = 0.0065$, where t is the mean rotor to duct clearance and D_i is the inlet duct diameter.
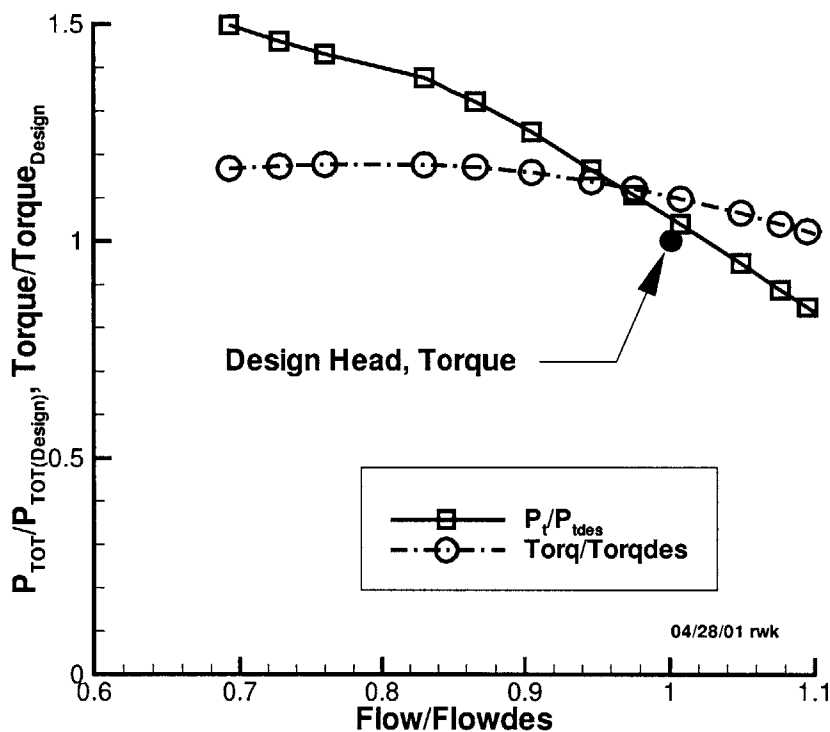
Figure 2-20: Example of a waterjet pump curve

2.3.3 Mean Velocity and Stagnation Pressure Profiles

Using the LDV system mean velocity profiles were collected across the duct at the inlet, midstage and outlet measurement planes. The LDV measurements collected 400 samples per point to determine the mean tangential and axial velocity at roughly 25 radial points across the duct. Data points near the hub and duct were more tightly spaced to better capture the boundary layer effects in these regions. Similar radial spacing was used for the stagnation pressure profile data. The collected velocity and pressure data at one operating condition was then interpolated so that coincident interpolated data could be used for the loss calculations and energy balance calculations discussed in chapter 4.

When measuring profile data at the outlet plane, the assumption of axisymmetry was no longer all that valid because of the presence of the stator wakes. To average
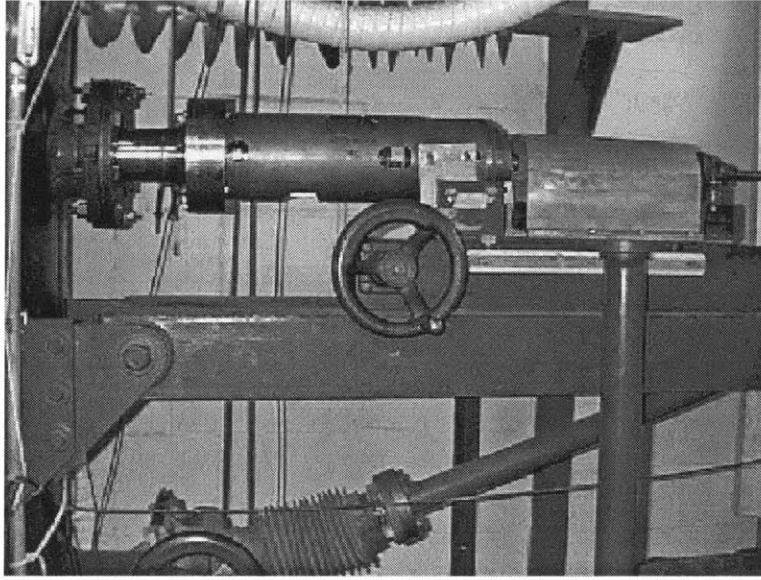
Figure 2-21: Picture of the shaft positioning apparatus

out the non-axisymmetric variations in the profile measurements the 11 bladed stator was rotated in 45 degree increments to give eight angular stations of data. the results from all these profiles were averaged. The 45 degree incremental spacing was dictated by the bolt pattern on the stator housing (eight equally spaced bolts on both sides held the stator set in place). Figure 2-22 shows the mean velocity profile and the profiles at the eight individual positions showing the angular variation in velocity due to the stator wakes. The effect of angular variations on the stagnation pressure measurements was similar to Figure 2-22 but the deviations were smaller.

2.3.4 Phase-Averaged Velocity Measurements

The phase-averaged velocity measurements were conducted at the midstage (rotor exit) plane to obtain the details of the rotor blade wakes as a function of radius. These data were collected at the design flow condition at each of the radii where mean velocity data were taken during the mean velocity profiles measurements. For each measurement location 36000 samples were taken and distributed into 360 angle bins with a one degree bin spacing, giving an average of 100 samples per bin. The points nearest the hub were not able to collect this many samples in reasonable time
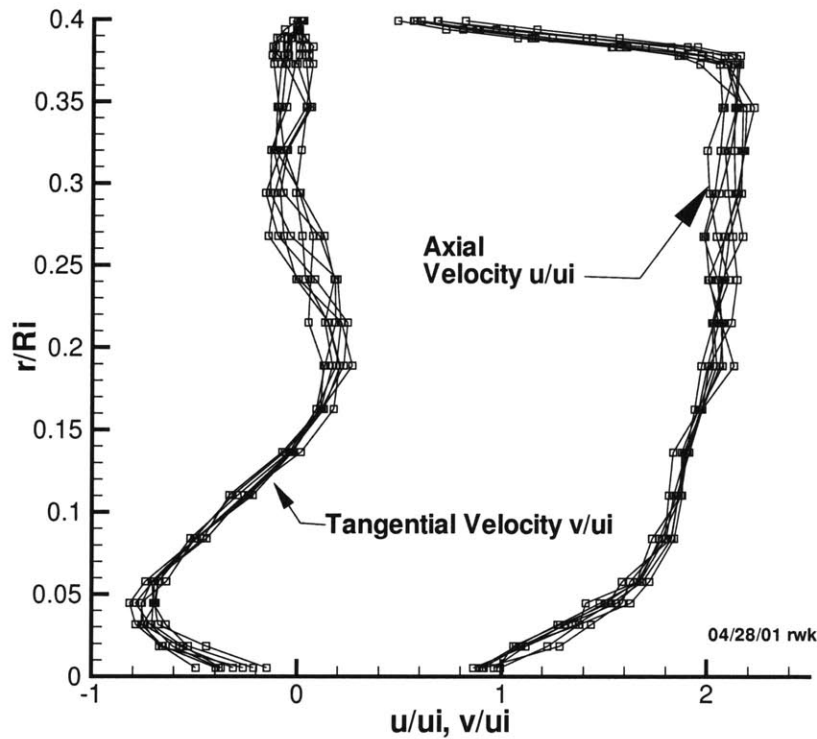
Figure 2-22: Mean velocity profile across the outlet duct at eight different angular stator positions; The stator set had 11 blades

due to low data rate at these inner radii, where in the worst case, the data collection fell to about 15 samples per bin. Fortunately, the most interesting flow phenomenon happened near the tip of the rotor in the region of the rotor tip/duct junction. The outlier removal scheme desribed earlier was applied to the data which provided a reasonable smoothing of the data in a sensible way. Also it was found that data was uniformly distributed for all the bins indicating that particle seeding was uniform even in the blade wakes.

Due to velocity bias error inherent in LDV particle measurements, the accuracy of mean velocity measurement can be improved by taking the mean of the phase averaged data rather than the mean of all the particles measured at that point. This correction was not used in the data analysis of the mean velocity data but accounted for less than 2% in the areas of high blade wake variation near the rotor tip (i.e. the

worst case area). This error was not significant enough to change the results of this work but should be noted none the less.
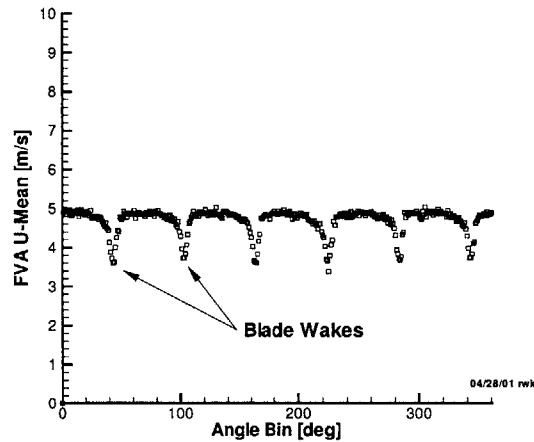
Figure 2-23: Sample of Phase-Averaged Velocity Data at One Point Behind Rotor

2.3.5 Non-uniform Inflow Measurement Procedure

Though non-axisymmetric inflow was not modelled in the numerical work of this research, some data were collected in a non-uniform inflow and are presented here merely to demonstrate the capability of the waterjet test facility in conducting non-axisymmetric inflow experiments. A wake screen was fashioned to give a non-uniform inflow distribution resembling that seen by a typical waterjet rotor. Since the typical waterjet inlet is an elbow through which the flow has to pass over a drive shaft, there is a velocity shadow due to the flow over this shaft that causes a velocity defect at the top part of the duct. The wake screen shown in Figure 2-6 was installed in the wake screen disk and the mean velocity produced by this screen was measured at the inlet. This was done by rotating the wake screen manually and taking mean velocity profiles at the duct. Radial surveys at 12 degree spacing increments were made in the open region of the screan but this angular spacing was decreased to 3 degrees near the top of the wake screen where the velocity gradients in the angular direction were expected to be high. Figure 2-24 shows the measurement of the axial profile produced by the wake

screen as measured in the described fashion. Once the non-uniform inflow was created additional mean flow and pressure field maps were obtained at the midstage and exit velocity planes. As well, pump curves in unsteady inflow were measured to determine the effect of the unsteady inflow on overall pump performance by comparing these results to the steady inflow results. The main reason for creating the non-uniform inflow, however, was to study the effects of the non-uniformity on rotor cavitation. Since the unsteady inflow causes large changes in the incoming angle of attack that the rotor blades see, it worsens the cavitation performance of the rotor. Though cavitation data were collected during this project, is not presented as part of this research due to the proprietary nature of the data to the funders of the experiment. Suffice it to say that the wake screen system was successful in creating the type of inflow typical to a marine waterjet and extended the useful capability of the waterjet test facility.
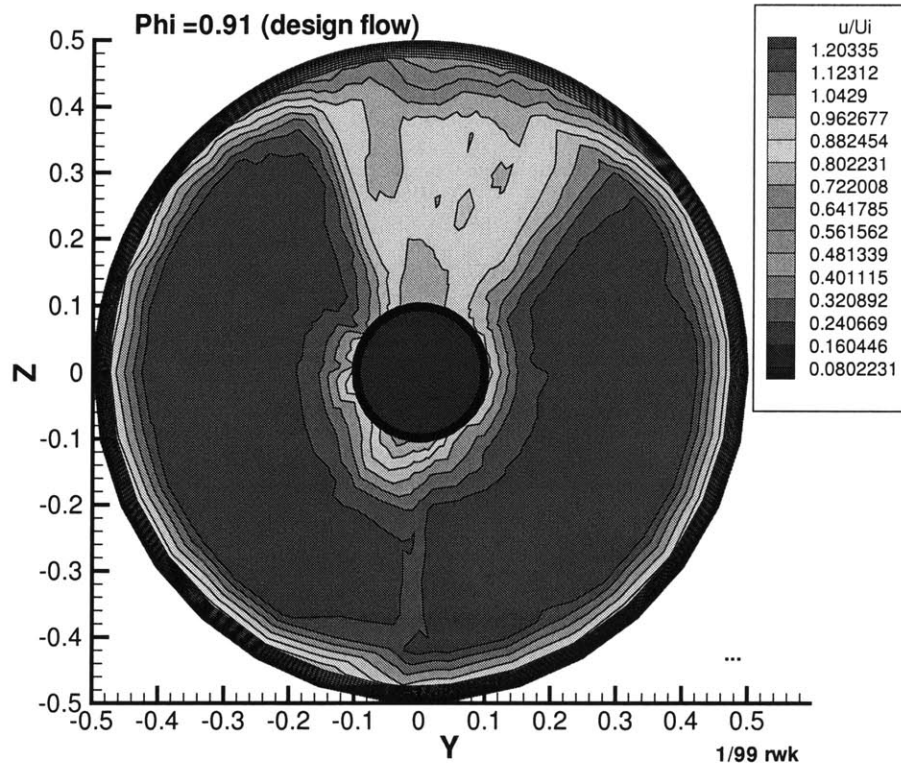
Figure 2-24: Inflow Axial Velocity Field produced by the wake screen of figure 2-6

Chapter 3

Experimental Results

3.1 Waterjet Experimental Results

3.1.1 Pump Performance Curves vs. Reynolds Number

To test the effect of Reynolds number on pump performance the pump was operated at various rotational speeds. The full scale design inlet Reynolds number for this pump was intended to be about 1.5×10^6 based on inlet diameter and velocity at the design flow. This Reynolds required a test shaft speed of about 2000 RPM which was above the capability of the dynamometer shaft . Due to vibration considerations, 1500 rpm was the maximum speed the driveshaft was driven during testing, but an even lower test speed would result in less vibration during testing. Thus it was intended to show that the pump performance at the model test speed of 1200 RPM was sufficiently insensitive to Reynold's number that the performance at the model speed was a sufficient representation of the full scale performance. Figure 3-1 shows the pump performance curves for three different pump speeds corresponding to inlet Reynolds numbers of 0.66×10^6, 0.88×10^6 and 1.1×10^6, which represent model test speeds of 900, 1200 and 1500 rpm, respectively. Figure 3-1 shows that there was little difference between the pump performance at the 900, 1200 and 1500 rpm conditions. These curves were conducted at a tip clearance of $t/D_i = 0.0025$, which represented the smallest gap that could be reliably tested in the facility without the rotor rubbing the casing during testing (case rubbing would yield biased torques readings). Since the effect of test speed on pump performance was insignificant it was felt that the

1200 rpm test speed would be sufficient to represent the pumps performance.
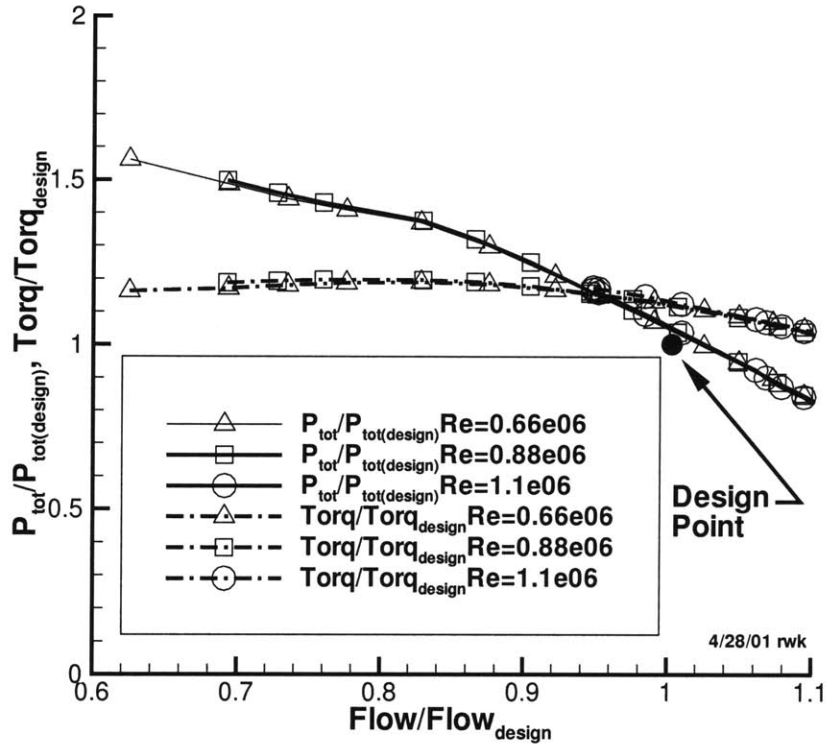
Figure 3-1: Pump Curves at Various Rotor Speeds

The intended design point is also shown on Figure 3-1 and shows that the actual pump pressure rise came very close to the intended design. However, the torque predicted by the design process underpredicted the actual torque by 10% at the design flow condition. This was not unexpected because the effect of secondary flow losses was not included in the design process. As will be shown later, the effect of secondary losses were the dominant loss mechanism in the rotor.

3.1.2 Effect of Tip Clearance on Overall Pump Performance

Pump curves were generated at various tip clearances ranging from $t/D_i = 0.0013$ to $t/D_i = 0.0064$. Figure 3-2 shows the performance curves resulting from these tests. The effect of the tip clearance on the test pump was very significant on both the pump

pressure rise and the torque of the rotor. Also, though not shown explicitly in this figure, there is a significant drop in efficiency as the tipgap increases. Figure 3-3 plots the torque, total pressure rise and efficiency at the design flow condition as a function of tip gap. Head rise and torque are relative to design values. Figure 3-3 shows that the performance drop is relatively insensitive for small clearances but falls quickly as the gap is widened. For example, the performance drop of the $t/D_1 = 0.0013$ case relative to the "zero" gap case was less than 1% on P_{tot}, torque and efficiency. If the gap was increased to $t/D_i = 0.00640$ then the performance drop was a substantial 12.5% on P_{tot}, 4.5% on torque and 7 points on efficiency.
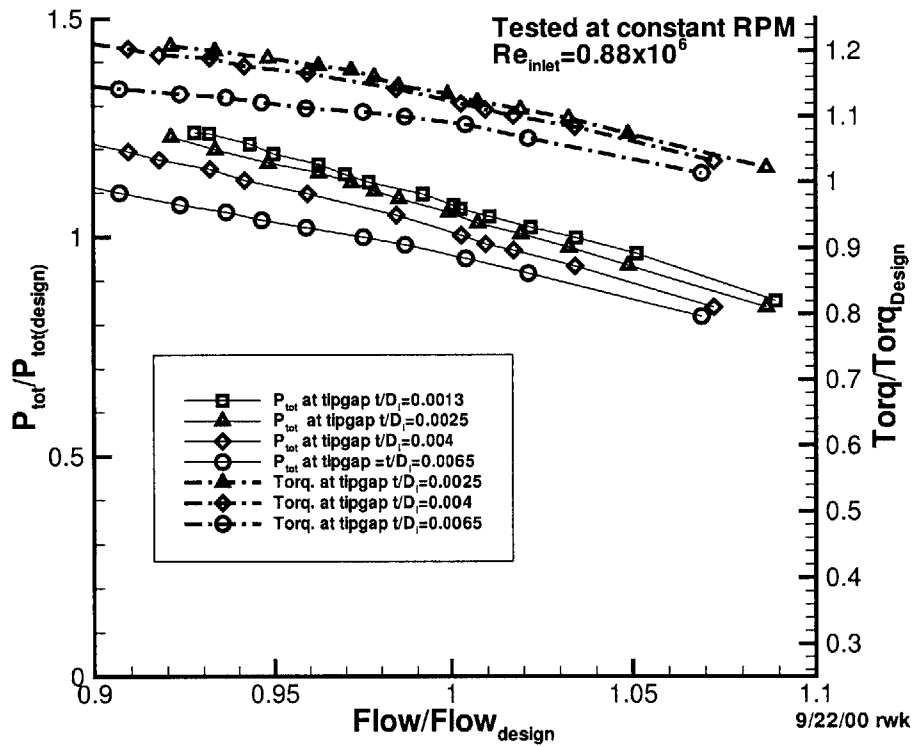
Figure 3-2: Pump Curves at Various Rotor Tip Clearances

It is general knowledge to both designers of turbomachinery and of ducted propellers that the effect of tip clearance is significant in many cases, causing a global reduction in the overall load of the bladerow. However, in the case of waterjets there
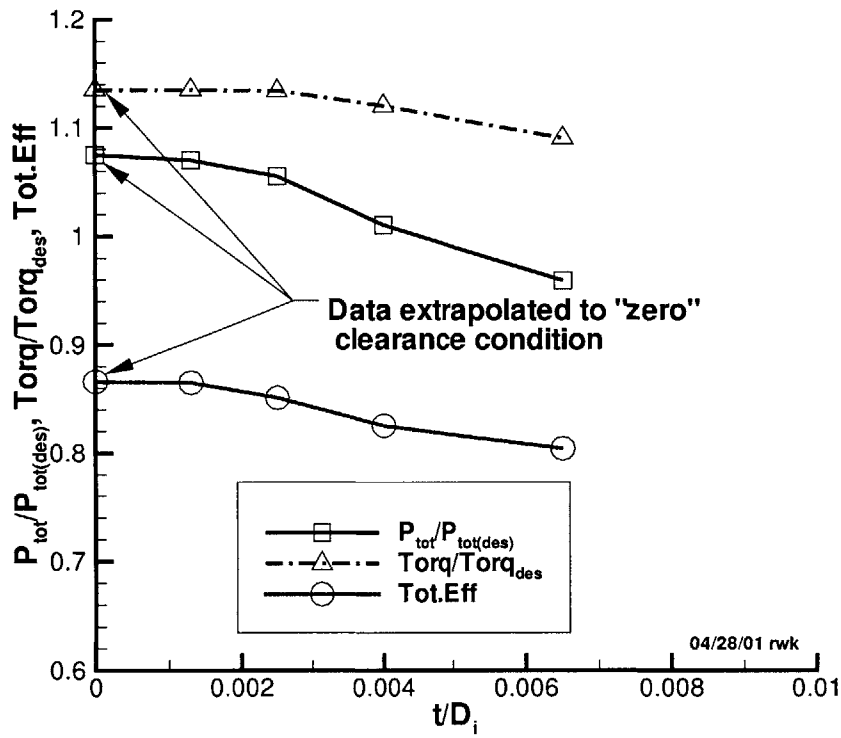
Figure 3-3: Effect of Tip Clearance on Waterjet Performance at the Design Flow Condition

is little quantitative data published on the effects of tip clearance on performance for a mixed flow waterjet rotor of low aspect ratio.

3.1.3 Mean Inflow Velocity and Stagnation Pressure Profiles

Figure 3-4 shows the non-dimensional axial inflow velocity and stagnation pressure profiles measured at the inlet measurement plane of the waterjet pumpset. The condition shown is for the rotor at the test speed and design flowrate. The reference for the stagnation pressure measurements was the inlet plane wall static pressure ports. This shows that the inflow was uniform across most of the duct but a measureable duct wall boundary layer existed near the duct. This type boundary layer is not unexpected in the case of a real waterjet housing due to the nature of the inlet elbow hydrodynamics.
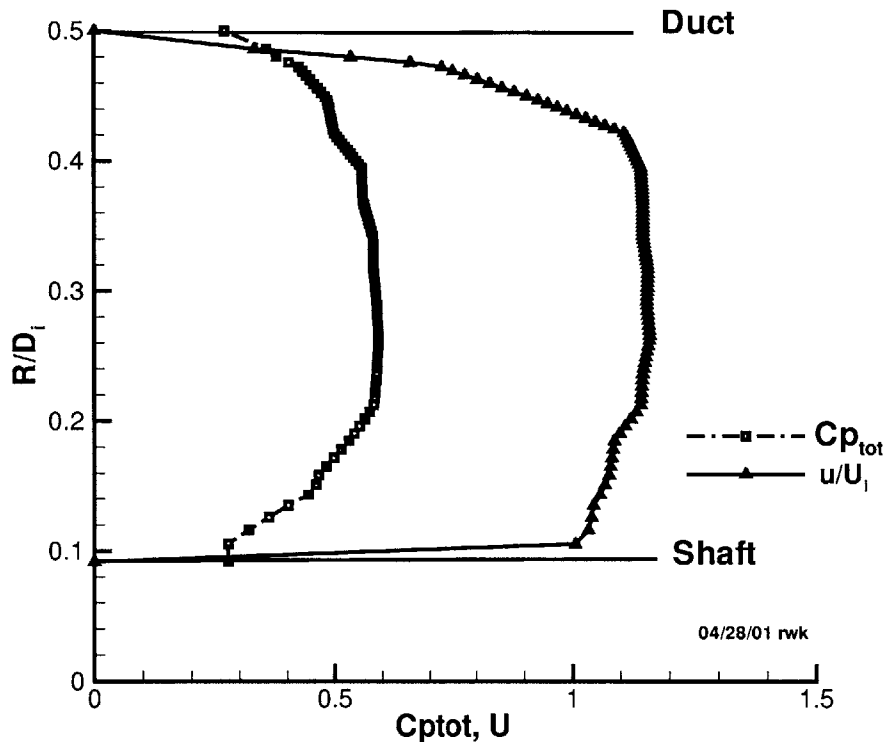
Figure 3-4: Inflow Velocity and Stagnation Pressure Profiles

3.1.4 Exit Plane Mean Velocity and Stagnation Pressure Profiles

Figure 3-5 shows the axial and tangential velocity profiles as well as the stagnation pressure profiles as measured at the exit plane of the waterjet pumpset at the model test speed with a nominal tip clearance $t/Di = 0.0025$. Due to the non-axisymmetric nature of the stator blades, the curves in figure 3-5 represent the average of eight stator angular positions (see Chap 2 Figure 2-22).

The results show that the stator does fairly well at cancelling the swirl in the outer portion of the duct, but overswirls the flow near the hub resulting in a hub vortex. Ideally, the pumpset would be designed to perfectly cancel the swirl everywhere in the exit flow. The stagnation pressure profiles also show a swirl induced pressure drop near the hub due to the presence of the hub vortex. The axial velocity distributions show a relatively large wake coming off the hub tail cone indicating the possibility of

separation on the tail cone.

Figure 3-6 shows the exit plane velocities and pressures at the design flow condition but with tip clearance set to a moderately high value ($t/D_i = 0.005$) This data corresponds to the condition where detailed loss and energy balance calculations were computed (derived later in this paper).
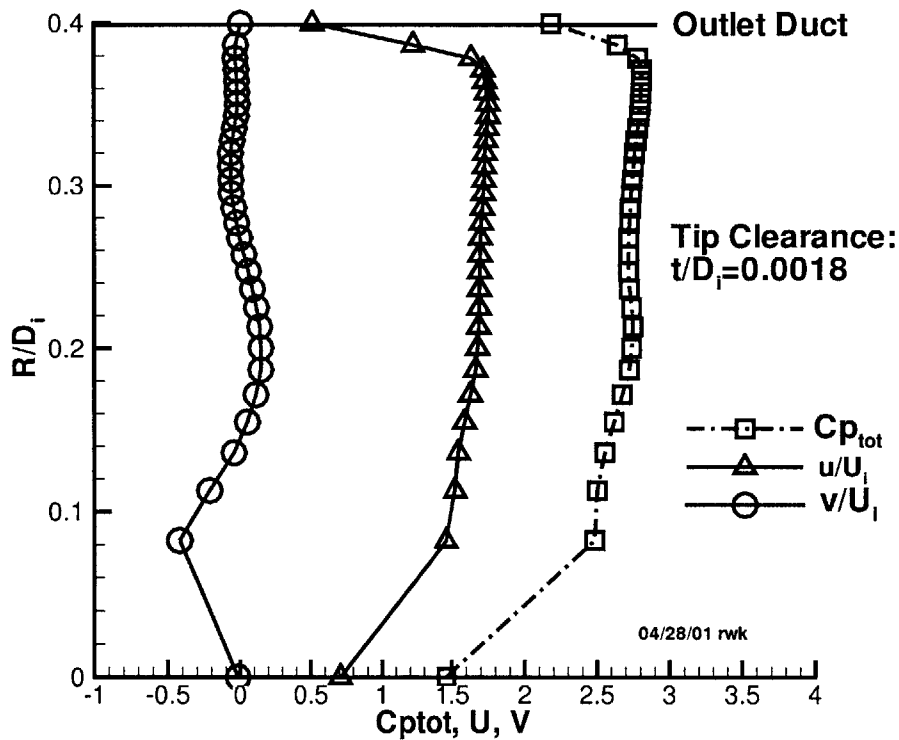
Figure 3-5: Exit Velocity and Pressure Profiles at $t/D_i = 0.0018$

3.1.5 Midstage Plane (Rotor exit) Mean Velocity and Stagnation Pressure Profiles

Figure 3-7, when first collected, gave the most suprising results up to that point in the testing. Prior to this, data performance curves, tip clearence effects, inlet and exit profile data all gave expected results. Given the fact that the operating head agreed well with the intended design gave confidence that the design procedures implemented
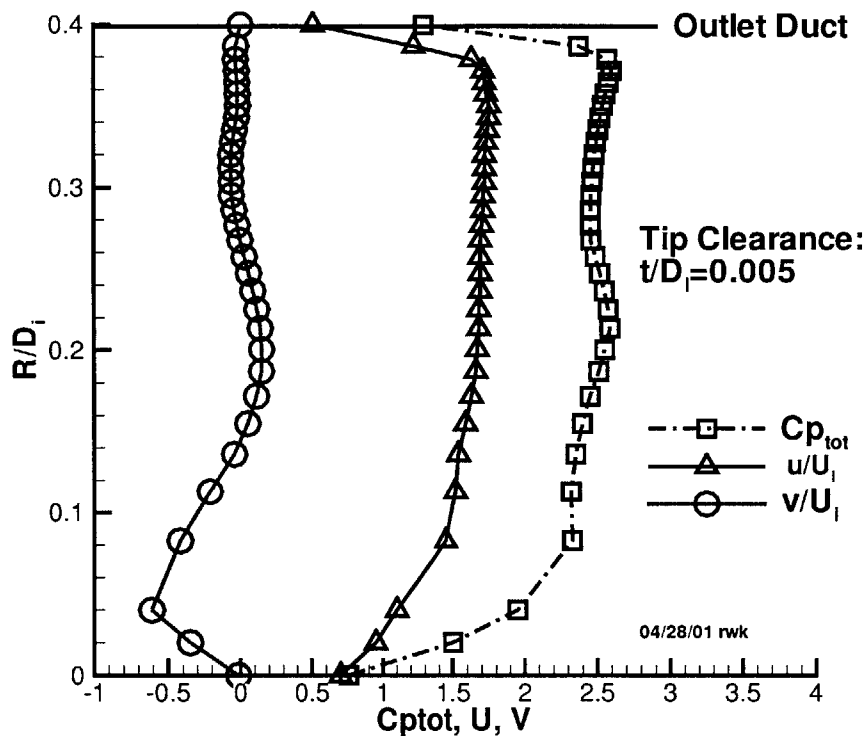
Figure 3-6: Exit Velocity and Pressure Profiles at $t/D_i = 0.005$

for this waterjet design were well suited to the design of waterjets. However, the search for answers to the underprediction of torque by the numerical model led to more detailed measurements on the rotor.

The data of Figure 3-7 shows the mean tangential and axial velocity profiles between the rotor and stator taken at the design flowrate and the tip clearance set at a moderately high value of $t/D_i = 0.005$. The tangential data, in particular, showed a large increase in swirl near the tip region of the rotor. Also shown in Figure 3-7 is the original swirl distribution predicted by the early numerical design and analysis, showing a large discrepency in swirl near the rotor tip area. This discrepancy was puzzling, though it gave evidence of the source of the torque discrepancy, since it is expected that swirl directly corresponds to the torque of the bladerow. Figure 3-8 does in in fact show an increase in the measured total pressure near the tip due to
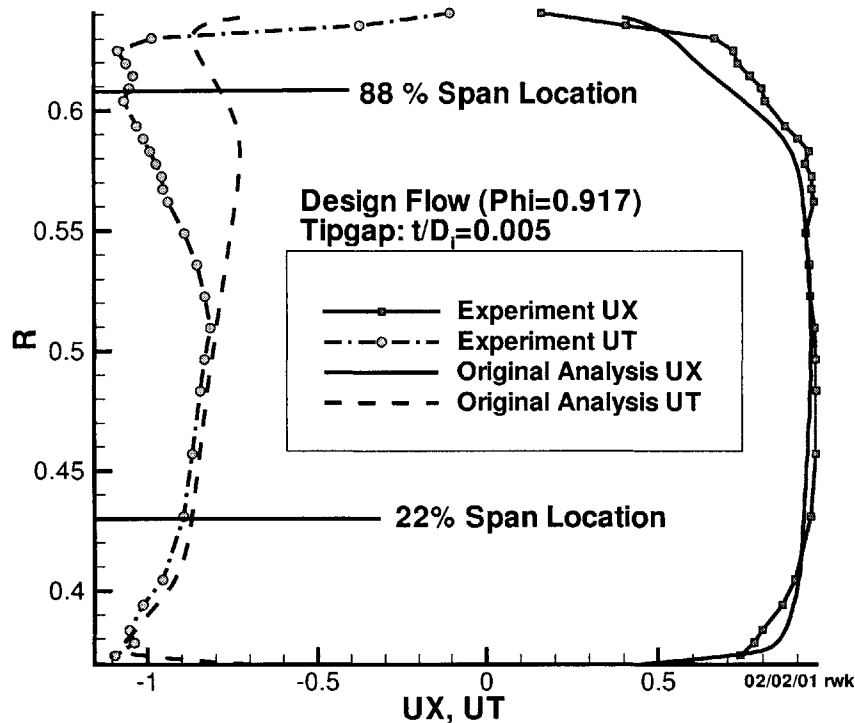
Figure 3-7: Mean Velocity Profiles Downstream of Rotor

the drag induced swirl when compared to the original predicted results.

Why was this large increase in swirl not showing up as increased pressure rise in the pump? Part of the answer lay in Figure 3-8, which shows a large drop in stagnation pressure near the rotor tip, and indicated high losses in this region relative to predictions. So the work done by the extra swirl is being negated by the high loss of pressure in this region.

3.1.6 Phase-Averaged Velocity Measurements at the Rotor Exit

To further investigate the nature of the high losses and high swirl found near the tip of the rotor, phase-averaged velocity measurements were conducted at the rotor exit (in the midstage measurement plane) at the design flow and $t/D_i = 0.005$. Data were taken at many radii across the duct but the essence of the results of these
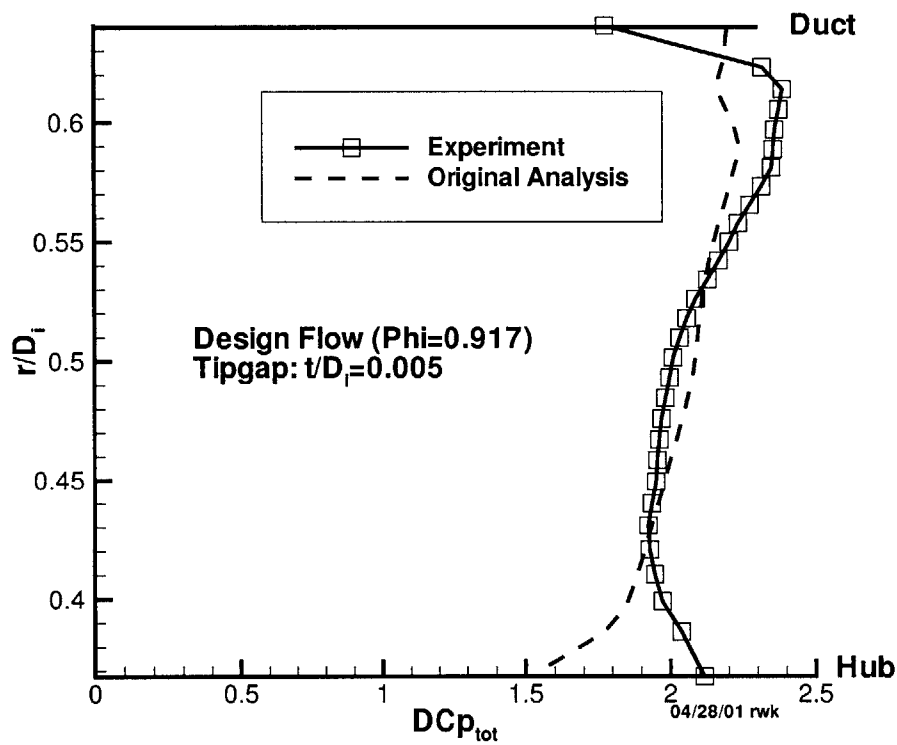
Figure 3-8: Stagnation Pressure Profile Downstream of Rotor

measurements is shown in Figure 3-9, which show phase-averaged axial and tangential velocity measurements at two radial positions. The first radii, corresponding to a radius $r/D_i = 0.43$ is at the inner radii region of the rotor exit annulus where the mean tangential velocity agrees with the original prediction (see Figure 3-7). The rotor blade wake dents are narrow and look like the 2-D section wakes expected from typical blade sections. The numerical model, in fact, used 2-D cascade thoery to estimate the blade drags used in the model, so we could expect good agreement in this region.

The second measurement position shown in Figure 3-9 was located near the rotor tip $(r/D_i = 0.608)$ This point was located in the region where major discrepancy in mean swirl between prediction and experiment occurred. The data at this point shows very large rotor blade wake dents indicative of a high loss region , and indicate
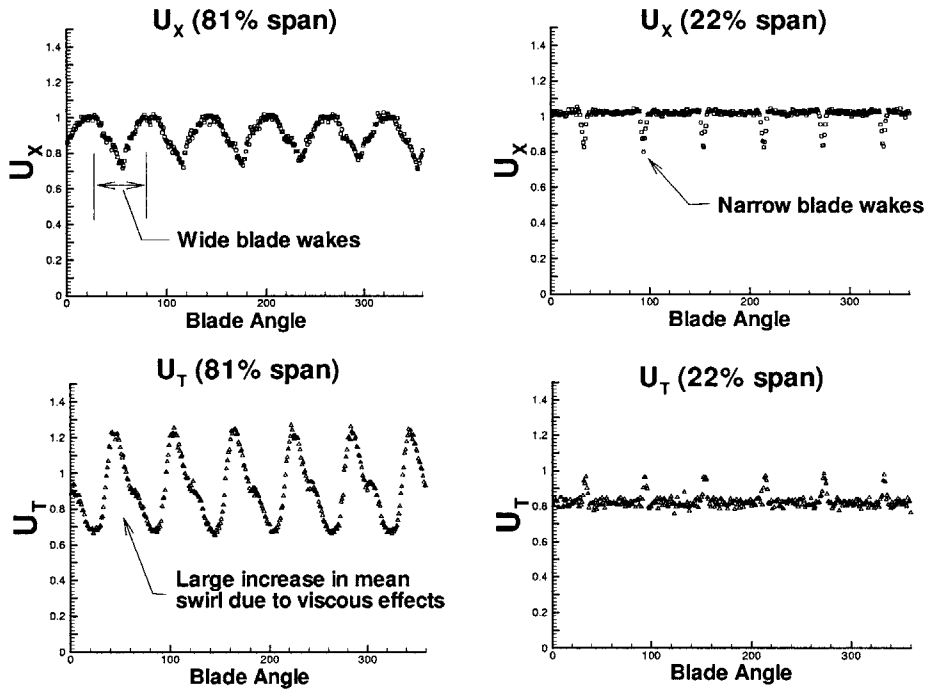
Figure 3-9: Phase Averaged Velocity Profiles Downstream of Rotor

flows of a complex nature near the blade tip. The tangential velocity data at this point also shows evidence of a secondary flow vortex in the mid-passage area (noting the small deviation in the swirl velocity in the wake dents of Figure 3-9). It will be shown later that this corresponds to the leakage vortex forming from the tip leakage flow. The phase averaged data at this location points to the increasing importance of the tip leakage/duct tip juction flow losses in the performance and efficiency of this waterjet pumpset.

3.1.7   Rotor Exit Velocity Profiles vs. Tip Clearance

Mean velocity profiles at the exit of the rotor were measured as a function of tip clearance and the results are shown in Figure 3-10. The effect of tip clearance on the pump loading is most apparent in the swirl distribution, which shows a global reduction in the swirl due to increased tip cleareance. The effect of tip clearance on loading is not just a local effect.

The more suprising results shown in Figure 3-10 is the fact that the drag induced

swirl near the tip of the rotor is very insensitive to the tip clearance. One would expect the swirl in this region to follow the same reduction in magnitude that the rest of the blade shows. The fact that the tip clearance has little impact on this drag induced swirl in this region is puzzling, though it was shown in figure 3-3 that the impact of tip gap on efficiency was significant. It appears, in this case, that the junction flow velocity field is driven by the nature of the junction itself, but the losses manifested in this region are directly related to the tip clearance.
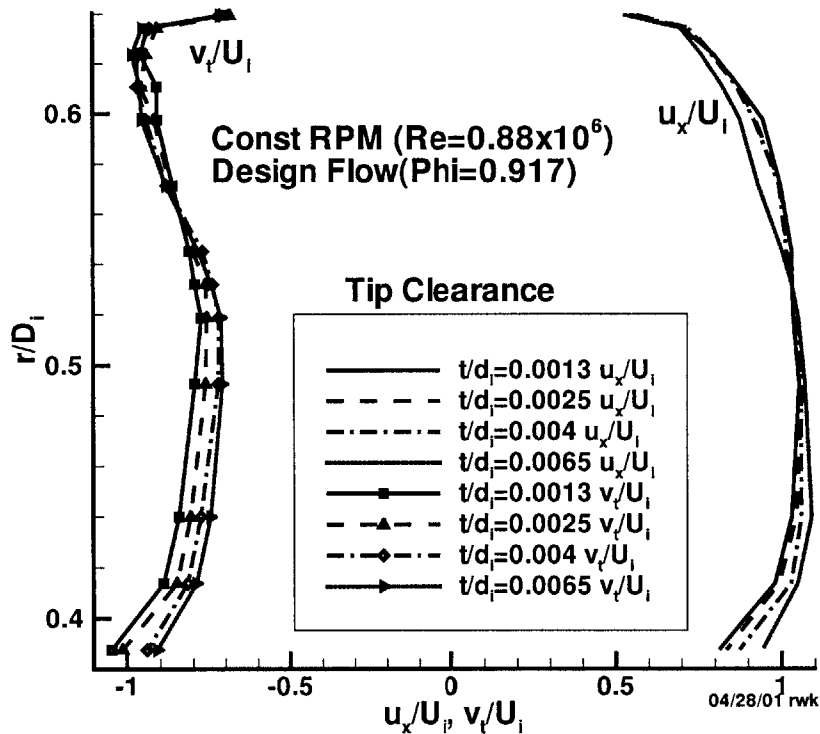
Figure 3-10: Mean Rotor Exit Velocity Profiles at Various Rotor Tip Clearances

3.1.8 Tip Leakage Vortex Flow Visualization

The tip leakage vortex at the design flow condition and $t/D_i = 0.005$ was observed by lowering the tunnel pressure until the tip leakage vortex cavitated. Figure 3-11 shows a cavitating leakage vortex crossing the passage between blades. A few points

can be noted from this photograph. First, the trajectory of the vortex indicated high velocities in the tip clearance region. Second, the vortex seems to be fed by additional (smaller) vortices that combine with the vortex and build its strength. This observation makes it easy to conceptualize an explicit vortex lattice representation of the leakage vortex. Since the shed vorticity combines into one vortex this would make modelling and aligning such a vortex model easier to implement. Pictures of cavitating leakage vortices has been documented before and [45] shows good examples of similar pictures for a stator/ rotor pumpset.
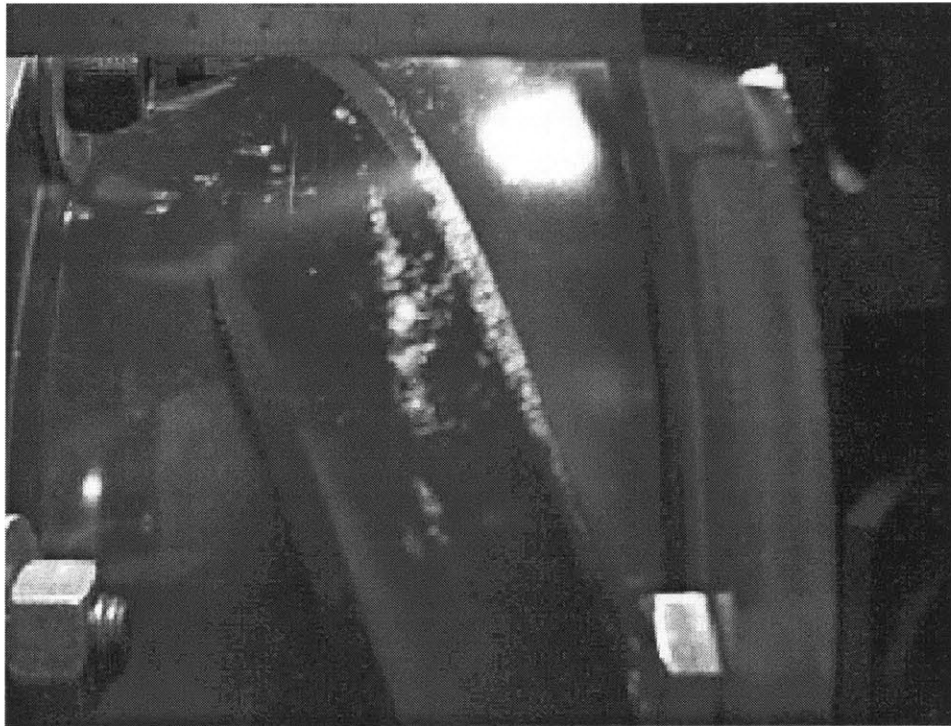
Figure 3-11: Picture of Tip Leakage Vortex

3.1.9   Rotor and Stator Loss Profiles

The data collected thus far on the waterjet rotor indicates that high losses may be occuring near the rotor tip in the area of the tip leakage. To quantify these losses, and where they occur radially in the blade row, an analysis was conducted to extract this information from the profile data collected. Since the stagnation pressure profiles are direct measurement of the fluid energy for an incompressible flow, this

information coupled with the axial and tangential profiles allowed the computatation of the energy flux through the measurement planes, provided calculations were carried out on mean streamtubes. Also, through careful energy analysis in the relative (or rotating) coordinate system, the energy loss profiles were also determined from the profile data.

In order to carry out the calculation of pressure, energy and energy flux the determination of the radial location of a circumferential mean streamtube was necessary, since it is desired to track these changes along streamtubes. The basic question becomes: what radius at a downstream measurement plane corresponds to some radius at the inlet (or reference) plane such they both represent flow along the same mean streamline. The typical solution to this problem is easily obtained by computing the stream function, Ψ at each plane, which is defined in equation 3.1. The stream function represents the cumulative mass flux from the inner hub radii to the radius of interest. Because mass flux is conserved, values of equal stream function at two different axial locations represent the same mean streamline and once the stream function is picked the radius of the streamline at each location can be computed. It should be noted that the mean streamtube does not correspond exactly to any local streamline since the real flow is non-axisymmetric, but represents only the axisymmetric portion (or circumferential mean) of the streamlines at a given radius.

$$\Psi = \frac{\int_{r_i}^{r} 2\pi U_x r\, dr}{\dot{Q}} \qquad (3.1)$$

Once the radii of a particular mean streamline at two duct axial locations was found then the change in stagnation pressure was determined from the Kiel probe profile data at the proper radii at the two stations. By converting this stagnation pressure to the stagnation pressure in the relative (rotating) coordinate system using relation 3.3 , the energy loss, $P_{t\Omega}$ was determined along this streamline. The loss coefficent $\bar{\omega}$ was then computed using equation 3.4.

If the stagnation pressure change along a differential streamtube is multiplied by the volume flux along that streamtube then a relation for the energy flux can be computed by integrating this product across the entire duct as stated in equation

69

3.5. By applying this energy relation in the relative coordinate system a relation for the energy loss can be computed using equation 3.7 or non-dimensionally 3.9. The integrand of equation 3.9 was then defined as the energy loss flux coefficient and represents the distribution of energy losses across the duct. Depicting the losses in terms of the energy flux loss coefficient gives an accurate picture of the radial distribution of losses for which is not depicted in the typical pressure loss coefficient. For example, if the pressure loss is large in an area of low flow (like a wall boundary layer) then the net effect of the losses in this region would be small. Obviously it would be important for a designer to understand what regions of the bladerow have high losses so that those areas may be focussed on to improve performance.

The stagnation pressure in the relative reference frame at a point is:

$$P_{t\Omega} = P_t - \rho V_t \omega r \tag{3.2}$$

The change in relative stagnation pressure along a mean streamline is then:

$$\Delta P_{t\Omega} = \Delta P_t - \rho \omega \Delta(r V_t) \tag{3.3}$$

The pressure loss coefficient along a streamtube is defined as :

$$\varpi = \frac{\Delta P_{t\Omega}}{\rho U_i^2} \tag{3.4}$$

By integrating the product of the change in stagnation pressure and the volume flux on a differential streamtube the energy flux passing through this section of duct is:

$$\Delta E = \int_{r_i}^{r_o} 2\pi \Delta P_t V_x r \, dr \tag{3.5}$$

or non-dimensionally:

$$\Delta \Xi = \frac{\Delta E}{\rho U_i^3 D_i^2} \tag{3.6}$$

and the power loss passing through the duct is similarly:

$$\Delta E_{loss} = \int_{r_i}^{r_o} 2\Pi \Delta P_{t\Omega} V_x r \, dr \tag{3.7}$$

70

or non-dimensionally:

$$\Delta\Xi_{loss} = \frac{\Delta E_{loss}}{\rho U_i^{3} D_i^2} \qquad (3.8)$$

The energy flux coefficient is then defined as:

$$\xi(r) = \frac{\Delta P_{t\Omega} V_x 2\Pi r}{\rho U_i^3 D_i} \qquad (3.9)$$

The concept of loss analysis along streamlines is common in the turbomachinery literature and Vavra [37], Denton [6] and Lyman [26] all provide information on these techniques. One interesting outcome of the loss coefficient of equation 3.4 is that it is easily converted to a streamtube efficiency by dividing by the inlet stagnation pressure in the relative coordinate system and subtracting it from one as in equation 3.10. This pressure is sometimes called the ideal pressure, since if it were constant throughout the bladerow then there would be no loss.

$$\eta_{sl} = 1 - \frac{\Delta P_{t\Omega}}{P_{t\Omega inlet}} \qquad (3.10)$$

The computed pressure and energy loss flux as a function of streamfunction are shown in Figure 3-12 for both the rotor and stator. The loss profiles for the rotor show very large losses in the outer radii of the duct, which constitutes almost all the rotor losses. At the inner radii of the duct the losses are near zero (the fact that they dip slightly below zero is an artifact of the measurement resolution as well as the possibility of losses "leaking" to the outer radii through the blade wake and boundary layer migration). Any effort to reduce the rotor losses should then be directed toward the junction flow/ tip clearance region of the rotor. The stator loss profiles are also depicted in Figure 3-12. The losses for the stator also show large losses in the outer duct region. However, the mechanism for the stator losses is likely quite different than that for the rotor. First of all, though the stator has duct junction flows, there are no tip clearance losses since the tip clearance is zero. If one looks at the mean velocity profiles coming off the rotor and into the stator (as in Figure 3-7) it apparent that the incidence angle of the flow relative to the stator is far from its intended design. Thus

much of the loss in the stator may be attributed to the fact that the stator blades are not properly aligned with the highly disturbed flow coming off the rotor. This is somewhat good news, since by re-aligning the stators much of the stator losses may be reduced substantially.
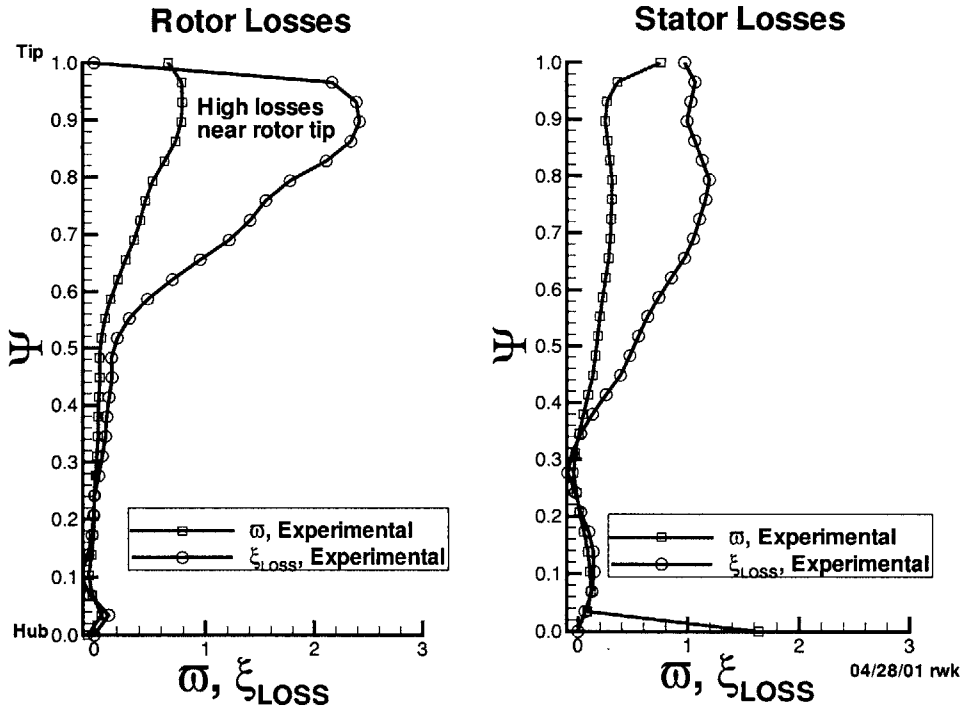
Figure 3-12: Loss Profiles

3.1.10 Pumpset Energy Balance

By computing the total energy flux accross the rotor and stator and comparing this power to the input shaft power of the rotor, a complete energy balance of the pumpset was performed. The non-dimensional shaft power can be defined as in equation 3.11, which is consistant with the definitions of the non-dimensional energy flux and energy loss flux as defined by equations 3.6 and 3.9 respectively. By adding the energy flux gain measured in the fluid to the computed lost energy flux, this should balance the input shaft power if all energy is properly taken into account. Table 3.1 shows the result of the energy balance applied to the waterjet pumpset at the design flow

	Rotor	Stator	Pumpset
Ξ	1.58	-0.14	1.46
Ξ_{loss}	0.19	0.14	0.33
Ξ_{total}	1.77	0.0	1.79
Ξ_{shaft}	1.79	-	1.79

Table 3.1: Waterjet Pumpset Energy Balance

condition with $t/D_i = 0.005$, representing the case where the loss profiles of Figure 3-12 were conducted. The results of Table 3.1 show that energy balance is achieved to within the measurement error. This confirms that all energy is accounted in the analysis, lending an independent check on the energy and loss computations presented thus far in this work.

$$\Xi_{shaft} = \frac{T_{shaft} \times \Omega}{\rho U_i{}^3 D_i^2} \tag{3.11}$$

There is some question as to the extra loss due to whether the duct shear is properly accounted in the energy balance. Since the duct is stationary and the rotor is rotating, there is a shear that develops between the rotor and duct, which consequently affects the rotor torque. If the shear dissapates as heat into the fluid then it will not influence the stagnation pressure and consequently would not be measured by the Kiel probe. Generally the duct shear effects are less than 2% of the shaft power and thus is within the shaft power measurement error bounds.

3.1.11 Extraction of Estimated Drag Coefficients from Loss Profile Measurements

The numerical models employed in this research represented blade viscous losses in terms of blade secton drag coefficients input by the user. It was then desired to extract estimated section drag coefficients from the measured loss profiles data in order to input these "measured" drag coefficients back into the model. In this way it was hoped that by introducing correct losses into the model so that the model would more accurately predict the pumpset flow fields and overall pump performance

73

characteristics. Specifically, by introducing the corrected losses, better prediction of the rotor exit swirl profiles (including the loss induced swirl effects) could be obtained. This is especially important for the design of the downstream blade row (i.e. the stator) since it sees the incoming flow off the rotor.

To estimate the sectional drag coefficients based upon the loss profile measurements one can relate the "Drag" losses to the energy loss at a given radii using equation 3.12. Equation 3.13 is the typical definition of sectional drag coefficient (and the one used in the numerical models). Combining equation 3.12 and 3.13 gives equation 3.14.

On a given streamtube:

Energy Loss:

$$F_{drag}U = 2\pi r \Delta P_{t\Omega} U \qquad (3.12)$$

Defining the drag coefficient:

$$C_D = \frac{F_{drag}}{1/2\rho U^2 C} \qquad (3.13)$$

Combining 3.12 and 3.13 gives

$$C_D = \frac{4\pi r \Delta P_{t\Omega}}{\rho U^2 C} \qquad (3.14)$$

Thus in order to estimate the sectional drag coefficient estimations of velocity U and the effective chordlength C are needed. The velocity was estimated as the mean relative velocity between the inlet and outlet measurement planes as in equation 3.15. The chordlength was estimated using a geometrical approximation of the bladechord using relation 3.16. Granted these estimates of velocity and chordlength were crude, but the ultimate goal was merely to show that by using the actual blade losses that the numerical models would give more accurate predictions.

74

Estimated mean streamtube velocity was estimated as follows:

$$U = [0.5(U_{xin}^2 + U_{xout}^2) + 0.5((\omega r - U_{\theta out})^2 + (\omega r - U_{\theta in})^2)]^{0.5} \qquad (3.15)$$

Sectional chordlength was approximated using the following geometric relation:

$$C = C_{root} + (r - R_{hub})/(R_{tip} - R_{hub})(C_{tip} - C_{root}) \qquad (3.16)$$

Where C_{root} is the blade root chord and C_{tip} is the blade tip chord

The estimated drag coefficients for the rotor using relations 3.14 3.15 and 3.16 is shown in Figure 3-13. Also shown in this plot are the original estimates of the section drag coefficients used in the design process. This plot shows that the original estimates of losses were substantially underestimated. Given this information, the under prediction of rotor power is not difficult to understand.

Discussions of the numerical analysis results using the drag coefficients estimated from the experiment are discussed later.
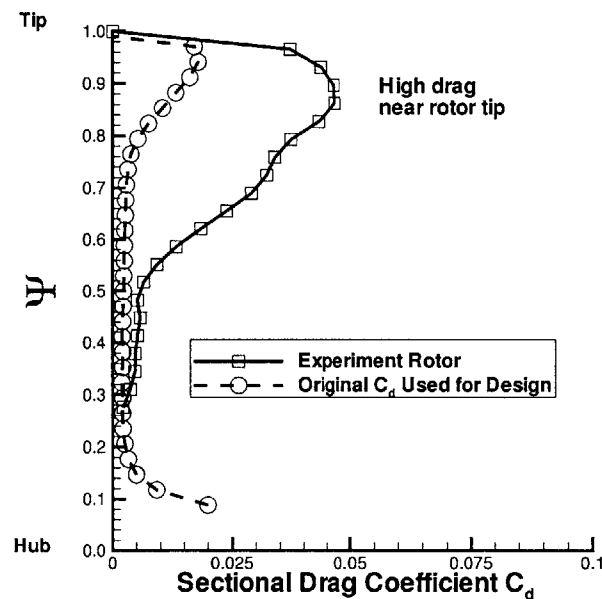
Figure 3-13: Rotor Sectional Drag Profiles

Chapter 4

Numerical Modelling Improvements

4.1 Background on the Numerical Modelling Methods

The coupled Lifting Surface/Throughflow solver method described in prior sections was the numerical model employed both in the design of the waterjet pumpset described in this work and the subsequent analysis of the waterjet. The Lifting Surface technique employed a vortex lattice method applied to the blade row's mean camber surfaces and utilized coincident source lines to represent thickness. Two axisymmetric throughflow solvers were employed, the first being a Reynolds Averaged Navier Stokes (RANS) solver, and the second being a streamline based Euler solver. The Euler solver was originally coupled by Renick [31] and later improvements were implemented by Hanson [10]. The great advantage of the Euler solver as compared to the RANS solver were both its ease of use by the user and the computational speed which was more than an order of magnitude lower than that of the RANS solver. The main disadvantage of this particular Euler solver was that is was limited to axisymmetric flows and could not be easily adapted to a non-axisymmtric solution. Since the design and analysis codes implemented in the coupling procedure were limited to axisymmetric inflow this was not a real limitation. However, since the 3-D lifting surface code is easily adapted to non-axisymmetric flows, coupling with a 3-D RANS solver would be necessary. In fact a coupled unsteady Lifting Surface/3-D RANS

technique was implemented by Warren [38] and more recently improved by Renick [32].

The Vortex Lattice lifting surface/RANS coupling method was first introduced by Kerwin et al [18] and later improved by Black [4]. The lifting surface code used in the model of Black [4] used images to model the effects of hubs and ducts on the blade rows and had no tipgap model implemented. The blade wakes were aligned with the circumferential mean flow rather than the local flow. Improvements to this model were implemented by McHugh [27] and included the addition of disctretized hub and duct models and a tip gap model based on the models developed by Kerwin [16] and Van Houten [11]. Full wake alignment models had not yet been added to the current model but alignment algorithms created by Greeley [9] had been implemented in similar Lifting Surface models. Work done by Ramsey [30] implemented a wake alignment method more generalized than Greeley's model. The work reported in this research added to the current lifting surface models a wake alignment model which built upon the work of Ramsey [30].

The loss modelling capability of the numerical models consisted of determining drag forces on the blades and passing those to the RANS solver as circumferential mean body forces. Prior to this research, no loss coupling had been implemented into the Streamline Euler solver, so this effort implemented an entropy based coupling which the throughflow solver was already designed to handle as input.

4.2 Wake Alignment

Typically, in the case of free tip propellers, trailing wake alignment for lifting surface calculation has been complicated by the tendency for wake edges to roll up tightly. This rollup causes numerical instabilities because wake field points (used for setting wake trajectories) can move physically close to the wake singularity elements. To avoid singularity problems associated with the rollup of the vortex sheet early wake alignment methods had to constrain the sheet in some way to avoid rollup (as done by Greeley [9]), for example, by constraining the vortex wake outer streamtube radius evolution.

Some researchers have created models to closely track the wake trajectory and rollup by finely discretizing the wake and taking great care to avoid singularity problems (as done by Pyo [29]). Though refined detail of the rolled up wake sheet may be useful to model tip vortex cavitation, such resolution is generally not needed to adequately capture the wake's effect on the blade forces. In addition, the fine discretization required to adequately rollup the wake can become quite computationally intensive.

Ramsey [30] implemented a wake alignment procedure based on a desingularized vortex model that eliminated the numerical issues associated with the singularities. Ramsey's method allowed the computation of the wake vortex velocity on the elements themselves, which also eliminated velocity interpolation problems associated with control points located between vortex elements. The desingularization parameter mimicked the behavior of a real viscous vortex with a viscous core region, though the model was not based on a physical representation of the flow. The desingularization parameter turned out to be a vortex core radius that was set to give stable results of the wake alignment algorithm and was not allowed to change as the wake trailer evolved.

A wake alignment procedure similar to Ramsey's was implemented into the current lifting surface model with a few key differences. The vortex model utilized the "Oseen Vortex profile" which is the steady solution of a 2-D vortex (infinite line vortex) in a viscous fluid. From this model an explicit relationship was formulated for the growth of the vortex core as the wake trailer convected downstream.

4.2.1 Desingularized Vortex Algorthms

Figure 4-1 shows the tangential velocity profile about an Oseen vortex at various vortex decay times. The Oseen vortex is essentially the profile that an infinite 2D line vortex would assume in a viscous fluid and is the solution to the vorticity equation under the assumption of a 2D axisymmetric steady flow. The "potential" starting vortex profile follows the relation of equation 4.1, and has infinite tangential velocity at zero radius. The Oseen vortex profile follows the relation of equation 4.2 which

looks just like the potential vortex formula 4.1 with a viscous decay term depending on fluid kinematic viscosity ν and the decay time τ. A derivation of the Oseen vortex can be found in White [39] .
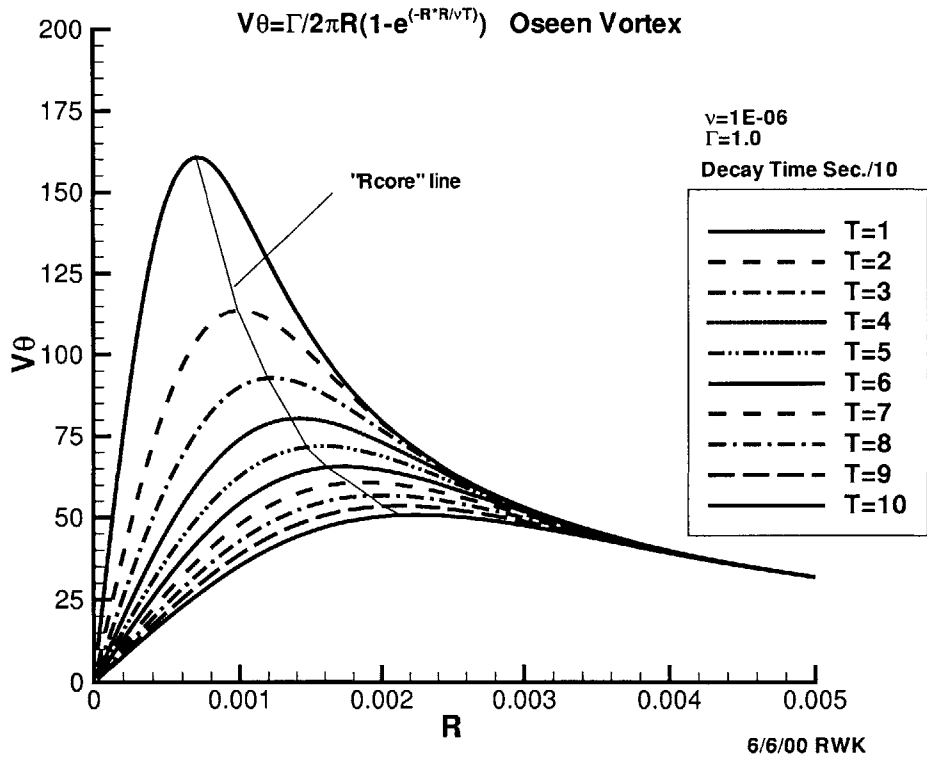
Figure 4-1: Velocity Profile of an Oseen Vortex

The induced velocity of a 2-D infinite potential vortex is given by:

$$V_\theta = \frac{\Gamma}{2\pi r} \tag{4.1}$$

The Oseen vortex profile is given by:

$$V_\theta = \frac{\Gamma}{2\pi r}\left(1 - e^{-\frac{R^2}{4\nu\tau}}\right) \tag{4.2}$$

It is important to note that the decay function is independent of the strength Γ of the vortex, which makes it possible (and in fact quite straightforward) to include

79

the vortex decay in the influence function calculation of the Lifting Surface solution procedure.

From the vortex decay model a decay time (and subsequently the core radius)can be computed from the convection history of the vortex trailer. The numerical effect of the growing core radius is to stabilize the wake trajectory. The definition of the vortex core radius is the point at which the maximum velocity occurs in the vortex velocity profile (see Figure 4-1). By taking the derivitive of the Oseen vortex equation 4.2 we can derive a relation relating the core radius (R_{core}) to the kinematic viscosity and decay time and the result is equation 4.3. The derivation of equation 4.3 is included in appendix A.

$$R_{core} = \sqrt{4\beta\nu\tau} \tag{4.3}$$

where $\beta = 1.255$

Equation 4.3 gives a simple relationship between the core radius of the vortex and the decay time of the vortex. In the model implemented, R_{core} is an input parameter to the vortex influence routines . Also, in the numerical model, the wake vortex trailers are grown according to the local velocity tangent to the vortex and a fixed timestep. This wake convection timestep was used as the R_{core} growth timestep of equation 4.3, since it represents the convection time of the wake trailer segment along the wake trailer. In this fashion the R_{core} growth model was implemented according to equation 4.4, which represents the cummulative growth in R_{core} along the wake trailer.

For the purposes of the model the careful derivation of the β term in equation 4.3 was overkill because the damping term ν will not be close to the pure fluid viscosity and for our purposes is simply a dissipation term. In a real wake the dissipation would be dominated by the turbulent dissipation or "eddy" viscosity which is generally much higher than the fluid viscosity in a wake region. Suffice it to say that this damping term ν will be set according to sensitivity studies on the wake alignment growth algorithm, but we should expect this term to be much higher than that of pure fluid viscosity. The real purpose of deriving the growth model according to some physical

insight on vortex decay is to find a form which is physically reasonable for such a core growth model.

$$R_{core} = \sqrt{4\beta\nu(t_{no} + \sum_{1}^{n}(\Delta t_n))} \qquad (4.4)$$

Defining the initial vortex core radius RC_0:

$$t_{no} = \frac{{RC_0}^2}{4\beta\nu} \qquad (4.5)$$

4.2.2 Wake Alignment Algorithm

Prior to this research, the Lifting Surface model utilized for these studies aligned the wake sheet coming off the blade with the circumferential mean flow. This neglected the local variation in the velocity field due to the presence of the blades and wakes. A wake alignment scheme based on the desingularized vortex scheme described earlier was implemented to align with the local flowfield. Figure 4-2 shows the effect of wake alignment with the circumferential mean flow vs. alignment with the local flow.

Using the desingularized vortex scheme mentioned in the previous section along with the R_{core} growth model of equation 4.4 along with an initial R_{core} set at the blade trailing edge, the wake was first grown along the circumferential mean flow. The induction velocities were then computed on the wake trailer nodes using the desingularized vortex routines. The wake was then regrown along the effective flowfield plus the computed wake node induction velocity and this process was repeated until the wake trajectory converged. Since the wake was regrown for each iteration, this method was labeled a "shooting method" and was found to converge satisfactorily after only 2-5 iterations.The core radius R_{core} was set at each node according to equation 4.4 where the timestep was the same timestep used to grow the wake. With the growth model implemented the stability and smoothness of the grown wake were greatly improved over keeping the core radius constant.

Another wake alignment method utilized was a "node velocity" method where

Wake alignment result on Propeller 4119

Flow

Blade
Rotation

Blade
Trailing
Edge

"Aligned " Wake Sheet
Aligned with local flow

Original Wake Sheet
Aligned with Circumferential Mean Flow

7/28/00 rwk
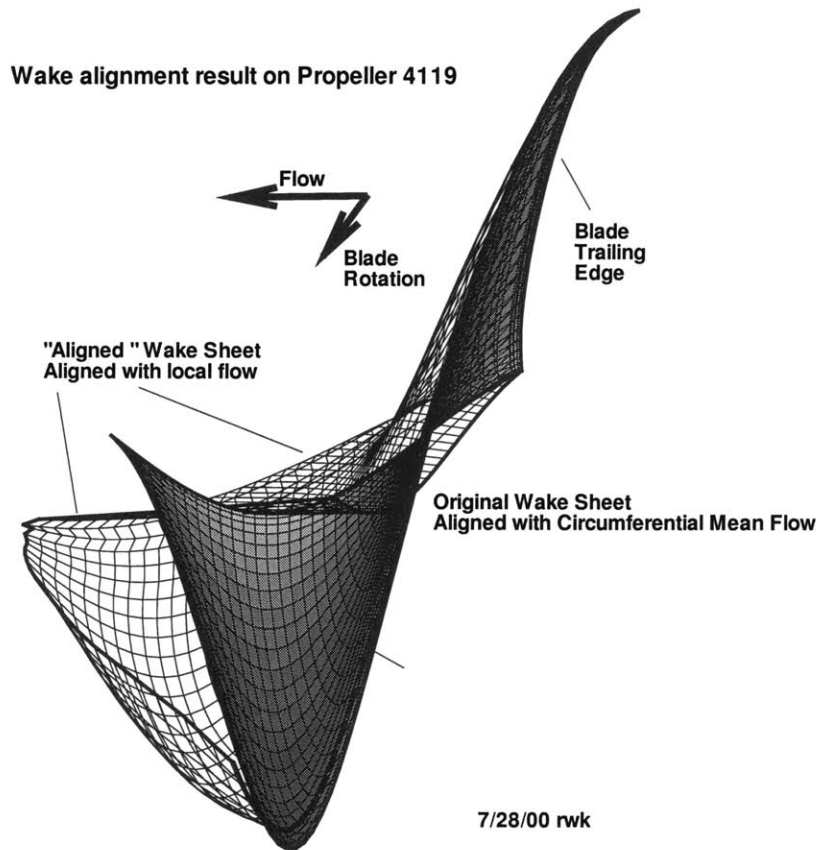
Figure 4-2: Aligned vs. Unaligned Blade Wake Sheet

each wake node was moved according to the computed cross velocity at each node, mimicking the motion of an actual vortex if perturbed by a crossflow. The node velocity method converged very slowly and was a function of the number of trailer nodes, as the wake trajectory had to ripple through the entire length of the trailer. However, the node velocity wake growth may be necessary to utilize in a time stepped unsteady code where an aligned wake is perturbed locally by a changing flowfield.

4.3 Losses

The losses manifested in the mixed flow waterjet can be categorized as follows:

- Blade drag loss

- Tip leakage loss

- Duct/hub wall boundary layer loss

- Blade induced drag loss

In seeking to model the losses though the pumpset one could lump the first three losses into a blade drag loss profile. In fact, in the Lifting Surface model, blade row losses are input as sectional drag coefficients. In this manner, by adjusting the radial distribution of drag coefficients, one can approximate the losses manifested by all the loss mechanisms depicted above (induced drag losses are already included in the lifting surface model).

4.3.1 Drag Induced Swirl

The results of Figure 3-7 show a large discrepancy between the swirl predicted by the model during the design process and the actual measured swirl. This discrepancy happens in the region of high losses near the tip of the rotor and consequently a region of high drag. The additional swirl velocity is made up in large part by the extra swirl induced into the flow by higher drag forces. Because the losses were introduced into the Lifting Surface model as forces (i.e. drag coefficients) applied to the blade surfaces the effects of drag forces on drag induced swirl was derived as part of this research. Besides giving us better understanding of this swirl effect, this derivation has practical use when adding the drag induced swirl effects in the Euler throughflow solver, since blade induced swirl is entered directly to the model.

Figure 4-3 depicts the blade surface forces as applied to a point or panel on the blade. This schematic shows both the "lift" force computed from the Kutta Joukowski law applied to the vortex lattice elements, and the drag force computed from the sectional drag coefficient. The drag force is applied opposing the surface streamline and one can see from Figure 4-3 that this force has a component in the swirl direction, which is generally in the same direction as the swirl force due to the lift. Hence, the drag forces should result in an increased swirl velocity as compared to the swirl induced if no drag were present.

To compute the swirl induced by blade forces one first starts with the momentum equation in the swirl direction. This equation in compact form is stated in equation
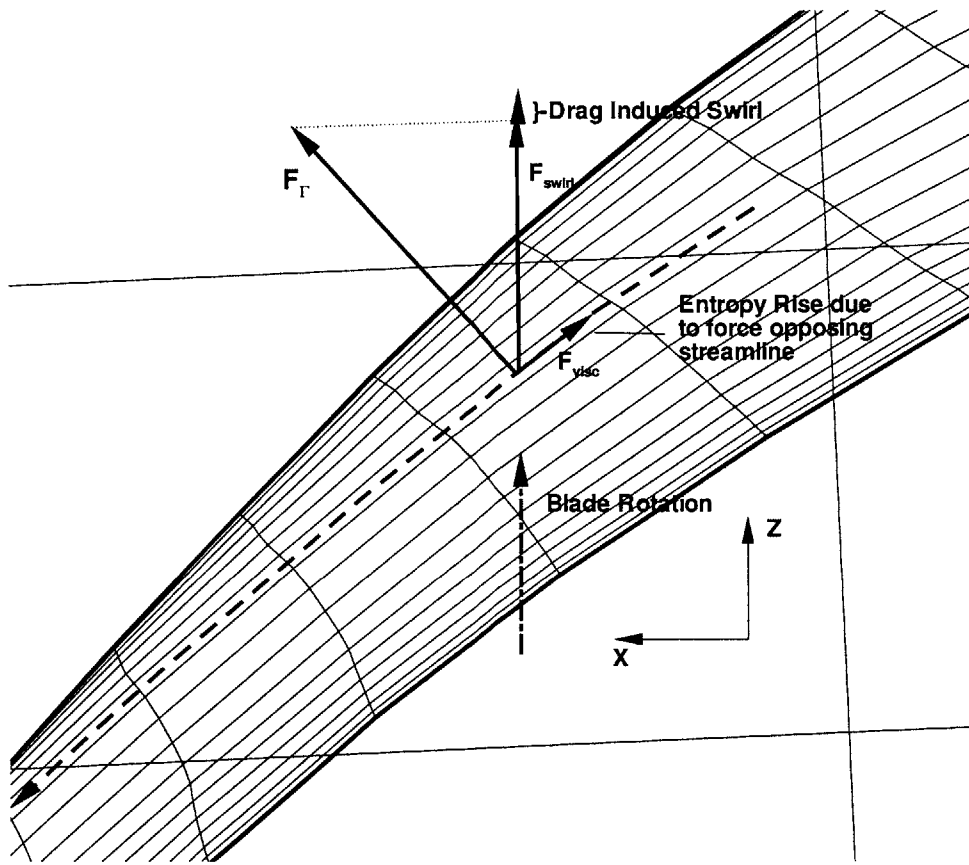
Figure 4-3: Blade surface force vector diagram

4.6 and derivation of this equation can be found in Lyman [26].

$$rF_\Theta = \rho\frac{D(rV_\Theta)}{Dt} \tag{4.6}$$

Where F_Θ is a volumetric body force and D/Dt is the substantial derivative

Equation 4.6 is essentially a differential form of the Euler turbine equation which is a fundamental concept to turbomachinery analysis. This equation is valid regardless of where the forces come from and thus is valid for loss forces as well as blade "lift" forces. With some manipulation (see appendix A) equation 4.6 can be written in the form of equation 4.7. Equation 4.7 shows that the change in swirl due to volumetric body forces is a function of the force itself, the surface velocity V_s and distance traveled along the streamline. In fact the term $\Delta s/V_s$ is merely the differential "time

of flight" along the streamline.

$$\frac{rF_\Theta}{\rho} = \frac{\partial(rV_\Theta)}{\partial t} + V_s\frac{\partial(rV_\Theta)}{\partial s} \tag{4.7}$$

Thus from equation 4.7 we can compute the swirl distribution along a streamlime induced by the tangential forces along that streamline. This will be used later to formulate a numerical scheme to convert forces into swirl necessary for coupling with the Euler throughflow solver.

4.3.2 Entropy rise due to losses

Entropy rise occurs from losses in the fluid due to the dissipative force opposing the local streamline (i.e viscous forces). These forces act to drop the pressure along the streamline and for an incompressible fluid this drop in pressure is equal to the drop in energy of the fluid. If we define the entropy as in equation 4.8 we see that the entropy rise is directly related to the streamline stagnation pressure drop due to the viscous forces. In the case of incompressible flow the entropy equation can be further reduced to equation 4.9, where P_{tinl} is the inlet reference stagnation pressure. To compute the the pressure drop along a streamline relation 4.10 was utilized since the pressure drop is simply the volumetric force times the distance traveled along the streamline and the total blade section loss is the integral of this relation.

Defining entropy in a form utilized by the Euler solver:

$$S \equiv ln\left[\frac{(h_t/h_{inl})^{(\gamma/(\gamma-1))}}{p_t/p_{tinl}}\right] \tag{4.8}$$

Where h is the fluid enthalpy.

Assuming viscous losses to be adiabatic we have $h_t =$ constant and equation 4.8 becomes:

$$S = -ln(p_t/p_{tinl}) + Constant \tag{4.9}$$

The expression for the pressure drop along the streamtube is :

$$dp_t = F_{sdrag} ds \qquad (4.10)$$

Where F_{sdrag} is the volumetric circumferential mean force opposing the streamline.

These relationships for entropy rise and pressure drop along the streamline will be used later to establish a differencing formula to be applied to the discrete viscous force distribution on the blade surface.

4.3.3 Tip Leakage Effects

It has been shown experimentally that the effects of the tip clearance and blade junction flow has a significant effect on the performance on the waterjet studied in this research. As far as modelling the effect of the tip clearance on pump performance three major effects were determined to be important. These effects were:

- The effect of the leakage flow on overall blade loading

- The effect of the losses of the leakage flow on pump head rise

- The effect of the leakage vortex on the flowfield and loading

The effect of leakage flow on overall blade loading has been well studied. For example Kerwin [16] and McHugh [27] both show examples of the overall blade loading reduction due to leakage flows on a ducted propeller. This effect was modelled purely as a potential flow effect and tip leakage losses were not accounted for in these models (other than the induced drag loss due to the circulation drop of the blade due to the tip leakage). The leakage model implemented by McHugh [27] was used in this research to model the drop in blade circulation due to the presence of a leakage flow. This model was based upon an orifice flow model applied to a gap panel created as an additional vortex lattice panel at the tip of the blade, between the rotor tip and the duct. The flow through this panel was not set to the typical blade condition of $\vec{V} \cdot n = 0$ but flow was allowed to pass through this panel in accordance with relation 4.11, where

V_g is the gap velocity normal to the panel, C_q is an empirical orifice coefficient and ΔP_g is the pressure jump across the gap (set by the gap panel strengths).

$$V_g = C_q\sqrt{2\Delta P_g/\rho} \tag{4.11}$$

Where V_g is the normal component of the velocity through the gap panel such that $V_g = V_s \cdot \hat{n}$

The fluid losses due to the gap can be modelled as body forces in the fluid, since it is clear that a fluid element in the gap has a net force across it due to the shear and pressure drop through the gap. The component of this body force opposing the flow streamline will result in the fluid energy loss. The component of gap body force in the tangential direction manifests itself as drag induced swirl. To model the forces due to the gap flow it can be assumed that all the fluid momentum component normal to the gap is lost (as is typical for an orifice flow). Knowing the drop in total pressure at this point and the direction of the tipflow streamline then the loss component of body force could be estimated. From the solution of the gap problem we also get another component of force from the gap singularity elements which is normal to the fluid streamline. This "Kutta-Joukowski" force has a tangential component which affects the swirl and an axial/radial component which affects the pump pressure rise. Figure 4-4 depicts the flow through a blade tipgap and shows the vector diagram of both the loss and lift forces as well as the local streamline.

The wonderful outcome of treating tipgap forces in this manner is that they are modelled in exactly the same way that the typical blade forces are represented. Specifically, the gap panel forces are computed exactly the same way that forces on the blade due to the vortex lattice are computed. Also the gap loss force is equivelant in nature to the section drag force (though the fluid physics of a gap flow is not the same mechanism as that of a section drag force). Thus in our final model of the losses in the gap, these forces and losses could be modelled simply as forces, just like the forces and losses of the rest of the propeller model. This means that gap losses could be entered as an equivalent drag force to account for the loss due to leakage. However, a single section drag coefficient model does not properly account for the distribution
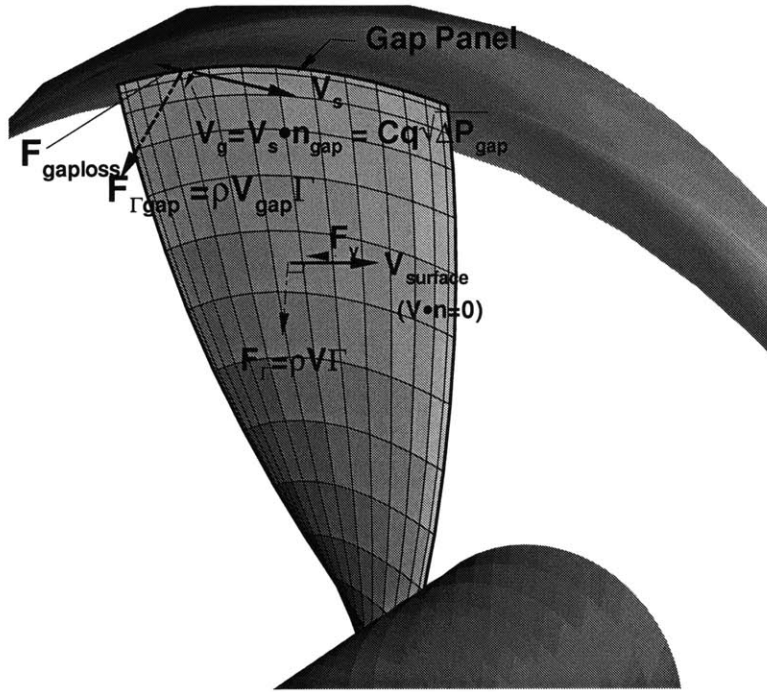
Figure 4-4: Schematic of Tipgap Flow Showing Forces and Flow Vectors

of losses, since the drag coefficient at each panel is assumed constant. The same problem arises for the blade drag model since the local "drag coefficient" is assumed constant on the section whereas in reality we know this varies as the boundary layer parameters change. An obvious shortcoming of the externally input drag coefficient is that it requires the engineer to estimate this before the calculation.

A more sophisticated approach, which could be implemented in the model without too great a difficulty, would be to compute the loss locally according to a gap loss model. Though such a tipgap loss model was not implemented as part of these modelling efforts such a model could take the form of equation 4.12. Equation 4.12 makes use of the gap model equation 4.11 and a gap power loss estimation expression $\dot{W} = \Delta P_{gap} A_{panel} V_s \cdot \hat{n} = F_{gaploss} V_s$.

$$F_{gaploss} = \frac{A_{panel} V_g^2}{Cq^2 V_s}(\rho/2) \qquad (4.12)$$

For the analysis and validation work completed as part of this research, the gap losses were simply lumped into the equivalant drag coefficients estimated from the

experiment. The prior arguments on the modelling of tipgap loss with forces serves to justify this approach as a reasonable way to treat such tipgap losses.

The prior lifting surface model did not pass tipgap forces into the throughflow solver, the argument being that since they were not part of the blade they should not be included in the coupling. However, it is contended in this research that these gap forces do exist in the real fluid and therefore should be passed to the throughflow solver in order to include their circumferential mean effect on the flowfield.

4.4 Loss Coupling into the Euler Solver vs. RANS solver

The prior work by Black [4] had successfully coupled the lifting surface solver with an axisymmetric RANS solver. Coupling the Lifting Surface solver to the RANS solver was achieved by computing blade circumferential mean forces at each blade control point and overlaying theses forces into the RANS grid by converting these point forces into volumetric body forces applied to each overlapped RANS cell. Because the forces passed from the Lifting Surface solver included blade drag forces, the method inherently included losses in the coupling procedure.

In the original coupling method the drag forces were applied at the trailing edge of the blade row. It was hypothesized at the time that the introduction of drag forces at the blade control points would introduce errors in the lifting surface solution of vortex strengths because the drag forces would induce changes to the velocity field used for the lifting surface calculation.

In the current research it was hypothesized that applying the drag forces at the control points in the coupling procedure was self-consistent with both the RANS solver solution and the Lifting Surface solver. It is certainly true that the drag forces change the velocity flow field in which the Lifting surface solver operates, but it is contended that this is the proper background flowfield for the calculation. The question that arises is whether the local nature of the drag forces is properly modelled by smearing these forces into circumferential average forces. However, the same is true of the blade potential lifting forces and the coupling of these circumferential mean forces has proved successful. Though not a proof, this analogy provides some

support that the inclusion of circumferential mean drag forces applied to the blade control points properly models the circumferential mean effects of these forces on the coupled solution.

One more direct problem of applying the drag forces at the trailing edge of the blade rows is that the effect of these forces on the throughflow solution is not perfectly accurate in the case of streamlines that change radius through the blade row. Since the tangential forces manifests into a torque that affects the local swirl, then the radius as well as the local velocity at which the force is applied affects the amount swirl intorduced into the flow. A simple proof based upon a tangential momentum equation arguement is carried out in appendix A, showing that the application of the total force to the trailing edge panel results in errors in the amount of swirl introduced. Of course, in the case of bladerows with little drag or change of streamline radius this error will likely be small. However, in the case of a mixed flow waterjet this effect is likely significant.

4.5 Coupling with an Axisymmetric Euler Solver Including Losses

Successful coupling of a streamline curvature based Euler Solver with the lifting surface blade model was implemented and validated by prior researchers, [31] [10]. However, in these coupling efforts the representation of blade row losses in the throughflow solver was neglected. These losses have an appreciable affect on the axisymmetric throughflow solution (and hence the final coupled solution) and the inclusion of these losses in the coupling procedure was desirable to improve the coupling methods accuracy.

The lifting surface model already had included a representation of blade losses through the input of blade section drag coefficients. The Euler solver also had the capability to model losses through the introduction of user specified entropy rise. Blade forces were introduced into the Euler solver through user input of blade induced swirl (rV_Θ). Prior coupling work had introduced the blade induced swirl but neglected both the drag induced swirl and the entropy rise due to losses. In this research the

90

proper coupling including the drag induced swirl and the entropy wise was added to the coupling procedure, and in this way proper modelling of blade row losses was achieved.

The prior Euler/Lifting Surface coupling method utilized the circumferential mean velocity computed for the blade lifting problem from the Lifting Surface model to compute rV_Θ directly. Since this is most of the blade force it was desired to simply add the rV_Θ contribution of the viscous drag to this precomputed blade swirl. To implement the introduction of drag induced swirl the momentum equation in the form of equation 4.7 was decomposed into a "viscous part" and a "lifting part". By expanding equation 4.7 in this way and collecting terms into a "lifting" part and a "drag" part the computation of the drag induced swirl could be done independently of the lifting force, such that the prior direct method of computing the lifting portion of rV_Θ could be utilized. The resulting expression for the change in swirl due to viscous force is shown in equation 4.13, which has been discretized along the streamline coordinate (s).

$$\Delta(rV_\Theta)_v = \frac{rF_{\Theta v}\Delta s}{\rho V_s} \tag{4.13}$$

Where $F_{\Theta v}$ is the circumferential mean volumetric drag force

To compute the net swirl at each node, equation 4.13 was differenced along the streamline according to equations 4.14 to 4.16.

Discretizing rV_Θ along the streamline:

$$\Delta(rV_{\Theta v})_n = (rV_{\Theta v})_n - (rV_{\Theta v})_{n-1} \tag{4.14}$$

Combining with equation 4.13 and solving for rV_Θ gives:

$$(rV_{\Theta v})_n = rV_{\Theta v})_{n-1} + \frac{rF_{\Theta n}\Delta s}{\rho V_{sn}} \tag{4.15}$$

Where the volumetric viscous force $F_{\Theta v}$ is computed from the discrete panel force $f_{\Theta v}$ as:

$$F_{\Theta v} = \frac{f_{\Theta v}}{2\pi r A_{panel}} \tag{4.16}$$

To compute the circumferential mean volumetric force at each node and its corresponding panel, expression 4.16 was utilized. The resulting drag induced swirl, computed according to the differencing equation 4.13, was then added to the swirl induced by lifting forces.

One shortcut taken in this method for the calculation of the drag induced swirl was that the streamline was assumed to follow the blade grid. Though this is not far from the actual case due to the method of building the blade grid, this is an approximation. In fact, one reason for retaining the original "lifting swirl" portion of the calculation was that this portion of the swirl was not computed by a discretized differencing computation and was not prone to errors in the growth along psuedo-streamlines rather than actual streamlines. Since the drag induced swirl is generally much smaller than the lifting portion of the swirl it was felt that this approximation was justifiable. However, with a little effort in splining the drag force field, this approximation could be eliminated.

The computation of swirl due to tangential forces was numerically validated by computing the drag induced swirl from blade lifting forces (which are output from the Lifting Surface solver along with drag forces) and computing the resulting induced swirl. Comparison ofthe swirl output directly from the lifting surface code to the value computed using relation 4.13 provided evidence that the proper calculation was implemented. Figure 4-5 shows the trailing edge swirl distribution computed by both methods showing the force calculation of the swirl agrees with the lifting surface result. Also shown in Figure 4-5 are contour plots of the blade induced swirl calculated by both methods.

The entropy distribuition along the blade was computed using relations 4.9 and 4.10. Disctretizing these formulas along the streamtube gives equation 4.19.

Discretizing the pressure change due to viscous force along the streamline:

$$(p_t)_n = (p_t)_{n-1} - (F_{sv})_n (\Delta s)_n \qquad (4.17)$$

Where the volumetric viscous force F_{sv} is computed from the discrete panel force
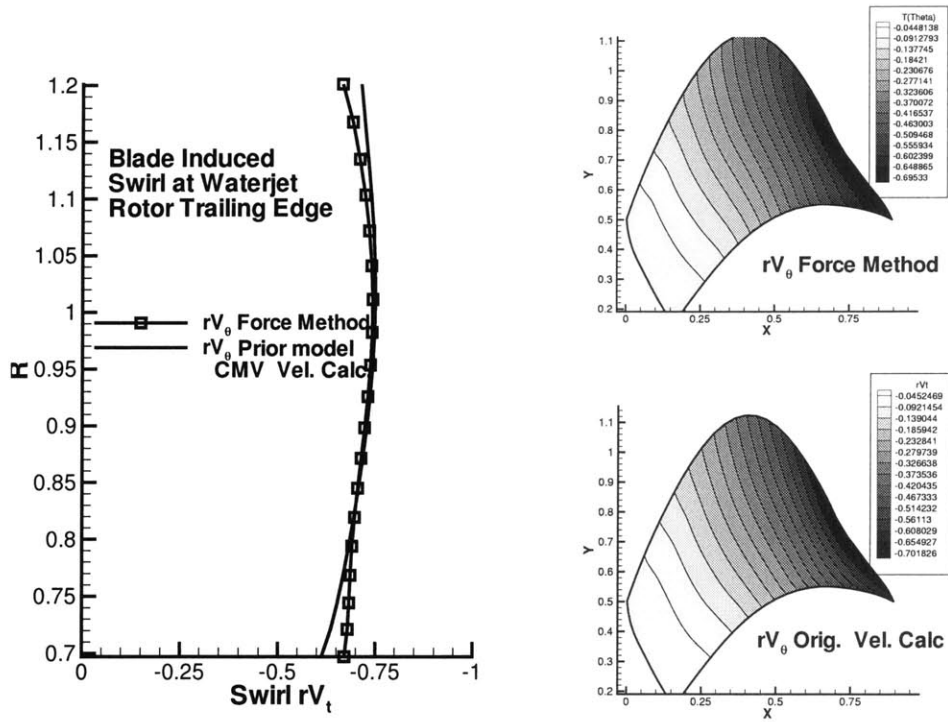
Figure 4-5: Comparison of force calculated swirl to original lifting surface circulation based model result

f_v as:

$$F_{sv} = \frac{f_{sv}}{2\pi r A_{panel}} \tag{4.18}$$

Referencing 4.17 equation 4.9, the change in entropy from the inlet DS becomes:

$$DS = -ln(\frac{(p_t)_{n-1} - F_{sv}\Delta s}{p_{tinl}}) \tag{4.19}$$

where the pressures are stagnation pressures Equations 4.17 through 4.19 were used to compute the differential entropy DS applied along the blade grid. As in the case of the drag induced swirl calculation, applying the differencing along the blade grid is not the same as applying the formula along the streamline, but through the same arguemnts employed for the drag induced swirl it was felt this was a justifiable approximation.

Chapter 5

Validation

5.1 Propeller 4119: Validation of Wake Alignment

To validate the wake alignment model, propeller geometry 4119 was used because data was actually published on the details of the wake trajectory by Jessup [13]. Data for this propeller included measurement of the wake position at a few locations downstream of the propeller as well as measurements of the tip vortex core radius at various downstream positions. This data allowed both validation of the wake alignment model to data as well as the vortex core growth model.

A study was conducted by which the trailing edge starting vortex core radius (RC_0)non-dimensionaalized on propeller radius, and the core growth damping constant RC_{grow} were varied over a range of reasonable values to explore the sensitivity of the wake position to these parameters.

The vortex growth model implemented took the form of:

$$R_{core} = \sqrt{RC_0^2 + RC_{grow}^2 \sum_1^n (\Delta t_n)}$$

where $RC_{grow} = \sqrt{4\beta\nu}$ and $\sum_1^n(\Delta t_n)$ is the time of flight along the vortex.

Figure 5-1 shows the computed position of the wake trailer of propeller 4119 at a fixed position of $x/R = 1.0$ and $r/R = 0.70$ downstream as a function of RC_0 and growth factor RC_{grow} in the vortex growth model, where the data is plotted in degrees from some reference blade position. This plot shows that the wake position is

94

insenstitive to the growth model parameters over a range of RC_0 of 0.001 to 0.05 and a growth parameter of 0.01 to 0.05. This range of values agree both with research done by Ramsey [30] where he found that a fixed core radius of 0.02 of propeller radius gave good results, as well as the values used to correlate with the data on a real tip vortex core(discussed later in this chapter).
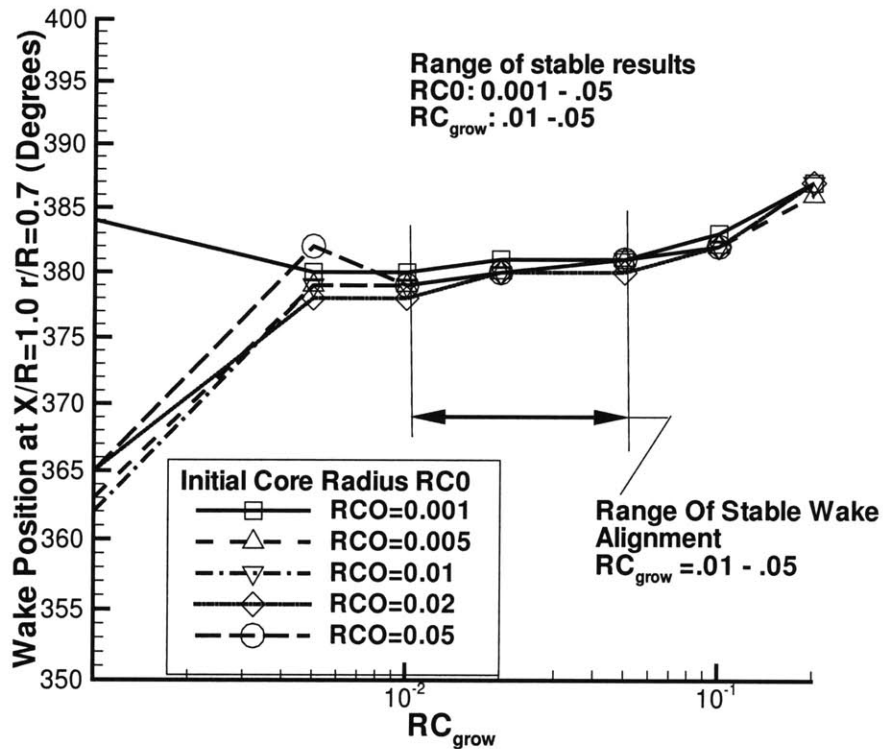
Figure 5-1: Effect of Initial Vortex Core Radius and Core Growth Factor on Wake Trailer Trajectory

Figure 5-2 shows the tip vortex core growth of propeller 4119 as a function of downstream position. Using the growth model a initial core radius of $RC_0 = 0.006$ was set along with a growth coefficient RC_{grow} of 0.02 . The RC_0 was chosen to match the experiment at the trailing edge, but the damping required was set according to the middle of the RC_{grow} range found in Figure 5-1. This shows that the growth factor which gives good results in wake alignment also agrees roughly in core radius with the experimental data in both the magnitude and shape of the core growth. It

is also interesting to note that the tip trailer under these circumstances lead to a core radius of about 0.02 in the region where our typical wake model ends. Through this research, it was found that instabilities grew with the length of the wake especially near the end of the modelled wake. Thus it appears that Ramsey's constant core value of 0.02 was needed to stabilize the end of the transition wake. In fact, with the core growth model the initial core size can be set to a much smaller value, which ison the order of the blade (or wake) thickness.
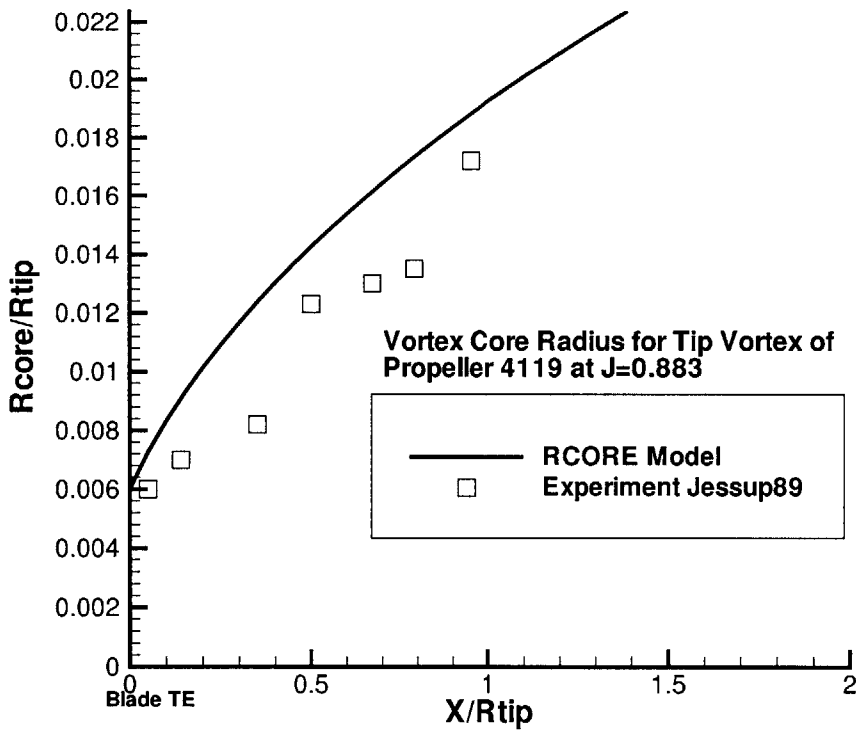
Figure 5-2: 4119 Tip trailer rcore growth: model vs. experiment

Wake alignment on propeller 4119 was conducted at the design advance coefficient of $J = 0.833$ and the propeller forces , KT ans KQ were computed. Table 5.1 shows the results of the aligned vs. unaligned wake on forces. Experimental results are also shown. It is apparent that wake alignment has only a small affect on the propeller forces for a coupled analysis. This means that the alignment of the wake with the

	KT	10KQ
No Wake Alignment	0.151	0.284
W/ Wake Alignment	0.153	0.287
Experiment	0.146	0.280

Table 5.1: Forces on Propeller 4119 at J=0.833 Aligned vs. Unaligned Wake

time averaged flow field captures most of the effects of the wake on blade forces.

Circulation distributions for the 4119 propeller are shown in Figure 5-3 for the unaligned and aligned analysis as well as the experimental result. These results show little difference in blade forces for aligned vs. unaligned wake even when there are relatively large differences in the wake trajectories (see Figure 4-2). It is important to note that the results shown are for a fully coupled analysis. When one uses only the lifting surface solver with an assumed effective flow, larger differences in forces generally results. During a coupled analysis, however, the flow is "aligned" with the circumferential mean flow, which accounts for most of the effects of the wake trajectory on the blade forces. In short, aligning the wake with the time averaged flow field, rather than the local flow, is generally all that is needed to get accurate blade forces.

The wake positions for propeller 4119 were measured by Jesssup [13] at an axial location of about one propeller radius downstream ($x/R = 0.95$). The angular and radial position of the wake at this location for the unaligned and aligned analysis are shown in Figure 5-4 and show some interesting behavior. The "unaligned" wake is actually aligned with the mean time averaged flow field and, of course, shows no rollup and little wake contraction. However, both the data and locally aligned wake show the wake rollup and contraction. The aligned wake of the model put the tip vortex at radius of about 0.91 vs. 0.87 for the experiment at $x/R = 0.95$. The unaligned wake had a tip radius of 0.97. The aligned case had a starting core radius of 0.01 at the trailing edge of the blade and a growth factor $RCgrow = 0.02$ for this case.
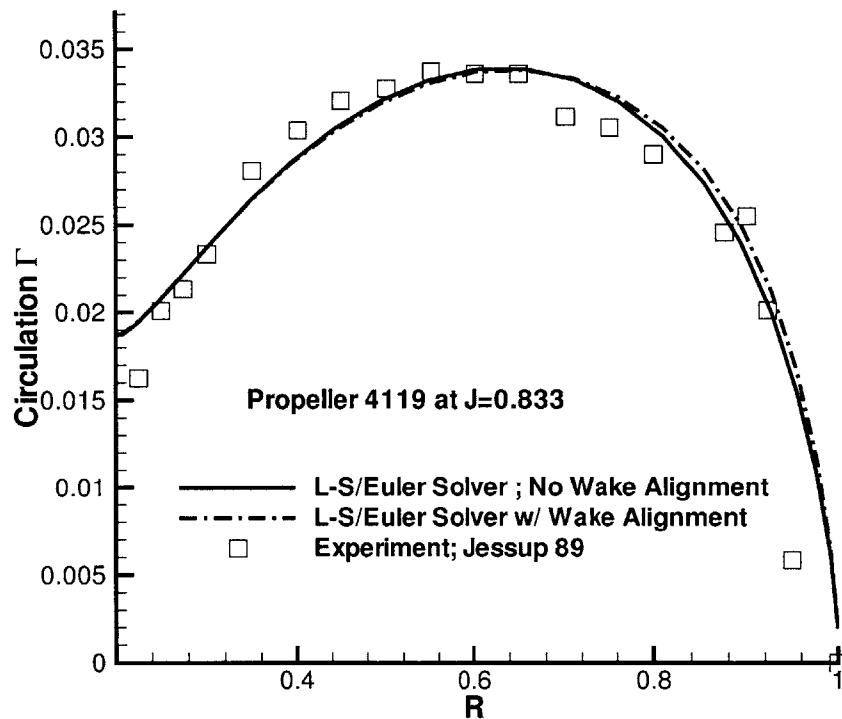
Figure 5-3: Aligned vs. Unaligned Circulation distributions for propeller 4119

5.2 MIT Waterjet

5.2.1 Coupled Lifting Surface/RANS Analysis

Coupled Lifting Surface/RANS analysis calculation were carried out on the waterjet geometry at various conditions. The early analysis results used estimated drag co-efficients were much lower than those found from the experiment. Updated analysis was performed using the experimentally estimated drag coefficients, giving improved results. Cases were run at the design flow condition as well as off desgin conditions to generate computed pump curves.

The typical RANS flowfield result is depicted in Figure 5-5, which shows the case of no tipgap, using experimentally determined drag coefficients at design $J = 1.147$. This figure shows the tangential velocity profiles and throughflow streamlines which show the swirl introduced by the rotor and taken out by the stator. Also shown are
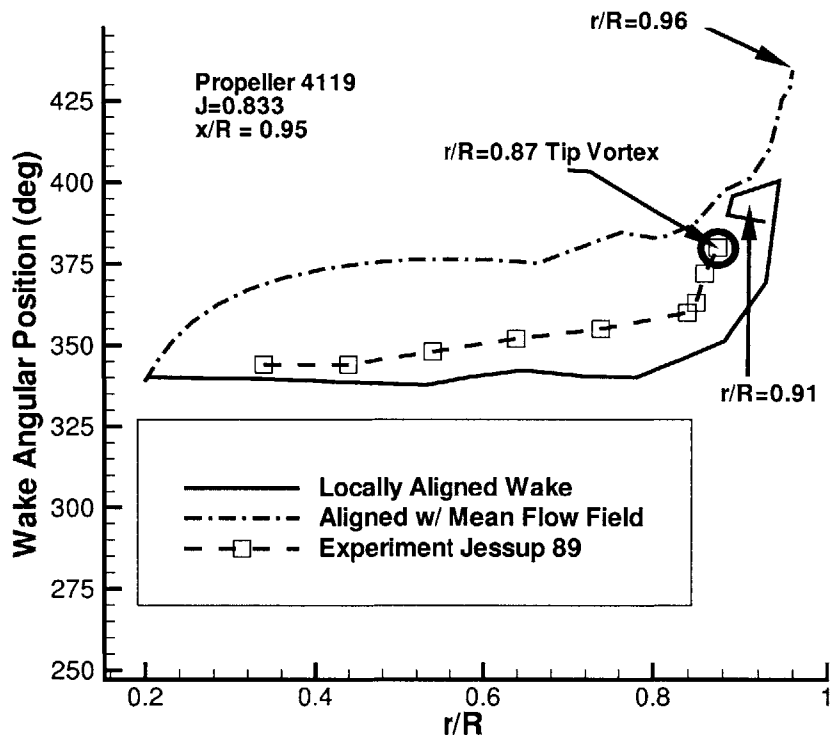
Figure 5-4: Wake Position Aligned vs. Unaligned vs. Experiment for Propeller 4119

the static and pressure contours. Note that the rotor increases the stagnation pressure but the stator leaves it almost unchanged (in fact it drops due to stator loss). Of course, this has to be the case since the stator can add no energy to the flow since its input shaft power is zero.

Figure 5-6 shows the calculated and experimental mean velocity profiles at the exit of the rotor. For the case where original estimates of drag coefficient were used the agreement is poor for the swirl velocity. However, when the experimentally estimated drag coefficients were introduced into the analysis the resulting swirl profile was much closer to experiment. This indicates that in the RANs coupling procedure the drag induced swirl is being accounted for by the coupled analysis. The RANS grid has a no slip boundary condition on the walls and was sufficient in length to generate a boundary layer at the duct inlet comparable to that measured in the experiment.

99
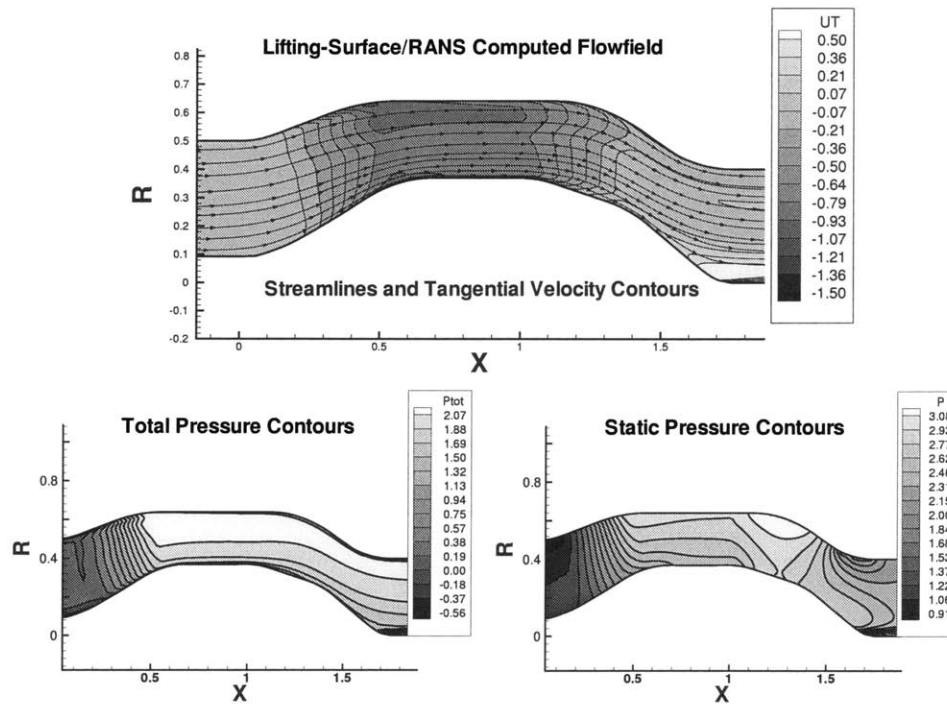
Figure 5-5: Output Rans flowfield

With the experimentally estimated drag coefficients entered into the numerical model the analysis gave much better prediction of the rotor losses as shown in Figure 5-7. This is no suprise for if the methods' bookkeeping is correct this is the result we expect. In other words if we input higher losses then we should get the higher losses out of the analysis. One puzzling issue with the loss result is that the loss is overpredicted by the L-S/RANS solver whereas the swirl(including drag induced swirl) of Figure 5-6 is underprected. This is not consistant since higher loss should result in higher swirl due to the increased drag induced swirl. This discrepancy should be explored further to resolve this issue.

Figure 5-8 shows the numerically determined pump curves for a variety of different analysis cases as compared to the experiment. Shown are the results using the original drag estimates as well as those determined from the experiment. These results show that when correct drag coefficients are used that the pressure rise of the pump agrees well with the experiment but the torque is overpredicted by 5% . This dicrepancy is likely tied to the overprediction of losses described earlier. As well, given the crude
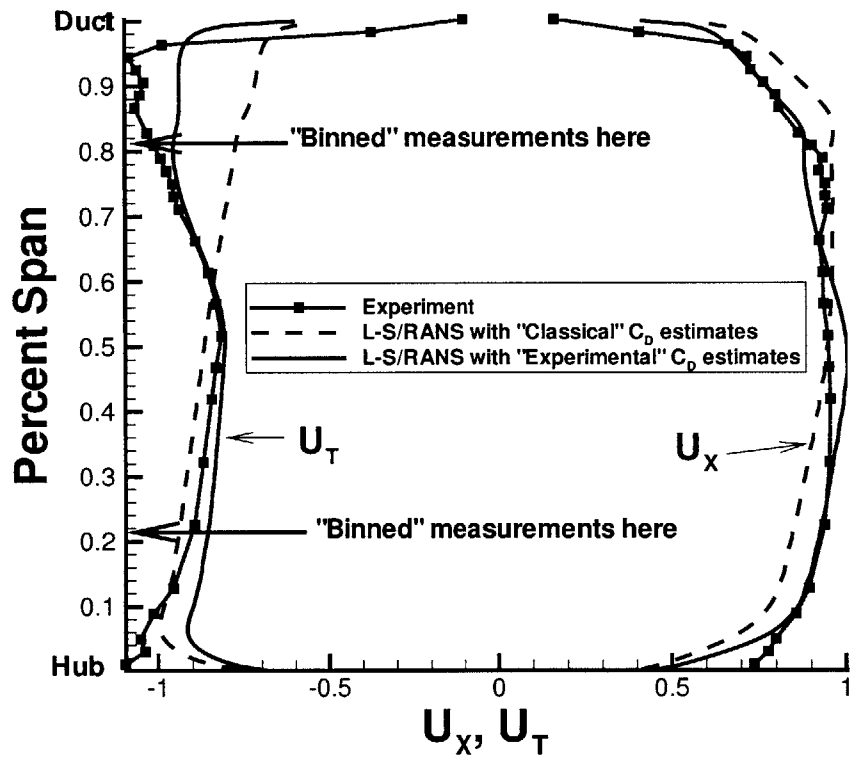
Figure 5-6: Rotor Mean Exit Velocity Profiles: RANS analysis vs. experiment

estimation of drag coefficients and also given that the tipgap was not modelled in this anlaysis the 5% torque discrepancy is not unrealistic.

The Lifting Surface/ RANS coupling method has been shown to give good results predicting the performance of the waterjet pumpset. However, small errors exist in the final solutions. The original design of Taylor et. al. [35] hit the design pressure rise but under predicted the torque by about 10%. This torque discrepancy was understandable for the losses input to the model were far lower than those realized in the actual pump. When estimates of the proper losses were introduced the pump performance was still in good agreement but the torque was too high by about 6% .
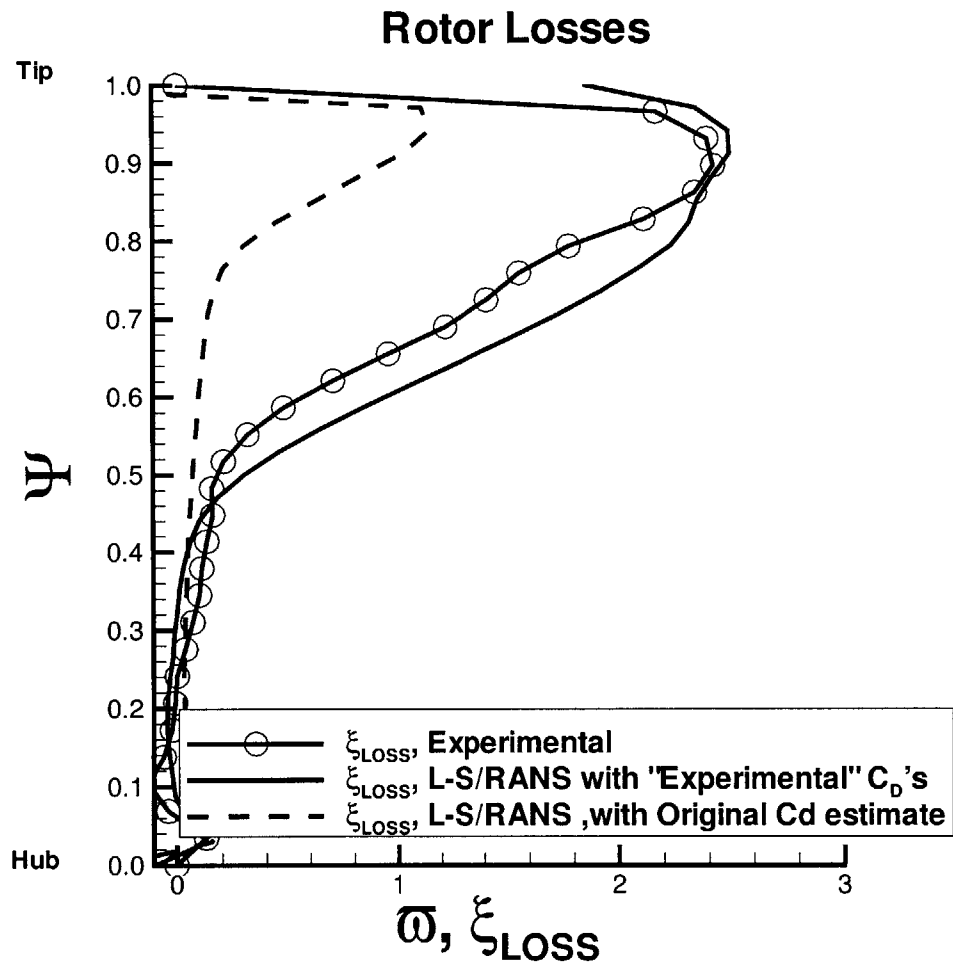
Rotor Losses

Figure 5-7: Waterjet Rotor losses RANS vs. Experiment

5.2.2 Coupled Lifting Surface/Euler solver

Comparisons of Euler solver results to experimental results were conducted on the waterjet test case to validate the Euler procedure including losses. Figure 5-9 depicts the typical output results of the Euler solver showing the contours of swirl in the duct work as well as the swirl and pressure coefficients levels along the ducts for each streamline. These results, of course, are similar to those shown for the RANS coupling output.

With the experimentally estimated drag coefficients input into the Lifting Surface/Euler coupling analysis the mean rotor exit swirl distributions were extracted
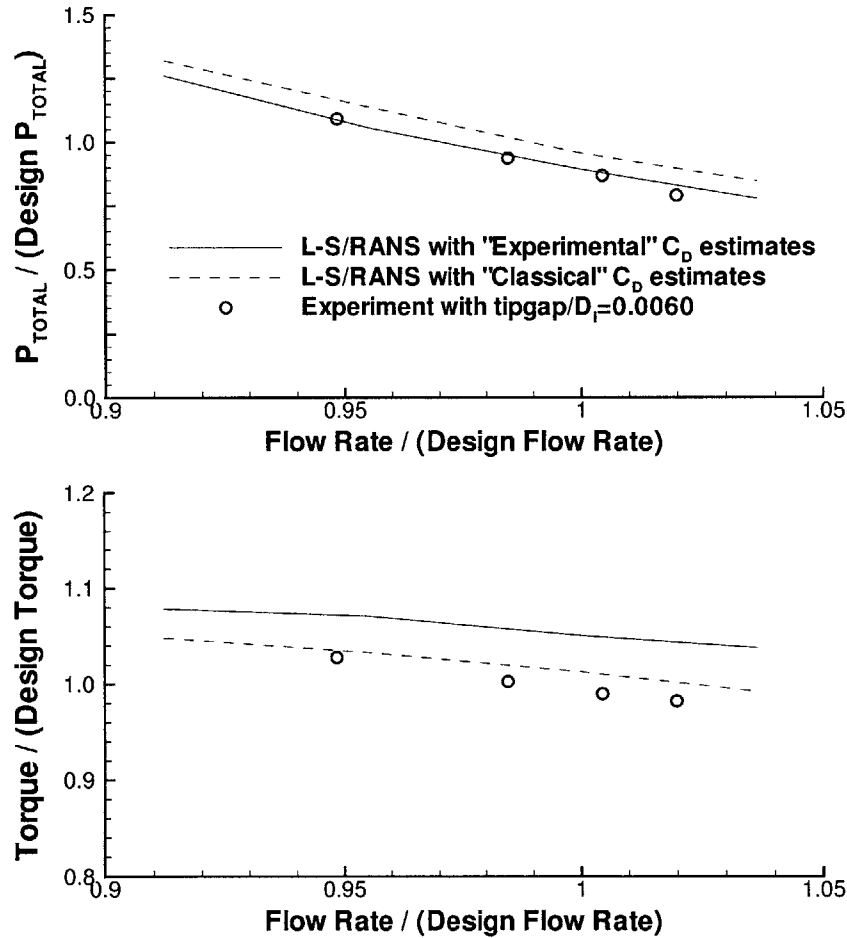
Figure 5-8: Comparison of pump performance curve of LS/RANS vs. experiment

from the resultant converged flowfield and compared to the experimental results. As can be seen in Figure 5-10 the swirl distributions of the case with losses show significant drag induced swirl over the no loss case. The axial velocity profiles show discrepency near the duct tip and near the hub. The tip region discrepancy is likely due to the fact that the inflow boundary layer was not modelled in the throughflow solver. A recent addition to the Euler coupling method was added by Hanson [10] to model arbritrary inflow profiles, but this was not used in this work for reasons of simplicity (since this new capability has not yet been well utilized). The overall swirl profile is also likely affected by the discrepancy in axial velocity profile since the two are linked by the blade surface boundary condition.

103
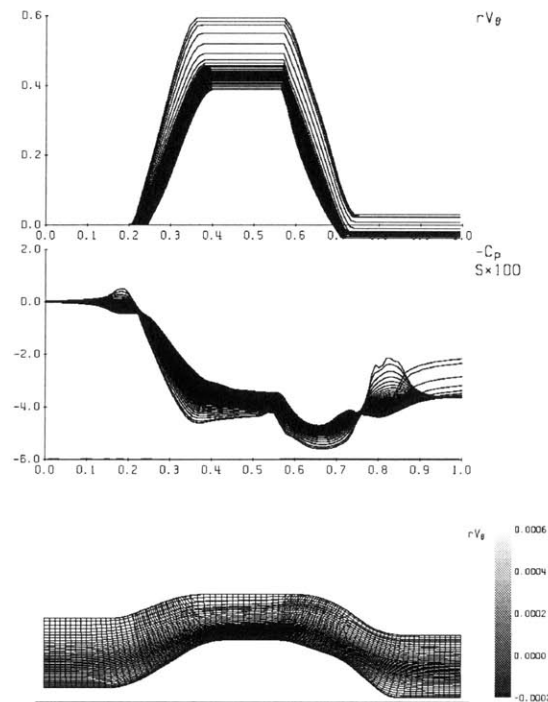
Figure 5-9: Flowfield Outputs from Euler solver

From the resultant Euler solver flowfield the loss profiles were also extracted and compared to the experiment. Figure 5-11 shows the resultant loss profiles at the waterjet rotor exit for the coupled Euler solution versus experiment, showing that the loss coupling through entropy gives good results in modelling the rotor loss profile. The results of Figure 5-11 are based upon the same experimentally extracted drag coefficients which were input into the Lifting Surface/RANS model. Both the loss profile of Figure 5-11 and the swirl profile in Figure 5-10 are somewhat lower than experiment near the tip in the region of high loss. This disrepancy is at least self consistant unlike the RANS results shown previously. Given the crudeness of this drag estimation the resultant computed loss profile is reasonably good, and gives evidence that the entropy loss modelling procedure is correct.

The tipgap model in the Lifting Surface solver was utilized to model the drop in blade loading due to tip leakage. However, the model had not been validated against
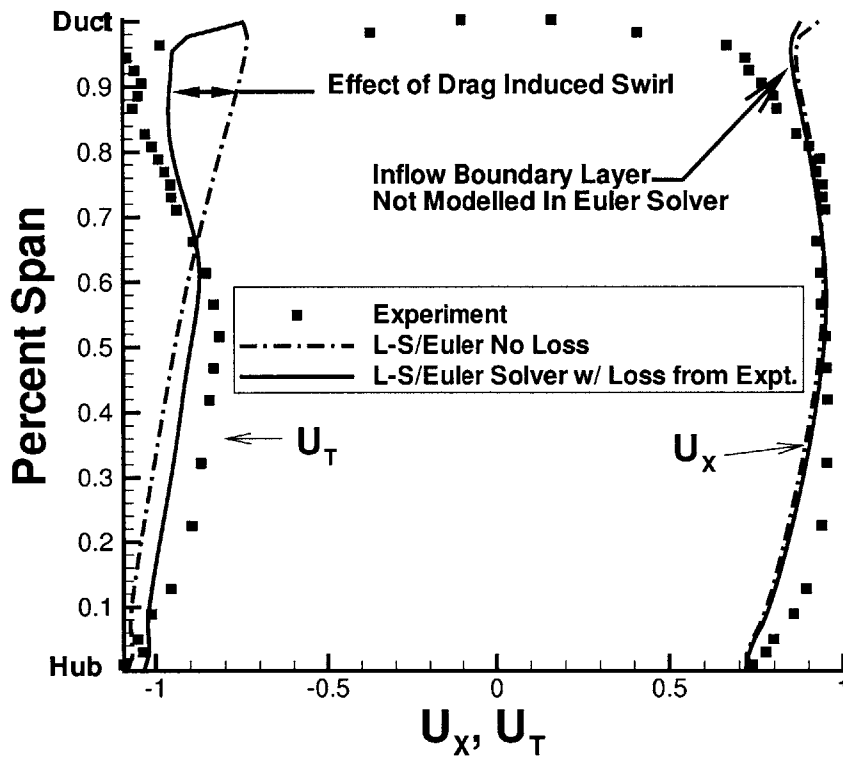
Figure 5-10: Waterjet Rotor Exit Velocity Profiles: Euler vs. Experiment

many cases, mainly due to the general lack of such data. Since good performance data were taken for the waterjet test case at various tip clearances, this became a good test case for the tipgap model itself. To test the tipgap model, cases were run with the Lifting Surface/Euler coupling method at the design J of 1.147 at various tip clearances. The results showed a drop in both pressure and torque as the tipgap was increased as expected. Figure 5-12 shows the computed tangential velocity and static pressure profiles at the rotor exit at various tip clearances. These plots show that the tip clearance affects the loading over the whole blade (not just locally at the tip). This result is no surprise since this is the typical result of tip leakage effects on blade loading.

The experimental tangential velocity profiles of Figure 3-10 show that the swirl in the leakage area does not drop much with increased tip gap. However the numerical

Rotor Losses
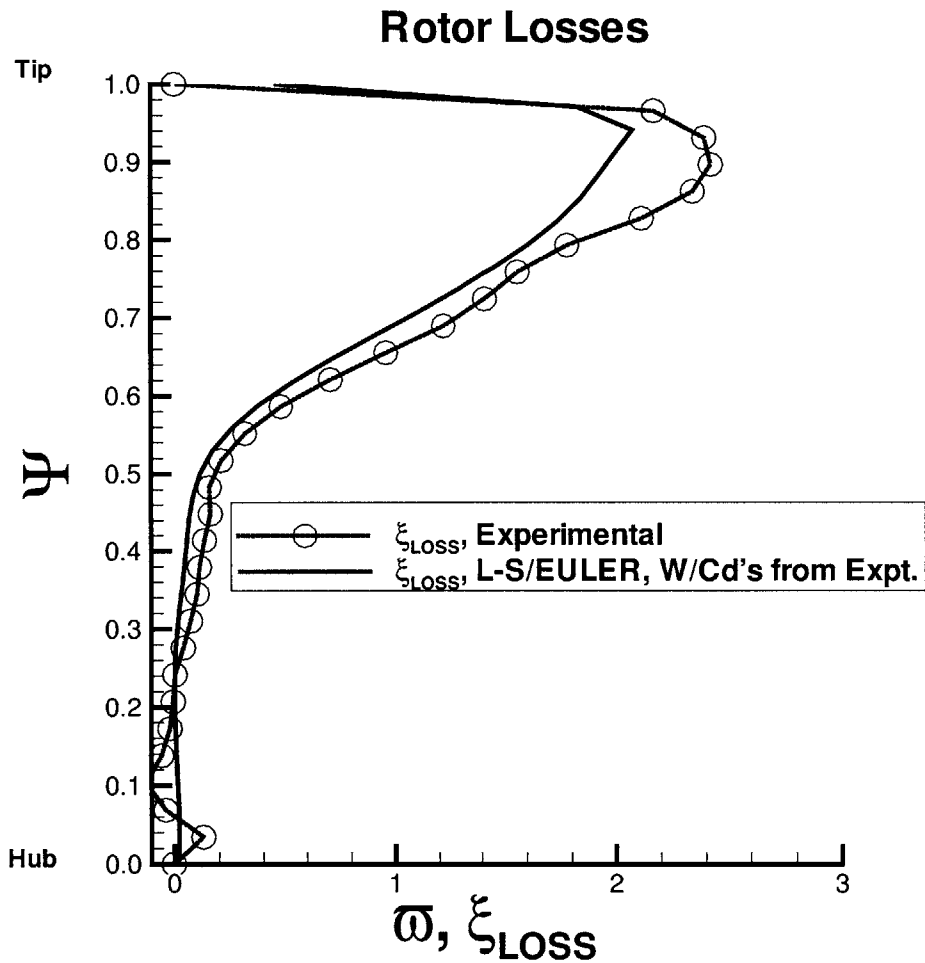
Figure 5-11: Waterjet Rotor Exit Loss Profiles: Euler vs. RANS vs. Experiment

results of Figure 5-12 do not show this behavior. This is puzzling and could provide clues for better modelling the leakage flow. Both the modelling of leakage loss (or entropy rise) as discussed earlier and the modelling of the tip leakage vortex are areas which may enable better prediction of the flow details in this region.

Figure 5-13 shows the drop in torque and total pressure in the waterjet pump as a function of tip clearance. The data is normalized to the "zero" gap value for comparison purposes. Both the computed and experimental results are shown. The numerical model does quite well in predicting the torque drop due to tip gap as compared to experiment. However, the drop in overall pressure rise due to tip gap is underpredicted by the numerical model. In fact to get the model to agree with
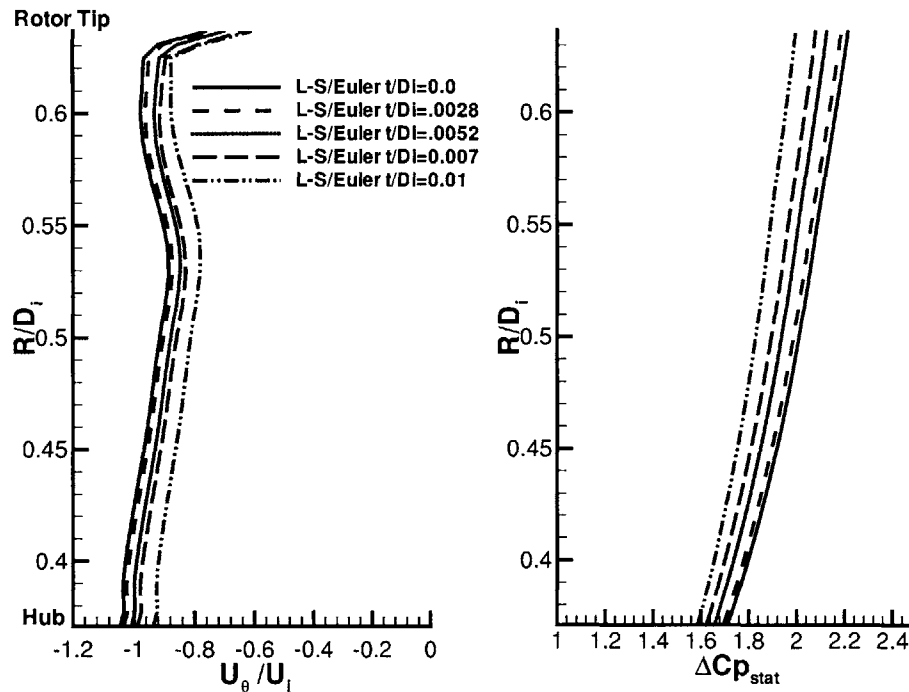
Figure 5-12: Computed Rotor Exit Tangential Velocity and Static Pressure profiles for the waterjet case at design flow J=1.147

experiment would require a gap about twice as large as tested, which is saying that the gap has less resistance than expected. Some of this discrepancy may be explained by the lack of inlet boundary layer in the numerical model, since the low axial inflow makes the blade see high angle of attack in this region, and hence could generate higher gap pressures, effectively increasing the gap leakage flow.

The validation of the coupled Lifting Surface /Euler solver as compared to the experiment has been demonstrated for the waterjet geometry. It is felt that this case is quite a severe validation case as compare to the typical propeller case for the following reasons:

- Mixed flow blade rows

- Internal flow such that pressure rise is significant

- Multi-Blade rows
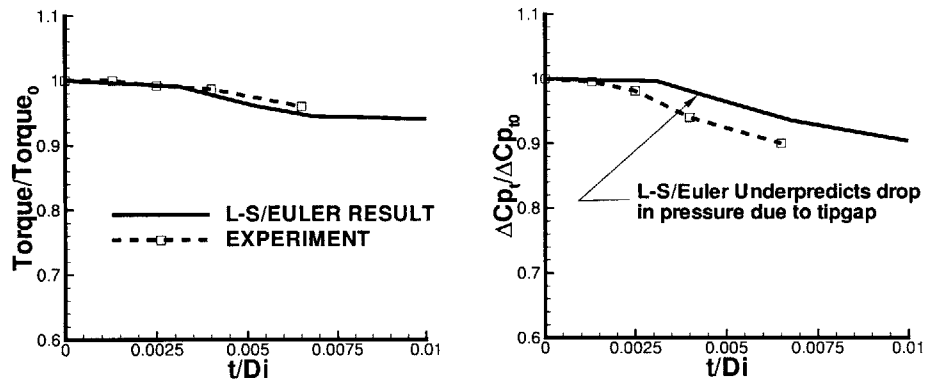
Figure 5-13: Normalized Torque and Pressure Loss vs. Tipgap: Computation vs. Experiment

- Presence of tip clearance flows

- Losses which significantly affect blade performance

- Large amount of drag induced swirl

For these reasons it is felt that the waterjet validation case put to the test the design and analysis methods validated in this work and gave good results. At this point it has been demonstrated that both the RANS coupling method and the Euler coupling method give good results when losses are properly included in the models. Some discrepancies still exist between the experiment and analysis but these dicrepancies are getting smaller as our understanding of waterjet flow characteristics increases. For example the understanding of rotor/duct losses resolved the original underprediction of torque which led to unusually high prediction of pump efficiencies.

The validation of the Euler solver also lead to large improvements in the numerical methods' capabilities. Though the Euler solvers' results are essentially equivalant to the RANS results, the speed, robustness and ease of use of the Euler solver greatly enhance the usefulness of these methods to the typical designer.

Chapter 6

Conclusions

6.1 Introductory Remarks

An overall result of this research has been the complete merging of the propeller world and the turbomachinery world. Concepts useful in either design paradigm were fit to compliment information gleaned in the other paradigm. For example, in the numerical work the coupling of fully three dimensional "propeller" blade design codes with a turbomachinery throughflow code enhanced the capabilities of both methodologies, each complimenting the other and strengthening the others' weaknesses.

On the experimental front bridging the gap between propeller terminology and turbomachinery terminology proved quite challenging. For example converting between drag coefficients and pressure loss coefficients was quite perplexing. An unforseen outcome of this research were relationships which converted form one paradigm to the other. For example the translation of blade drag to circumferential entropy rise, tangential forces to swirl were derived as part of this research.

6.2 Experimental Contributions

In the experimental portion of this research effort the following contributions were made that are of interest to the waterjet design and testing community:

- Design and implementation of a waterjet test facility

- Development of detailed waterjet test procedures relevant to detailed studies of waterjet performance

- Documentation of detailed measurements on a low aspect ratio mixed flow waterjet pumpset

- Development of analysis techniques for determining waterjet bladerow losses

6.2.1 Waterjet Test Facility

The waterjet test facility was constructed to ensure accurate measurements of parameters relevant to the performance of a waterjet in an efficient manner. The use of an accurately manufactured inlet flow nozzle provided simple and accurate measurement of the total flow rate. The incorporation of a rotatable wake screen ensured the capability to simulate non-uniform inflow. The measurement planes located at the inlet, midstage and outlet of the pumpset allowed efficient measurement of velocity and pressure profiles neccessary for detailed studies of waterjet losses. The waterjet facility as designed has already successfully provided data on various other waterjet pumpsets other than the pumpset reported in this work. It is hoped by the author that the thorough documentation of the waterjet test facility provided in this thesis may be of aid to others building similar facilities for testing waterjets.

6.2.2 Test procedures

Though many of the test procedures implemented in the waterjet test facility were standard (such as pump curves), the capabilities implemented in the collection of velocity and pressure profiles proved quite useful. The use of a two component LDV system allowed accurate measurement of both mean and phase averaged velocity profiles across the duct. The phase averaged data capability provided insightful data on the nature of the losses in the waterjet rotor. The use of Kiel probes to measure stagnation profiles, in the authors opinion, provided the most insightful information of all, the loss profiles of the bladerows. The amazing features of the simple and inexpensive Kiel probe are too compelling for the tester to ignore. The key features of a Kiel probe making it indispensible were:

- Ability to measure stagnation pressure regardless of incidence angle

- Ability to resolve time average stagnation pressure in highly varying flowfields

- Provided a direct measurement of time averaged fluid energy at a given duct radius

6.2.3 Tests on a mixed flow marine waterjet

Of all the data taken a few of the results published were noteworthy. First, the measurement of the pump performance on a mixed flow waterjet as a function of tip clearance is data rarely published on waterjets. It is hoped that the data provided in this work can provide designers an idea of the relative magnitude of such losses in marine waterjets.

The measurements of detailed loss profiles was useful, not only in the methodology, but this data provided insight into the loss mechanisms of such a waterjet. In essence the losses of the rotor were completely driven by the nature of the flows near the duct wall junction in the region of the tip clearance.

The complete energy balance analysis of the waterjet pumpset is also something rarely seen even in the turbomachinery literature, but provided insightful validation of the measurement tools and procedures.

6.3 Numerical Modelling and Validation

6.3.1 Wake alignment

A generalized wake alignment scheme was incorporated into the Lifting Surface portion of the numerical model and validated against available data. This method aligned the wake with the local flowfield and included the effects of the wake self induction. The scheme avoided the typical instabilities associated with past wake alignment schemes by implementing the following features into the alignment scheme:

- Computation of wake induction velocities on the wake nodes

- Use of desingularized vortex influence functions which mimicked the "viscous core" of a real vortex

- Implementation of a viscous core growth model based on an Oseen vortex decay model which grew the vortex as the wake sheet progressed, thus better stabilizing the wake sheet.

Validation of the wake alignment scheme against experiment showed good results if reasonable value of the starting vortex core radius and growth factor were input.

6.3.2 Loss Modelling

Both a drag induced swirl model and an entropy rise model were implemented into the Lifting Surface/Euler solver model. The resulting model compared well to the experimental results providing validation of the loss coupling method. The end result of the loss coupling with the Euler solver was that it could give results comparable to the RANS solver in 1-2 orders of magnitude less time.

6.3.3 Validation Efforts

Running both the Lifting Surface/RANS model and the Lifting Solver/Euler model gave reasonable results on rotor and stator performance (including exit swirl and loss profiles) as compared to experiment as long as the proper losses (through section drag coefficients) were input to the model. Ideally one would like to predict losses as part of the model, but in the case of complex losses such as those seen in the waterjet calculation of the losses is, at this point, difficult. However, since the numerical model was shown to give good results if the correct losses were input, this lends credence to the methods' ability to correctly compute the performance of a complicated propulsor given proper loss inputs. This means that if and when improvements to the prediction and modelling of these secondary flow losses are developed, such models could be incorporated into the numerical model, expanding the prediction capability of the model. It should be noted some discrepancies arose in the loss coupling for the RANS procedure which should be explored.

6.4 Recommendations for Future Work

The work presented in this thesis touched upon areas important to the numerical modelling of waterjets. Several areas of improvements to the model to better predict the performance of waterjets were implemented and studied as part of this effort. The research also identified areas that could be better modelled but such models were not implemented as part of this research. Some of the areas of possible future modelling improvements are:

- Direct modelling of the tipgap leakage loss. In the thesis a derivation of such a loss model was presented and it would be rather straightforward to implement such a calculation of the losses due to the leakage flow. Since the proposed method relies on computing tipgap forces, it is completely compatible with the current coupling model.

- Discrete modelling of the tip leakage vortex. The tip leakage vortex observed may have a significant impact on the evolution of the junction flow near the rotor tip. This leakage vortex could be modelled in much the same way the blade wake sheet is modelled, as a set of trailers emanating from the tip panels. In this sense the wake alignment scheme implemented in this research could prove useful in tracking the trajectory of this leakage vortex, since its position relative to the blade surface may impact the flow in that region of the blade.

- Extend waterjet validation efforts to include capabilities already incorporated into the numerical model. These include:

  - Stripwise viscous boundary layer calculation of blade drag directly on the blade surfaces. This calculation is expected to have trouble near the junction flow region but could give insight onto the nature of large drag behaviors near the blade tips.

  - Explicitly modelling the measured inlet profile using the entropy method developed by Hanson [10] for the Lifting Surface Euler model.

  - Implement an improved thickness modelling scheme in the Lifting Surface

solver. Small errors in thickness result in blockage errors in the throughflow solver, such that each of the solvers are essentially solving for a different flow condition.

It is obvious that the research on waterjets conducted in this research has only begun to explore the complexities faced in modelling losses on a complex waterjet propulsor. Though the results of the modelling efforts have shown good results with the ability to predict pressure rise and torque of a multi bladerow waterjet to better than $\pm 5\%$, improvements to these models would also provide insight on how to better design waterjets in the future.

6.5 Closing Remarks

In this research the following contributions were made in the areas of experimental studies and numerical modelling of a mixed flow marine waterjet:

- Construction of a fully capable waterjet test facility including instrumentation and test procedures useful to documenting, in detail, the performance of a waterjet pumpset.

- Measurement of the performance details of a very low aspect ratio rotor with stator including effects of tipgap on performance as well as detailed velocity and pressure surveys.

- The determination of bladerow losses from the measurements as well as the presentation of a full energy balance

- Validation of the numerical models in modelling the pump performance using losses computed from the experiment.

- Addition of loss coupling to the Euler solver through the conversion of blade forces to swirl and entropy rise.

- Implementation of a general local wake alignment scheme into the Lifting Surface solver.

It is hoped by the author that the insights gleaned from both the experimental studies and the modelling efforts will prove useful to the waterjet design community in the pursuit of better waterjet technology. The results shown from this research show that improvements to performance and efficiency are still possible with the research pointing to likely areas where improvement efforts may be concentrated.

Appendix A

Mathematical Derivations

A.1 Derivation of Vortex core radius vs. time for Oseen vortex

Given the Oseen vortex profile:

$$V_\theta = \frac{\Gamma}{2\pi R}\left(1 - e^{-\frac{R^2}{4\nu\tau}}\right)$$

(A.1)

By taking the derivitive of the Oseen vortex equation above we can derive a relation relating the core radius (R_{core}) to the kinematic viscosity and decay time as shown in equations A.2 to A.6.

Letting:

$$\alpha = \frac{1}{4\nu\tau} \text{ and } \beta = \frac{R^2}{4\nu\tau}$$

(A.2)

Then taking the derivitive of equation 4.2 with respect to R and setting $\frac{DV_\theta}{DR} = 0$ and

116

$R_{core} = R$ gives:

$$\frac{DV_\theta}{DR} = 0 = \frac{\Gamma\alpha}{2\pi}\left(-\frac{1}{\beta} + 2e^{-\beta} + \frac{e^{-\beta}}{\beta}\right)$$

(A.3)

Which can be reduced to:

$$0 = -1 + 2\beta e^{-\beta} + e^{-\beta} \text{ or}$$
$$1 = 2\beta e^{-\beta} + e^{-\beta}$$

(A.4)

Solving equation A.4 iteratively gives:

$$\beta = 1.255$$

(A.5)

So from the definition of β (equation A.2) gives:

$$R_{core} = \sqrt{4\beta\nu\tau} \text{ where } \beta = 1.255$$

(A.6)

117

A.2 Derivation of Swirl induced by a volumetric force due to viscous drag and lifting forces

For a volumetric body force applied to a fluid the tangential momentum equation can be shown to take the form A.7, see Lyman[26].

$$rF_\Theta = \rho \frac{D(rV_\Theta)}{Dt}$$

Where F_Θ is a volmetric body force and D/Dt is the substantial derivative

(A.7)

$$\frac{rF_\Theta}{\rho} = \frac{\partial(rV_\Theta)}{\partial t} + V_x \frac{\partial(rV_\Theta)}{\partial x} + V_r \frac{\partial(rV_\Theta)}{\partial r} + V_\Theta \frac{\partial(rV_\Theta)}{r\partial \Theta}$$

(A.8)

Assuming steady flow and noting that $Vs = \Delta s/\Delta t$, $V_x = \Delta x/\Delta t$, $V_\Theta = r\Delta\Theta/\Delta t$, $V_r = \Delta r/\Delta t$ and noting that $\vec{V}_s = \vec{V}_x + \vec{V}_r + r\vec{V}_\Theta$ then equation A.8 becomes:

$$\frac{rF_\Theta}{\rho} = V_s \frac{d(rV_\Theta)}{ds}$$

(A.9)

Or in discrete form:

$$\frac{rF_\Theta}{\rho} = V_s \frac{\Delta(rV_\Theta)}{\Delta s}$$

(A.10)

Differencing rV_Θ along a streamline where:

$$\Delta(rV_{\Theta v})_n = (rV_{\Theta v})_n - (rV_{\Theta v})_{n-1}$$

(A.11)

Thus at node n:

$$\Delta(rV_\Theta)_{vn} = (rV_{\Theta v})_n - (rV_{\Theta v})_{n-1} = \frac{rF_{\Theta vn}\Delta s}{\rho V_s}$$

(A.12)

Solving for $(rV_{\Theta v})_n$ gives

$$(rV_{\Theta v})_n = (rV_{\Theta v})_{n-1} + \frac{rF_{\Theta n}\Delta s}{\rho V_{sn}}$$

(A.13)

Adding in the swirl at the node due to lifting force gives the total blade induced swirl:

$$(rV_{\Theta tot})_n = (rV_{\Theta v})_n + (rV_{\Theta lift})_n$$

(A.14)

Converting the discrete blade panel force to the circumferential mean volumetric force $F_{\theta v}$

$$F_{\Theta v} = \frac{f_{\Theta v}}{2\pi r A_{panel}}$$

(A.15)

A.3 Proof of drag induced swirl error by applying drag forces at blade trailing edge

Assume that the two forces are applied on blade panels at two different radii along the same streamline, one at the blade trailing edge. Also assume that the radial velocity at these points is zero and dr for the streamline across this panel is zero (to simplify things).

Then let:

$$\beta = \frac{2\pi \rho V_s}{\Delta s}$$

At point 1 (from the conservation of momentum):

$$F_1 = \frac{\beta_1}{r_1} \Delta(r_1 V_{\Theta 1}) = \beta_2 \Delta(V_{\Theta 1})$$

At point 2:

$$F_2 = \frac{\beta_2}{r_2} \Delta r_2 V_{\Theta 2} = \beta_2 \Delta V_{\Theta 2}$$

so:

$$F_1 + F_2 = \beta_1 \Delta V_{\Theta 1} + \beta_2 \Delta V_{\Theta 2} = F_{tot}$$

Now assume that the force is applied to the trailing edge:

$$V_{\Theta TE} = \Delta V_{\Theta 1} + \Delta V_{\Theta 2}$$

The swirl induced by the total forces applied to the trailing edge is:

$$F_{tot} = \beta_2 \Delta V_{\Theta TE} \neq \beta_1 \Delta V_{\Theta 1} + \beta_2 \Delta V_{\Theta 2}$$

Since:

$$\beta_1 \neq \beta_2 \quad \text{In general}$$

Bibliography

[1] J. L. Allison. Marine Waterjet Propulsion. *SNAME Transactions*, 101, 1993.

[2] J.L. Allison, C. Jiang, J.G. Stricker, M.M. Athavale, J.E. Kerwin, and T.E. Taylor. Modern Tools for Waterjet Pump Design and Recent Advances in the Field. In *Royal Institution of Naval Architects Conference on Waterjet Propulsion – Latest Developments*, Amsterdam, The Netherlands, 1998.

[3] A. L. Batcheller and R. W. Kimball. A Procedure for the Calibration of Pressure Transducers, December 1999.

[4] S. D. Black. *Integrated Lifting-Surface/Navier-Stokes Design and Analysis Methods for Marine Propulsors*. PhD thesis, Department of Ocean Engineering, Massachusetts Institute of Technology, June 1997.

[5] D. Burke. *Discrete Vortex Theory for Propeller in Non-Uniform Flow*. PhD thesis, Department of Ocean Engineering, Massachusetts Institute of Technology, 1972.

[6] J. D. Denton. Loss Mechanisms in Turbomachines. *ASME Journal of Turbomachinery*, 115:621–656, October 1993.

[7] M. Drela. XFOIL: An Analysis and Design System for Low Reynolds Number Aerofoils. *Lecture Notes in Engineering: Low Reynolds Number Aerodynamics*, (54), 1989.

[8] F. Durst, A. Melling, and J. H. Whitelaw. *Principles and Practice of Laser-Doppler Anemometry*. Academic Press, 2nd edition, 1981.

[9] D. S. Greeley and J. E. Kerwin. Numerical Methods for Propeller Design and Analysis in Steady Flow . *SNAME Transactions*, 90, 1982.

[10] C.J. Hanson. Integrated Lifting-Surface and Euler/Boundary-Layer Theory Analysis Method for Marine Propulsors. Master's thesis, Department of Ocean Engineering, Massachusetts Institute of Technology, 2000. also Naval Engineer's thesis.

[11] R. J. Van Houten. Analysis of ducted propellers in steady flow. Technical Report 4.76-1, Airflow Research and Manufacturing Corp., Watertown, MA., February 1986.

[12] I. Huntsman and R. Hothersall. Development of Quasi 3D Design Methods and 3D Flow Solvers for the Hydrodynamic Design of Water Jets. In *Waterjet Propulsion III*, Gothenburg, Sweden, February 2001. Royal Institution of Naval Architects.

[13] Stuart D. Jessup. *An Experimental Investigation of Viscous Aspects of Propeller Blade Flow*. PhD thesis, The Catholic University of America, June 1989.

[14] J. E. Kerwin. New facilities for research in naval architecture and marine engineering at mit: Variable pressure water tunnel. Technical report, New England Section, SNAME, October 1967.

[15] J. E. Kerwin. Computer techniques for propeller blade section design. *International Shipbuilding Progress*, 20(227), 1973.

[16] J. E. Kerwin. A method of treating ducted propeller tip gap flows in a potential flow panel code. Technical Report Internal Report, Massachusetts Institute of Technology, Cambridge, Ma., October 1989.

[17] J. E. Kerwin. The MIT Marine Hydrodynamics Water Tunnel–A 53'rd Anniversary Celebration. Technical report, New England Section, SNAME, May 1992.

[18] J. E. Kerwin, D. P. Keenan, S. D. Black, and J. G. Diggs. A Coupled Viscous/Potential Flow Design Method for Wake-Adapted, Multi-stage, Ducted

Propulsors. In *Proceedings, Society of Naval Architects and Marine Engineers*, 1994.

[19] J. E. Kerwin and C. S. Lee. Prediction of Steady and Unsteady Marine Propeller Performance by Numerical Lifting-Surface Theory . *SNAME Transactions*, 86, 1978.

[20] J.E. Kerwin, S.D. Black, T.E. Taylor, and C. L. Warren. A Design Procedure for Marine Vehicles with Integrated Propulsors. In *Propellers/Shafting '97 Symposium*, Virginia Beach, VA, September 1997. Ships' Machinery Committee, SNAME.

[21] J.E. Kerwin, T.E. Taylor, S.D. Black, and G. McHugh. A Coupled Lifting-Surface Analysis Technique for Marine Propulsors in Steady Flow. In *Propellers/Shafting '97 Symposium*, Virginia Beach, VA, September 1997. Ships' Machinery Committee, SNAME.

[22] Justin E. Kerwin. 13.04 Lecture Notes - Hydrofoils and Propellers, February 2001.

[23] R.W. Kimball, J.O. Scherer, and T.E. Taylor. Enhancements to the Design and Analysis of Waterjet Propulsors Using a Coupled Lifting-Surface/RANS Technique and Comparison with Experiment. In *Waterjet Propulsion III*, Gothenburg, Sweden, February 2001. Royal Institution of Naval Architects.

[24] R.I. Lewis. *Turbomachinery Performance Analysis*. Arnold, London, 1996.

[25] E. H. Lurie. A Note on the Error Analysis of Velocity Measurements of the Flapping Foil Experiment. Technical Report Rep. 95-3, Department of Ocean Engineering, Massachusetts Institute of Technology, November 1995.

[26] F. A. Lyman. On the Conservation of Rothalpy in Turbomachines. *ASME Journal of Turbomachinery*, 115:520–526, October 1993.

[27] G. McHugh. Advances in Ducted Propulsor Analysis using Vortex-Lattice Lifting-Surface Techniques. Master's thesis, Department of Ocean Engineering, Massachusetts Institute of Technology, 1997. September, 1997.

[28] Air Moving and Control Association. AMCA Standard 210-85, 1985.

[29] S. Pyo and S.A. Kinnas. The flow adapted grid (flag) applied to the analysis of propeller tip flows. In *Proceedings of the Propellers/Shafting '94 Symposium*, Virginia Beach, VA, September 1994. SNAME.

[30] W. Ramsey. *Boundary Integral Methods for Lifting Bodies with Vortex Wakes*. PhD thesis, Department of Ocean Engineering, Massachusetts Institute of Technology, 1996.

[31] D.H. Renick. An Analysis Procedure for Advanced Propulsor Design. Master's thesis, Massachusetts Institute of Technology, June 1999. also Naval Engineer's thesis.

[32] D.H. Renick. *Unsteady Propeller Hydrodynamics*. PhD thesis, Department of Ocean Engineering, Massachusetts Institute of Technology, 2001.

[33] T. E. Taylor. Combined Experimental and Theoretical Determination of Effective Wake for a Marine Propeller. Master's thesis, Massachusetts Institute of Technology, October 1993.

[34] T.E. Taylor and R.W. Kimball. Experimental Validation of a Coupled Lifting-Surface/RANS Procedure for Waterjet Pump Design and Analysis. In *SNAME Fast 99 : Fifth International Conference on Fast Sea Transportation*, Seattle WA, 1999.

[35] T.E. Taylor, J. Otto Scherer, and J.E. Kerwin. Waterjet Pump Design and Analysis Using a Coupled Lifting-Surface and RANS Procedure. In *Royal Institution of Naval Architects Conference on Waterjet Propulsion – Latest Developments*, Amsterdam, The Netherlands, 1998.

[36] NH 03031 United Sensor Corporation, 3 Northern Blvd. Amherst. Kiel Probes Bulletin 3, June 1983.

[37] M. H. Vavra. *Aero-Thermodynamics and Flow in Turbomachines*. Wiley, New York, 1960.

[38] C.L. Warren, T.E. Taylor, and J.E. Kerwin. A Coupled Viscous/Potential-Flow Method for the Prediction of Propulsor-Induced Maneuvering Forces. In *Propellers/Shafting 2000 Symposium*, Virginia Beach, Virginia, September 2000. Society of Naval Architects and Marine Engineers.

[39] F. M. White. *Viscous Fluid Flow*. McGraw-Hill, second edition, 1991.

[40] H. B. Wilson and R. J. Van Houten. A program for interpolation, smoothing, fourier analysis, and effective wake estimation of propeller inflow fields: Mitwkproc user's manual. Technical Report 83-7, Department of Ocean Engineering, Massachusetts Institute of Technology, June 1983.

[41] G. F. Wislicenus. *Fluid Mechanics of Turbomachinery*. Dover, second edition, 1965.

[42] G. F. Wislicenus. Hydrodynamic Design Principles of Pumps and Ducting For Waterjet Propulsion. Technical report, National Technical Information Service, U.S. Department of Commerce, 5285 Port Royal Rd. Springfiled Va. 22151, June 1973.

[43] M. Zangeneh. Inviscid-Viscous Interaction Method for Three-Dimensional Inverse Design of Centrifugal Impellers. Technical Report 2, ASME, April 1994.

[44] M. Zangeneh and M. Roddis. A Three-Dimensional Method for the Design of Marine Ducted Propulsor Blading. Technical report, Virginia Beach, VA, September 1994.

[45] W.C. Zierke, W.A. Strake, and P.D. Taylor. An Experimental Investigation of the Flow through an Axial-Flow Pump. *Journal of Fluids Engineering*, 117(1):485 – 490, September 1995.